Development of Zinc Nitride Materials for Semiconductor Applications

By:

Aristotelis Trapalis

A thesis submitted in partial fulfilment of the requirements for the degree of
Doctor of Philosophy

The University of Sheffield
Faculty of Engineering
Department of Electronic and Electrical Engineering

November 2018

to my friends and family·

σας ευχαριστώ

Table of Contents

Acknowledgements iii

Abstract v

Chapter 1: Introduction 1
1.1. Semiconductor materials and devices 1
1.2. Zinc Nitride and Zn-IV-Nitrides 2
1.3. Thesis outline 4
1.4. Bibliography 5

Chapter 2: Literature Review of Zinc Nitride 7
2.1. Crystal structure 7
2.2. Charge transport properties 9
2.3. Bandgap and refractive index 11
2.4. Chemical synthesis approaches 14
2.5. Physical vapour deposition 18
2.6. Roadmap for applications 21
2.7. Summary 23
2.8. Bibliography 23

Chapter 3: Experimental Techniques and Methodologies 27
3.1. Physical vapour deposition techniques 27
3.2. Characterisation techniques 33
3.3. Bibliography 46

Chapter 4: Zinc Nitride Grown by Sputtering 49
4.1. Sputtering process 49
4.2. Surface morphology and film composition 52
4.3. Crystal structure 55
4.4. Charge transport properties 57
4.5. Absorption coefficient and refractive index 59
4.6. Photoluminescence 63
4.7. Summary 68
4.8. Bibliography 69

Chapter 5: Zinc Nitride Grown by Molecular Beam Epitaxy 73
5.1. Molecular Beam Epitaxy of Zinc Nitride 73
5.2. Growth process parameters 73
5.3. Effect of experimental parameters on the growth rate 77
5.4. Morphology and crystal structure 85
5.5. Charge transport properties 91
5.6. Optical bandgap and Burstein-Moss shift 95
5.7. Summary 99

5.8. Bibliography 100

Chapter 6: Aluminium Zinc Nitride Grown by Sputtering 103
6.1. Bandgap tuning in Zinc Nitride materials 103
6.2. Compositional analysis of a II-III-V alloy 104
6.3. Crystal structure and morphology 107
6.4. Absorption coefficient and refractive index 108
6.5. Charge transport properties 112
6.6. Summary 114
6.7. Bibliography 114

Chapter 7: On thermal annealing and the stability of Zinc Nitride 117
7.1. Ex-situ thermal annealing of Zinc Nitride 117
7.2. Ambient stability of annealed samples 117
7.3. Crystal structure 122
7.4. Optical bandgap 123
7.5. Summary 125
7.6. Bibliography 126

Chapter 8: Zinc Nitride Nanoparticles by Gas Phase Aggregation 127
8.1. Zinc Nitride nanoparticles 127
8.2. In-situ process monitoring 127
8.3. Deposition rate and process stability 129
8.4. Nanoparticle deposition with and without nitrogen plasma 130
8.5. Summary 133
8.6. Bibliography 134

Chapter 9: Conclusions and Further Work 135
9.1. Conclusions 135
9.2. Further work 137
9.3. Bibliography 140

Acknowledgements

Throughout my PhD studies, I have been fortunate to work with people who helped me cope with the difficulties of studying for a PhD, and without whom this task would have been much more difficult. I would like to express my gratitude above all to Prof. Jon Heffernan, Dr. Ian Farrer, Dr. Alistair Kean, and Dr. Jonathan Sharman who played a critical role in guiding this project and my development as a student. I would also like to thank the research staff in the National Epitaxy Facility in the University of Sheffield who have helped introduce me (and many other students) to the facilities, despite their own busy schedules. This includes Dr. Kenneth Kennedy, Dr. Paul Fry, and Mr. Saurabh Kumar. Last but not least, I would like to thank friends, family, and fellow PhD students with whom I have shared my frustrations and difficulties over this period, and who have helped make my time in Sheffield enjoyable.

This research was co-funded by the EPSRC (Engineering and Physical Sciences Research Council) and Johnson Matthey PLC. The financial support by these parties is highly appreciated. Some of the results and discussion presented in this work have produced the following publications:

1. "Structural, electrical and optical characterization of as grown and oxidized zinc nitride thin films", A. Trapalis, J. Heffernan, I. Farrer, J. Sharman, and A. Kean, Journal of Applied Physics, **120**, 205102 (2016)
2. "Temperature dependence of the bandgap of zinc nitride observed in photoluminescence measurements", A. Trapalis, I. Farrer, K. Kennedy, A. Kean, J. Sharman, and J. Heffernan, Applied Physics Letters **111**, 122105 (2017).

Abstract

Zn_3N_2 has recently attracted research interest as a candidate for use in earth-abundant semiconductor devices. However, Zn_3N_2 is in a group of semiconductor materials that have not been studied extensively in past literature. As a result, this study is focused on the fundamental properties of Zn_3N_2 from a materials science point of view, with an emphasis on properties relevant to semiconductor applications.

The samples presented throughout this work were deposited by means of Reactive Sputtering and Molecular Beam Epitaxy. Samples with a wide range of material quality were obtained between these two techniques. The samples examined were polycrystalline in structure and highly doped due to intrinsic defects. The absorption onset for Zn_3N_2 samples varied in the range of 1.15-1.50 eV. Photoluminescence measurements on optimised samples further indicated that the bandgap of the films was in the energy region of 1.40 eV. Variations in the measured optical bandgap were attributed to the Burstein-Moss effect for highly doped samples. A parabolic approximation of the conduction band suggested an intrinsic bandgap of ~ 1.10 eV. Furthermore, tuning of the optical properties of Zn_3N_2 was demonstrated in the form of a II-III-V AlZnN alloy. By increasing the Al content in the ternary films, an increase of the bandgap of AlZnN up to 2.76 eV was demonstrated.

Finally, a method for improving the ambient stability of Zn_3N_2 thin films is discussed. It was found that ex-situ thermal annealing improved the stability of the Zn_3N_2 films dramatically. The mechanism suggested to explain these observations is an improvement in the structural quality of the native oxide caused by the annealing process. The improvement in stability was gradual for annealing temperatures up to 400 °C examined here. This is a promising method as it improves the stability of Zn_3N_2 layers significantly by utilising the native oxide and does not require the growth of any capping layers.

Chapter 1: Introduction

1.1. Semiconductor materials and devices

Semiconductor devices are at the core of the electronics industry which is occupied with the fabrication of integrated circuits used in computers and other electronics devices, as well as the photonics industry which is involved in the production of lasers, light emitting diodes (LEDs), solar cells, and photodetectors amongst other devices. These devices make use of the electronic or optoelectronic properties of semiconductor materials.

Semiconductor devices consist of multilayer heterostructures of semiconductors and their alloys (e.g. GaAs, AlGaAs, InGaAs). The electrical properties of the semiconductor layers, i.e. the parameters describing charge transport and free charge carriers within these layers, are vital to the performance of the devices. In an intrinsic semiconductor, a minimum number of thermally activated charge carriers are present at any non-zero temperature. Additional free charge carriers (electrons and holes) may be introduced into a material by structural defects and impurities (including dopants) in the crystal structure. Low charge carrier concentrations are often desirable in semiconductor layers, so that the carrier diffusion length can be maximised throughout the semiconducting layers. As a result, high purity materials (intrinsic semiconductors) are necessary in many semiconductor devices. Such high-quality layers are grown by Physical Vapour Deposition (PVD) or Chemical Vapour Deposition (CVD) techniques such as Molecular Beam Epitaxy (MBE) and Metal-organic Vapour Phase Epitaxy (MOVPE) respectively. Through these growth techniques, intrinsic semiconductors can be intentionally doped with electrons and holes by introducing impurities in a controlled manner.

To cover a wide range of applications, a plethora of semiconductor materials with different properties have been developed. In addition, new materials that may fit the requirements of specific applications are continuously being investigated. Semiconductor materials can be grouped in two categories: elemental semiconductors, and compound semiconductors. Elemental semiconductors are composed of a single species of atoms and include Group IV elements Si and Ge, and Group VI elements Se, and Te (**Figure 1.1**). Si was one of the earliest semiconductors to be investigated and continues to have major applications today, e.g. in the electronics and solar cell industries.[1,2] Compound

semiconductors are semiconductor materials that are composed of more than one elements of the periodic table. Although there are many known compound semiconductor materials, the electronics and optoelectronics industries have focused on specific materials systems because of their electric and optical properties. Group III-V (e.g. (Al, Ga, In)As, (Al, Ga, In)N) and Group II-VI (e.g. Zn(S, Se, Te), Cd(S, Se, Te)) semiconductors are arguably amongst the most researched and better understood semiconductor materials, and have many commercial applications in LEDs, lasers, solar cells, detectors, etc.[3] Other interesting semiconductor materials are formed from Group II-V and Group II-IV-V elements, such as Zn_3N_2 or Zn(Sn, Ge)N_2. Although some Group II-V semiconductors (e.g. Zn_3(P, As, Sb)$_2$, Cd_3(P, As, Sb)$_2$) have attracted interest for a variety of applications in the past, research on these materials has been done on a smaller scale when compared to group III-V semiconductors.[4-6] That is also true for zinc nitride (Zn_3N_2), the Group II-V semiconductor on which this work is focused.

Figure 1.1: Groups II to VII of the periodic table. Modified from http://www.ptable.com/

1.2. Zinc Nitride and Zn-IV-Nitrides

Zinc Nitride (Zn_3N_2) has recently attracted research interest in the search for earth-abundant, low-cost materials to be used as alternatives to other semiconductor materials.[7-12] Zn-IV-Nitrides, such as $ZnSnN_2$ and $ZnGeN_2$, have also recently attracted interest for

use as solar absorbers.[13-15] $ZnSnN_2$ has a bandgap of 1.4 eV, and $ZnGeN_2$ has a bandgap of 3.3 eV, whereas the bandgap of Zn(Ge, Sn)N_2 alloys is tuneable within that range. Although Zn-IV-N_2 are not studied in this work, they are related to Zn_3N_2 and are at a similar level of development.

Zn_3N_2 samples have been observed experimentally to have strong absorption and a narrow bandgap, making Zn_3N_2 a candidate for use as a solar absorber. Furthermore, Zn_3N_2 has demonstrated electrical properties that indicate it is a promising candidate for the development of low-cost high-mobility devices. For instance, relatively high charge carrier mobilities have been measured in polycrystalline samples with very high levels of doping. This is an interesting observation for two reasons:

a) Polycrystalline materials can be deposited by low-cost techniques such as sputtering on non-lattice matched substrates. As a result, costs associated with epitaxial growth are minimised if epitaxy is not necessary. In addition, Zn_3N_2-based semiconductor devices could be fabricated on amorphous or flexible substrates (because of low deposition temperatures) while maintaining device performance.
b) Because mobility usually increases at low doping levels, the carrier mobility of Zn_3N_2 could be comparable to other high-mobility semiconductors at intrinsic doping levels.

However, Zn_3N_2 is at an early stage of development and many of its properties are not yet fully understood. Aspects of Zn_3N_2 that are still open to debate include its bandgap, which is arguably one of the most important properties of a semiconductor especially for photonics. There is a controversy in the published literature about the exact value of the bandgap of Zn_3N_2, with experimental reports ranging from 0.9 to 3.3 eV.[16-19] Similar controversies have emerged in other semiconductor materials in the past. For instance, there was an uncertainty surrounding the bandgap of InN several years ago. The bandgap of InN was eventually determined to be 0.7 eV, instead of 2.3 eV which was initially reported.[20-24] Oxygen contamination and the Burstein-Moss effect were responsible for the observed bandgap broadening. Other nitrides such as ScN and $ZnSnN_2$ have also had similar discrepancies in their reported bandgaps.[14,25] These previous studies indicate that material quality is an important factor when determining basic material properties. In the case of Zn_3N_2, the bandgap controversy has not been resolved to date. Furthermore, the reported range of 0.9 to 3.3 eV is unusually high even when compared to materials which have had similar issues. As a result, there are recent publications discussing the suitability of Zn_3N_2

for applications as a solar absorber (narrow bandgap)[6], and as a transparent conducting nitride (wide bandgap).[26,27] Some of the possible explanations for the discrepancies in experimental reports are discussed in Chapter 2.

A particular challenge in the development of Zn_3N_2 as a semiconductor has been the high levels of unintentional doping observed experimentally.[26,28,29] It is common for Zn_3N_2 samples to be unintentionally doped with degenerately high carrier concentrations, often in the range of 10^{18}-10^{20} cm^{-3}. Although the origin of the high doping levels in Zn_3N_2 samples is not yet fully understood, based on computational studies, nitrogen vacancies and oxygen doping are thought to be the main causes.[30,31] Decreasing the doping levels in Zn_3N_2 samples to intrinsic levels remains one of the greater challenges associated with this material, as even single-crystal samples have been reported with very high levels of unintentional doping.[9]

Finally, the stability of Zn_3N_2 is an important topic in related literature. Zn_3N_2 is known to readily react with oxygen and water in ambient environments. The oxidation reactions are not self-limiting and can result in the complete conversion of Zn_3N_2 samples to ZnO or zinc hydroxide. Therefore, finding ways to improve the stability of Zn_3N_2 with encapsulation or other methods, is a necessary step if it is to be used in semiconductor devices. Interestingly enough, the ambient stability of Zn(Sn, Ge)N_2 materials does not seem to be an issue, possibly because of their different crystal structures. The oxidation process as well as ways to improve stability have been investigated in this work and are discussed in Chapter 7.

1.3. Thesis outline

This work investigates the properties of zinc nitride materials. To this end, physical vapour deposition processes to deposit zinc nitride films were developed. More specifically, Zn_3N_2 growth by Reactive Sputtering and Molecular Beam Epitaxy were investigated. Some of the most significant novel contributions of this work are on the discussion of the bandgap energy by analysis of absorption coefficient and photoluminescence measurements, and the investigation of a materials system for zinc nitride heterostructures based on the formation of wide-bandgap AlZnN semiconductor alloys, which have been demonstrated for the first time here.

Chapter 1 serves as an introduction to the topic and scope of this thesis.

Chapter 2 is a literature review focused on Zn_3N_2 and what is at present known about its properties. Known approaches to synthesising or depositing Zn_3N_2 are also discussed.

Chapter 3 discusses the characterisation and deposition techniques used in experiments. Experimental methodologies used to analyse data are explained in this chapter.

Chapter 4 discusses the properties of Zn_3N_2 samples deposited by a reactive sputtering process.

Chapter 5 discusses the growth of Zn_3N_2 by MBE, and the properties observed in the grown films.

Chapter 6 highlights initial results on tuning of the optical properties of Zn_3N_2 in an aluminium zinc nitride semiconductor alloy deposited by reactive sputtering.

Chapter 7 discusses the effects of thermal annealing on the stability of the deposited Zn_3N_2 materials and other measured properties.

Chapter 8 discusses a process to deposit Zn_3N_2 nanoparticles by a gas phase aggregation technique.

Chapter 9 lists the conclusions and highlights steps for further research on this topic.

1.4. Bibliography

[1] G. T. Reed, Nature **427,** 595 (2004).

[2] S. R. Wenham and M. A. Green, Progress in Photovoltaics: Research and Applications **4,** 3 (1996).

[3] G. Roelkens, L. Liu, D. Liang, R. Jones, A. Fang, B. Koch, and J. Bowers, Laser & Photonics Reviews **4,** 751 (2010).

[4] N. C. Wyeth and A. Catalano, Journal of Applied Physics **50,** 1403 (1979).

[5] G. Shen and D. Chen, Nanoscale Research Letters **4,** 779 (2009).

[6] M. Ullah, G. Murtaza, M. Yaseen, and S. A. Khan, Journal of Alloys and Compounds (2017).

[7] C. G. Núñez, J. L. Pau, M. J. Hernández, M. Cervera, and J. Piqueras, Applied Physics Letters **99,** 232112 (2011).

[8] C. G. Núñez, J. L. Pau, M. J. Hernández, M. Cervera, E. Ruiz, and J. Piqueras, Thin Solid Films **520,** 1924 (2012).

[9] W. Peng, T. Tiedje, H. Alimohammadi, V. Bahrami-Yekta, M. Masnadi-Shirazi, and W. Cong, Semiconductor Science and Technology **31,** 10LT01 (2016).

[10] S. R. Bhattacharyya, R. Ayouchi, M. Pinnisch, and R. Schwarz, physica status solidi (c) **9,** 469 (2012).

[11] C. G. Núñez, J. L. Pau, E. Ruiz, and J. Piqueras, Applied Physics Letters **101,** 253501 (2012).

[12] S. Sinha, D. Choudhury, G. Rajaraman, and S. K. Sarkar, RSC Advances **5,** 22712 (2015).

[13] N. Feldberg, J. D. Aldous, W. M. Linhart, L. J. Phillips, K. Durose, P. A. Stampe, R. J. Kennedy, D. O. Scanlon, G. Vardar, R. L. Field, T. Y. Jen, R. S. Goldman, T. D. Veal, and S. M. Durbin, Applied Physics Letters **103,** 042109 (2013).
[14] L. Lahourcade, N. C. Coronel, K. T. Delaney, S. K. Shukla, N. A. Spaldin, and H. A. Atwater, Advanced Materials **25,** 2562 (2013).
[15] S. Chen, P. Narang, H. A. Atwater, and L.-W. Wang, Advanced Materials **26,** 311 (2014).
[16] T. Yang, Z. Zhang, Y. Li, M. Lv, S. Song, Z. Wu, J. Yan, and S. Han, Applied Surface Science **255,** 3544 (2009).
[17] S. Simi, I. Navas, R. Vinodkumar, S. R. Chalana, M. Gangrade, V. Ganesan, and V. P. M. Pillai, Applied Surface Science **257,** 9269 (2011).
[18] M. Futsuhara, K. Yoshioka, and O. Takai, Thin Solid Films **322,** 274 (1998).
[19] P. N. Taylor, M. A. Schreuder, T. M. Smeeton, A. J. D. Grundy, J. A. R. Dimmock, S. E. Hooper, J. Heffernan, and M. Kauer, Journal of Materials Chemistry C **2,** 4379 (2014).
[20] V. Y. Davydov, A. A. Klochikhin, R. P. Seisyan, V. V. Emtsev, S. V. Ivanov, F. Bechstedt, J. Furthmüller, H. Harima, A. V. Mudryi, J. Aderhold, O. Semchinova, and J. Graul, physica status solidi (b) **229,** r1 (2002).
[21] J. Wu, W. Walukiewicz, K. M. Yu, J. W. Ager, E. E. Haller, H. Lu, W. J. Schaff, Y. Saito, and Y. Nanishi, Applied Physics Letters **80,** 3967 (2002).
[22] J. Wu, Journal of Applied Physics **106,** 011101 (2009).
[23] T. Matsuoka, H. Okamoto, M. Nakao, H. Harima, and E. Kurimoto, Applied Physics Letters **81,** 1246 (2002).
[24] J. Wu, W. Walukiewicz, W. Shan, K. M. Yu, J. W. Ager, S. X. Li, E. E. Haller, H. Lu, and W. J. Schaff, Journal of Applied Physics **94,** 4457 (2003).
[25] R. Deng, B. D. Ozsdolay, P. Y. Zheng, S. V. Khare, and D. Gall, Physical Review B **91,** 045104 (2015).
[26] X. Cao, Y. Ninomiya, and N. Yamada, physica status solidi (a) **214,** 1600472 (2017).
[27] J. Jia, H. Kamijo, S. Nakamura, and Y. Shigesato, MRS Communications**,** 1 (2018).
[28] G. Z. Xing, D. D. Wang, B. Yao, L. F. N. A. Qune, T. Yang, Q. He, J. H. Yang, and L. L. Yang, Journal of Applied Physics **108,** 083710 (2010).
[29] H. Gao, X. Zhang, Y. Zhao, and B. Yan, AIP Advances **7,** 035311 (2017).
[30] N. Jiang, J. L. Roehl, S. V. Khare, D. G. Georgiev, and A. H. Jayatissa, Thin Solid Films **564,** 331 (2014).
[31] Y. Kumagai, K. Harada, H. Akamatsu, K. Matsuzaki, and F. Oba, Physical Review Applied **8,** 014015 (2017).

Chapter 2: Literature Review of Zinc Nitride

2.1. Crystal structure

Zn_3N_2 has a cubic anti-bixbyite structure which has been studied in several computational and experimental studies.[1-4] The name anti-bixbyite originates from the mineral bixbyite (Mn_2O_3). The crystal structure of Zn_3N_2 (and other materials which exhibit this structure, such as Mg_3N_2) is identical to that of bixbyite but with reversed ion positions.[1] In the anti-bixbyite crystal structure of Zn_3N_2, N atoms form a cubic close packed framework and Zn atoms occupy the tetrahedral interstitial sites. The crystal structures of Zn, ZnO and Zn_3N_2 are shown in **Figure 2.1a-c**. The X-ray Diffraction (XRD) patterns corresponding to these structures are also shown **Figure 2.2**. The diffraction peaks of all crystal planes that may be observed in the range of 30-80° are shown on these graphs, as they may be found in powder XRD. Based on a lattice of 80 atoms and a cubic lattice of 9.76 Å, the theoretical density of Zn_3N_2 is calculated at 6.46 g/cm^3, which is close to the value of 6.2 g/cm^3 measured by Cao *et al.*[5] by X-ray Reflectivity (XRR) in reactively sputtered samples. Differences from the theoretical density are the result of a less than optimal structure in polycrystalline films, which result in the formation porous films.

The lattice constant of Zn_3N_2 (α = 9.76 Å) is relatively large compared to other semiconductor materials. As a result, identifying an appropriate substrate for epitaxial crystal growth has been one of the challenges associated with Zn_3N_2. However, reports of epitaxial or oriented growth have shown up in literature. Oshima and Fujita reported the growth of (111)-oriented Zn_3N_2 on a-plane sapphire by Molecular Beam Epitaxy (MBE).[6] In a more recent study, Wu *et al.* reported the growth of single crystal (100)-Zn_3N_2 on a-plane sapphire and (100)-MgO substrates by MBE.[7] Their high resolution XRD measurements revealed the presence of a single feature, the (400) peak of the Zn_3N_2 structure. Analysis of the full-width half-maximum (FWHM) of the peaks suggested that the samples grown on MgO had a better structural quality. Finally, Cao *et al.* reported epitaxial growth of (100)-Zn_3N_2 on yttria-stabilised zirconia (YSZ) by reactive sputtering in a narrow window of growth conditions.[8] For all YSZ, MgO and a-plane sapphire, epitaxial growth is based on the matching of the substrate atom positions with the half-lattice of Zn_3N_2, as their lattice constants are approximately half that of Zn_3N_2.

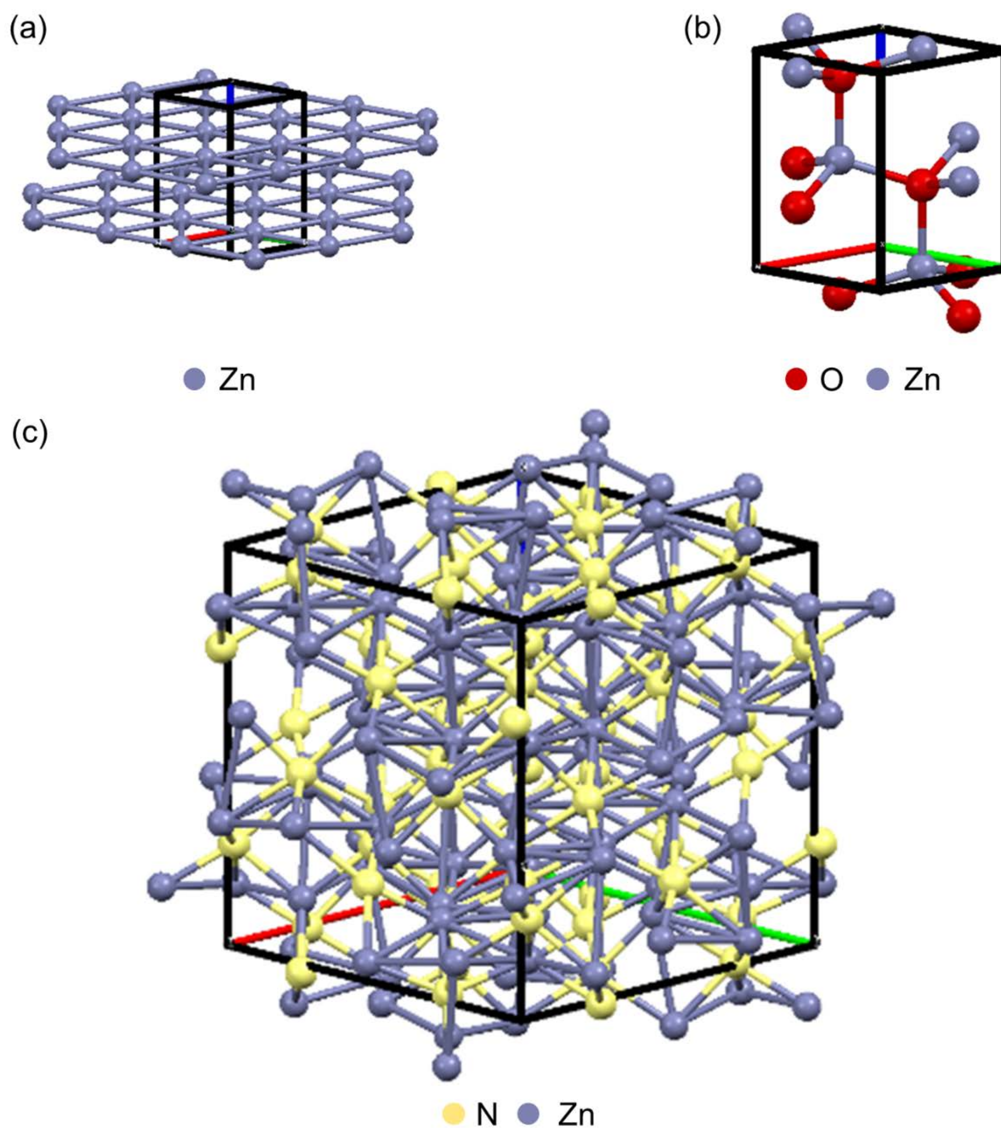

Figure 2.1: Crystal structures of (a) Zn, (b) ZnO and (c) Zn_3N_2.

Computational studies suggest that native point defects (N, Zn vacancies and interstitials) can be relatively easily formed in the lattice, as their formation is thermodynamically favoured.[2] Specifically, N vacancies are more likely to be formed in N-poor conditions and Zn vacancies are more likely to be formed in N-rich conditions compared to interstitial defects.[3] As a result, a large defect density is found in Zn_3N_2 samples studied in literature. The presence of these defects is evident in the electrical properties of Zn_3N_2 which are discussed next.

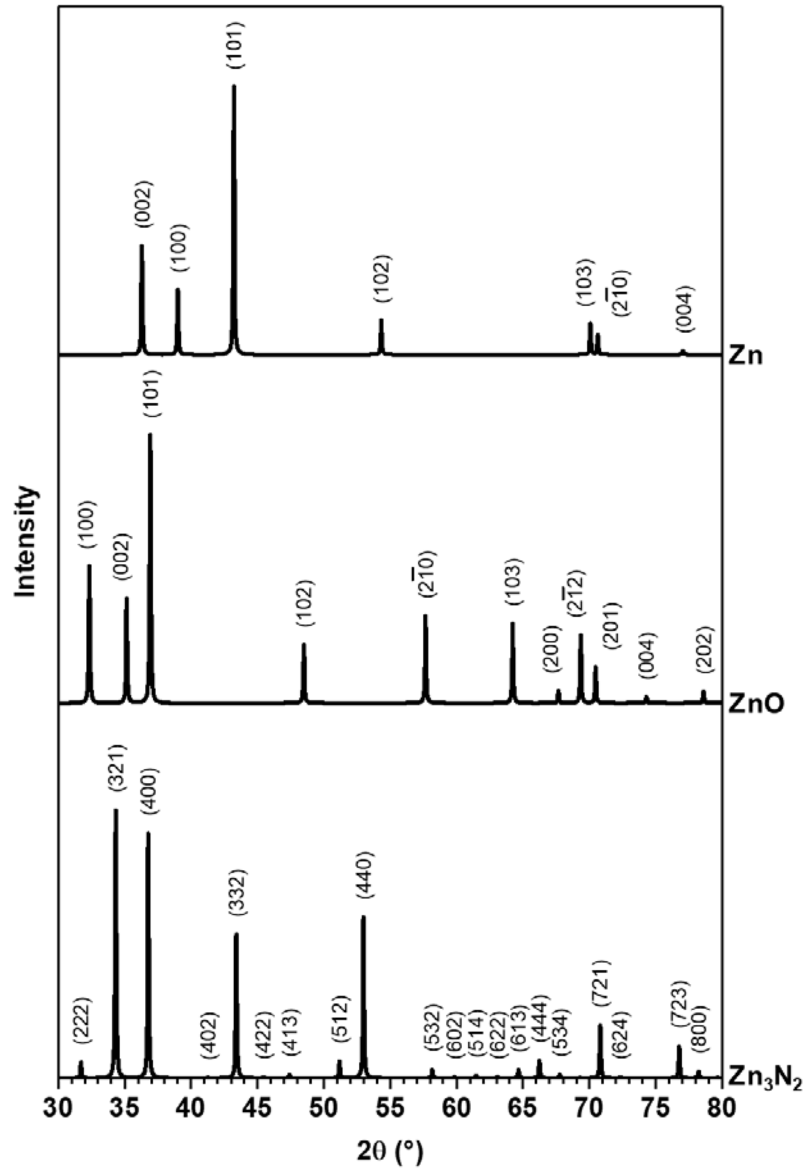

Figure 2.2: XRD patterns of Zn, ZnO and Zn_3N_2 based on their known structures.[1,9,10] Peak positions were calculated for $\lambda_{CuK\alpha} = 1.54056$ Å.

2.2. Charge transport properties

The electrical properties of semiconductors are primarily determined by the band structure of the material. As a result, the charge transport properties of different semiconductors vary significantly. A fundamental material-specific parameter that determines the mobility of electrons is their effective mass, $m*$. A low electron effective mass, such as that of GaAs, results in high carrier mobility.[11] This improves device performance and renders materials suitable for a variety of applications in electronics. The

mobility of charge carriers in semiconductors may be reduced by scattering mechanisms, such as scattering at ionised or neutral defects or impurities.

Native point defects such as vacancies and interstitials may introduce free charge carriers to the density of states. Similarly, impurity atoms introduce free electrons or holes depending on the type of impurity. In heavily doped semiconductor materials, the concentration of charge carriers typically determines their mobility through scattering mechanisms, which in turn affects the performance of semiconductor devices.

The electrical properties reported for Zn_3N_2 samples indicate they are highly doped. The charge carrier concentration, n_e, of Zn_3N_2 samples in literature is in the order of 10^{18}-10^{20} cm^{-3}. At these carrier concentrations, Hall mobilities, μ_H, in the range of 10^0-10^3 $cm^2 \cdot V^{-1} \cdot s^{-1}$ have been reported, whereas the resistivity ρ of such samples is in the order of 10^{-3}-10^{-2} $\Omega \cdot cm$. One of the interesting properties of Zn_3N_2 is the observation of high mobilities even at high carrier concentrations. Cao *et al.*[8] investigated the electron effective mass in Zn_3N_2 and its dependence on the charge carrier concentration. They found that the electron effective mass in their samples ranged from $0.16m_e$ to $0.37m_e$ and increased with the charge carrier concentration (where m_e is the free electron mass). Similar values have been reported by Suda and Kakishita and other studies.[12,13] In degenerately doped semiconductors, an increase of the effective electron mass with charge carrier concentration is attributed to a nonparabolicity of the conduction band and an increase of the Fermi level.[14] Cao *et al.* extrapolated from their data that the effective electron mass at the conduction band in intrinsic Zn_3N_2 is $m_0^* = (0.08 \pm 0.03)\ m_e$. This is a relatively low value which is comparable to that of InN. In the same study, Cao *et al.* also discussed the electron transport mechanisms in epitaxial and polycrystalline Zn_3N_2 and concluded that in their highly doped Zn_3N_2 samples carrier mobility was governed by ionized impurity scattering.[5]

The conductivity type of Zn_3N_2 is exclusively n-type in the published literature. Computational studies have suggested that the n-type conductivity is associated with N vacancies in the lattice which introduce free electrons.[3] In contrast, it has been suggested that Zn vacancies introduce free holes and result in p-type conductivity. However, p-type conductivity has not been reported to date, despite the range of techniques and conditions used to form Zn_3N_2. An explanation for the n-type conductivity even in Zn_3N_2 samples with a high structural quality is the presence of oxygen, which is thought to be an n-type dopant in Zn_3N_2. Unintentional oxygen doping of Zn_3N_2 has been observed experimentally in several studies making it evident that oxygen is easily incorporated into the lattice even

under high vacuum conditions.[6,12,15-18] Therefore, although Zn_3N_2 films have been shown to have promising electrical properties, the inability to lower the levels of unintentional doping, and to generate p-type conductivity are some of the issues that have prevented further development of this material.

2.3. Bandgap and refractive index

The bandgap and refractive index of a semiconductor material are amongst its most fundamental properties because they largely determine the applications for which it is suited. For instance, to cover a range of the electromagnetic spectrum in LEDs and lasers, different materials are used because of their different bandgaps which determine the emission frequency of the devices.

The discussion of determining optical properties is a major topic of interest for Zn_3N_2. The optical properties of a material may be determined experimentally or computationally. Among the experimental methods are optical techniques such as transmittance/reflectance measurements, and spectroscopic ellipsometry. In spectroscopic ellipsometry, the dielectric function of a layer in an optical system is modelled to derive its refractive index and absorption coefficient. While ellipsometry can be a very precise technique to determine the optical properties of a material, the bandgap observed in ellipsometric measurements may differ from the intrinsic bandgap of the material because of effects such as the Burstein-Moss shift. The Burstein-Moss shift is an apparent increase of the bandgap observed in highly doped semiconductors, caused by partial filling of the conduction band by electrons.[19,20] As a result, other techniques such as photoluminescence measurements may be used to confirm the bandgap of a material. Computational studies also contribute to understanding the band structure of a material by calculating its electronic structure. These calculations are done with atomistic computational techniques such as density functional theory (DFT). However, because these techniques are computationally intensive, they are often truncated and may result in known errors.[3] To account for such issues, the band structure may be calculated with several different approaches. For instance, Yoo *et al.* calculated values for the bandgap of Zn_3N_2 in the range of 0-1.48 eV using various levels of approximation.[4] As a result, while computational studies can be very useful in better understanding new materials, they do not always provide a definite answer to questions regarding the band structure of semiconductors. With that said, most computational studies suggest Zn_3N_2 has a narrow bandgap of approximately 1 eV.[4,21,22] Furthermore, Kumagai

et al. argued that the Burstein-Moss effect can only account for variations of the bandgap of up to ~1.7 eV in their predicted narrow bandgap electronic structure.[21]

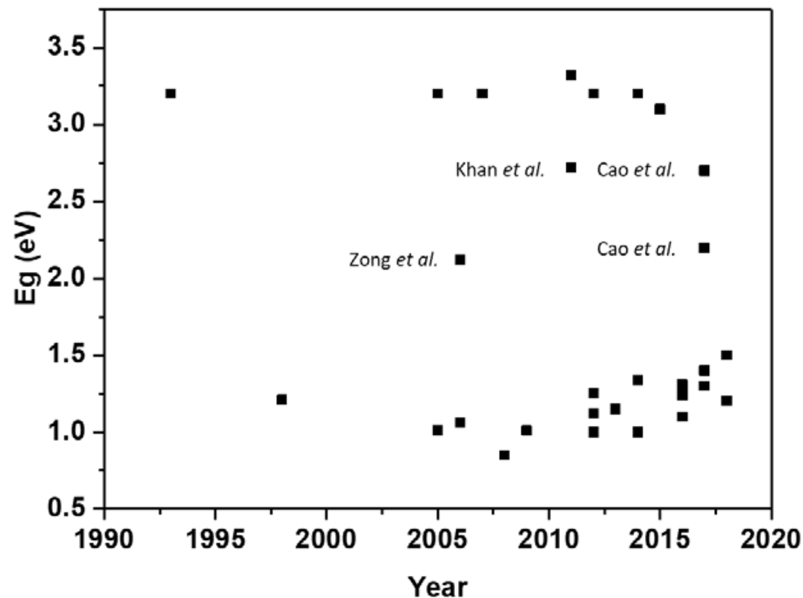

Figure 2.3: Optical bandgap values reported for Zn_3N_2 over time. This graph indicates the disparity between narrow and wide bandgap reports. The labeled data points highlight studies which have reported intermediate bandgap values.

Experimental reports for the optical properties of Zn_3N_2 are more controversial. Núñez et al. reported a refractive index of 2.0-2.8 determined by spectroscopic ellipsometry measurements on sputtered Zn_3N_2 thin films.[23] Jiang et al. reported similar results with a refractive index of 2.6-2.8.[24] Both studies reported a narrow bandgap in the region of 1.25 eV. Another study by Ayouchi et al. reported a lower refractive index of 1.7-2.4 and a bandgap of approximately 3.2 eV by modelling ellipsometry measurements of PLD grown Zn_3N_2 films.[25] These studies are indicative of the wide range of optical properties reported in Zn_3N_2 samples. Optical bandgaps ranging from 0.9 to 3.3 eV have been reported in experimental studies for Zn_3N_2 samples, which is an unusually wide degree of variability.[5,26,27] It can be argued that most studies are at the extremes of this range, whereas samples with intermediate bandgaps within that range are less common. This is demonstrated in **Figure 2.3**, which shows the bandgap values reported for Zn_3N_2 by year of publication. It is evident that most bandgap reports for Zn_3N_2 are either in the range of 1.0-1.5 eV or in the range of 3.0-3.3 eV.

The controversy regarding the optical bandgap of Zn_3N_2 is not yet settled and there are arguments on both sides. In some cases, the differences in the reported optical properties are attributed to the different fabrication methods and material quality in each study. Cao

et al. suggested that absorption in the visible region of the spectrum is caused by the formation of N interstitials.[5] More specifically, they suggest that the formation of a bond between a lattice N and an interstitial N introduces a half-filled N 2p state in the band structure so that defect-to-band transitions can occur. Therefore, by that argument, an excess of interstitial N defects results in a narrowing of the observed bandgap. In the papers of Cao *et al.*, optical bandgaps in the range of 2.2-2.8 eV are reported, varying because of a Burstein-Moss shift at high doping levels.

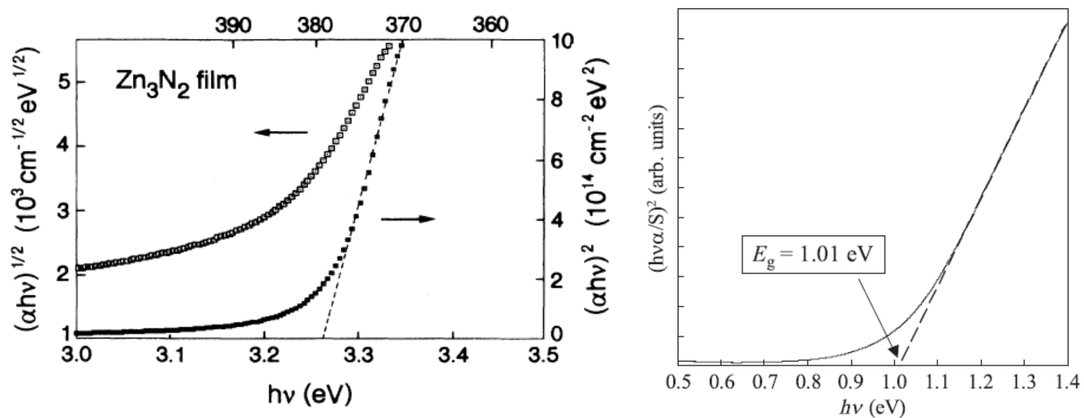

Figure 2.4: Absorption plots used to measure the optical bandgap of Zn_3N_2 samples from transmittance and reflectance measurements.[17,28] The graph on the left is from a study which reported a wide bandgap, whereas the graph on the right is from a study which reported narrow bandgap.

On the other hand, one of the possible explanations for the larger reported bandgaps of Zn_3N_2 may be related to its tendency to be converted to ZnO in ambient.[15,29] It is well-known that Zn_3N_2 is oxidised in ambient atmosphere, to the point of full conversion to ZnO. ZnO is a transparent semiconductor with a bandgap of approximately 3.3 eV and a refractive index of 1.8-2.0. Therefore, it would be difficult to distinguish between the optical properties of the wide bandgap Zn_3N_2 reported in some studies and those of ZnO. This suggests that some wide bandgap reports are likely the result of unintentional oxidation of Zn_3N_2 films to ZnO. This argument is re-examined in Chapter 4 with the use of experimental data.

Finally, in most experimental studies the optical bandgap is estimated by analysis of the absorption coefficient calculated from optical measurements. Examples of absorption plots used to estimate the optical bandgap are shown in **Figure 2.4** for both narrow and wide bandgap Zn_3N_2 samples. It should be noted that interpreting absorption spectra and absorption plots like those shown in **Figure 2.4** can be ambiguous based on the shape of the absorption coefficient.[30] As a result, misinterpretation of the absorption spectra is

another factor which may contribute to the range of reported bandgaps. The interpretation of experimental absorption plots is discussed further in Chapter 4.

2.4. Chemical synthesis approaches

Chemical synthesis of Zn_3N_2 powder accounts for a significant portion of the early published literature on Zn_3N_2. For this reason, the different approaches that have been reported are briefly reviewed here.

2.4.1. Ammonolysis of zinc and zinc compounds

The synthesis of Zn_3N_2 by ammonolysis, commonly referred to as nitridation in publications, involves a reaction of zinc or a zinc compound with ammonia conducted in a liquid or gas phase.[31,32] One of the earliest references of Zn_3N_2 is in the work of C.L. Bloxam on experimental chemistry published in 1903.[33] The following set of reactions which result in the formation of Zn_3N_2 are briefly described:

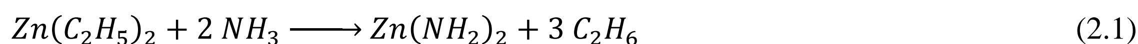

$$Zn(C_2H_5)_2 + 2\,NH_3 \longrightarrow Zn(NH_2)_2 + 3\,C_2H_6 \quad (2.1)$$

$$3\,Zn(NH_2)_2 \longrightarrow Zn_3N_2 + 4\,NH_3 \quad (2.2)$$

In this chemical process, diethyl zinc reacts with ammonia to form zinc diamine. Upon heating and out of contact with air, zinc diamine is reportedly converted to Zn_3N_2. It is mentioned in Bloxam's report that the Zn_3N_2 powder decomposed exothermically in the presence of water. The following reaction is suggested for the conversion of Zn_3N_2:

$$Zn_3N_2 + 3\,H_2O \longrightarrow 2\,NH_3 + 3\,ZnO \quad (2.3)$$

Another report of the nitridation of zinc was published in 1921 by W.J. Savoye in a thesis titled *"Zinc Nitride: Its Formation Properties and Alloys"*.[34] Savoye's thesis explored a variety of process conditions for the nitridation of Zn powder in ammonia. The following reaction was given for the formation of Zn_3N_2:

$$3\,Zn + 2\,NH_3 \longrightarrow Zn_3N_2 + 3\,H_2 \quad (2.4)$$

More recent publications on the synthesis of Zn_3N_2 by nitridation apply the same reactions. The nitridation reaction is typically carried out at temperatures of 400 °C or higher using ammonia flow rates in the order of 500 sccm (standard cubic centimetres per minute). The reactions are carried out for a duration of 2-4 h. An optimal reaction temperature is often reported at around 600 °C, whereas higher reaction temperatures have been reported to lead to the formation of a ZnO crystal phase.[16,35] A study of the thermal stability of Zn_3N_2

powder by Zong *et al.* indicated Zn_3N_2 is unstable in the presence of air at temperatures greater than 500 °C.[16] Several authors have reported the formation of ZnO and even a complete conversion of the product to ZnO after prolonged heating under ammonia.[16,35,36] The following reaction describes the conversion of Zn_3N_2 to ZnO in the presence of oxygen:

$$2\, Zn_3N_2 + 3\, O_2 \longrightarrow 6\, ZnO + 2\, N_2 \qquad (2.5)$$

Zn_3N_2 powder prepared by nitridation may have a microstructure of hollow spheres, nanowires or nanoneedles, subject to the process conditions and preparation of the zinc powder.[31,32,37,38] Scanning electron microscopy (SEM) images of these structures are shown in **Figure 2.5a-d**. The formation of hollow spheres has been explained by the initial formation of a Zn_3N_2 crust on the zinc particles.[32,39] Hollow spheres are then formed as zinc evaporates from these structures at high temperatures. A schematic of the formation process is demonstrated in **Figure 2.5e**. Khan *et al.* have demonstrated a variation of the nitridation process conducted in a solution of aqueous ammonia, from which similar structures were obtained.[40]

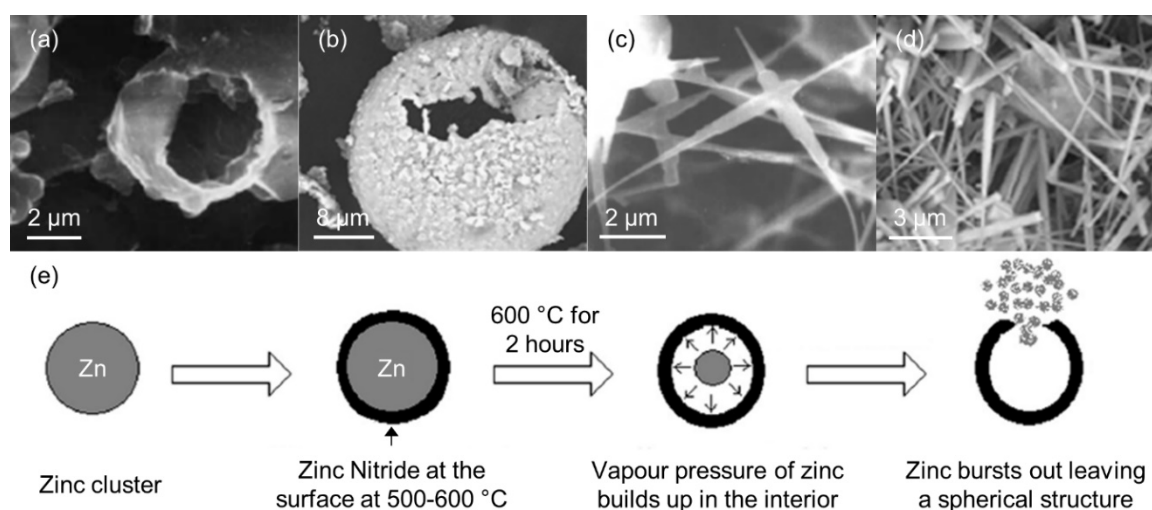

Figure 2.5: SEM images of Zn_3N_2 (a, b) hollow sphere microstructures and (c, d) nanowires and nanoneedles as seen in literature.[31,32,37,38] (e) A schematic representation of the proposed mechanism for the formation of the hollow spheres, modified from Zong *et al.*[37]

A Chemical Vapour Deposition (CVD) process reported by Wei, Tong *et al.* is similar in principle as it uses ammonia gas and zinc powder as the nitrogen and zinc sources respectively.[41] Wei, Tong *et al.* reported CVD growth using a reaction temperature of 680 °C which resulted in the formation of Zn_3N_2 microtips. SEM images of the microtips are shown in **Figure 2.6**.

The images in **Figure 2.6** also demonstrate changes in the morphology of the Zn_3N_2 films after exposure to ambient air for 3 days. This is a result of oxidation, which is a

recurring topic in the literature of Zn_3N_2. Reports of the unintentional oxidation of Zn_3N_2 indicate the requirement for a high-purity gas phase and overall environment in the experimental setup. The concern of oxygen contamination is also relevant for the discrepancies in the reported properties of Zn_3N_2 samples, which are thought to be influenced by the formation of zinc oxynitrides (ZnO:N).[29,42,43]

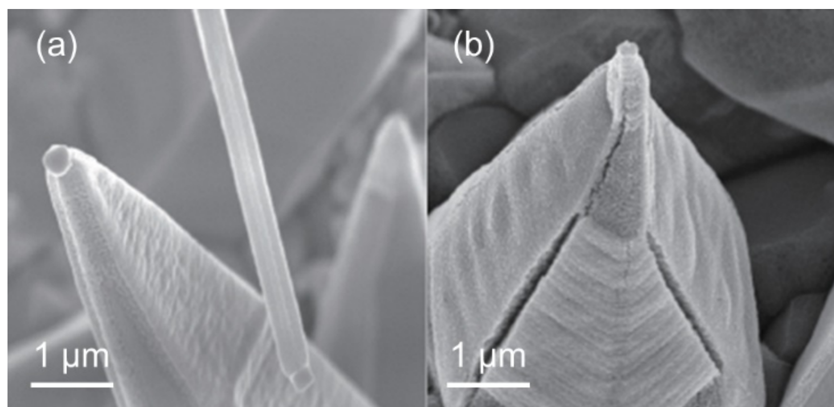

Figure 2.6: Zn_3N_2 microtips grown by thermal CVD (a) as deposited and (b) after exposure to ambient air for 3 days.[41]

2.4.2. Other experimental techniques

Variations of the reactions in (2.1) and (2.2) have been applied in several studies with different growth techniques, such as atomic layer deposition, chemical vapour deposition, and solvent-based chemical reactions. For instance, Taylor *et al.* published a process based on the use of diethyl zinc in a mixture of 1-octadecene and oleylamine.[44] In their experiment, ammonia gas was bubbled through the solution at 225 °C and diethyl zinc was added at a controlled rate. This resulted in the formation of Zn_3N_2 nanoparticles with diameters in the range of 2-7 nm. The size of the nanoparticles could be controlled by varying the addition rate of diethyl zinc. A transmission electron microscopy (TEM) image of the Zn_3N_2 nanoparticles prepared with this method is shown in **Figure 2.7a**.

Sinha *et al.* used diethyl zinc and ammonia gas as precursors to grow Zn_3N_2 on glass and Si substrates by atomic layer deposition (ALD).[45] In this experiment, the reactants were introduced to the reactor using N_2 as a carrier gas. Growth of Zn_3N_2 is facilitated by repeated cycles of the following surface-limited reactions:

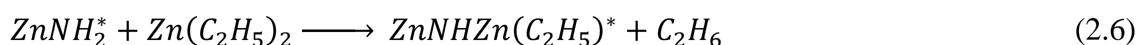

$$ZnNH_2^* + Zn(C_2H_5)_2 \longrightarrow ZnNHZn(C_2H_5)^* + C_2H_6 \quad (2.6)$$

$$ZnNHZn(C_2H_5)_2^* + NH_3 \longrightarrow ZnNHZnNH_2^* + C_2H_6 \quad (2.7)$$

where * indicates the surface species. The reactions were studied in the temperature range of 150-315 °C and indicated a maximum growth rate in the range of 175-215 °C.

Toyoura *et al.* reported the synthesis of Zn_3N_2 films by potentiostatic electrolysis of a zinc electrode in a molten LiCl – KCl – Li_3N salt at 400 °C.[17] In their experiment, zinc and aluminium plates were used as the working and reference electrodes respectively. A eutectic mixture of LiCl and KCl (59:41 mol%) mixed with 1 mol% of Li_3N was used as for the electrolysis. The Zn_3N_2 film is formed by means of potentiostatic electrolysis at 1.6 eV in the eutectic mixture. X-ray photoelectron spectroscopy (XPS) analysis showed that the surface of the samples was contaminated with $Zn(OH)_2$ and ZnO which they attributed to the reaction of Zn_3N_2 with oxygen, as described in (2.5), and water with the following reaction:

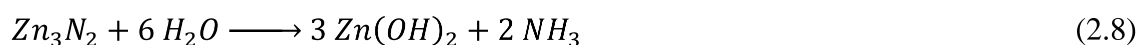

$$Zn_3N_2 + 6\,H_2O \longrightarrow 3\,Zn(OH)_2 + 2\,NH_3 \qquad (2.8)$$

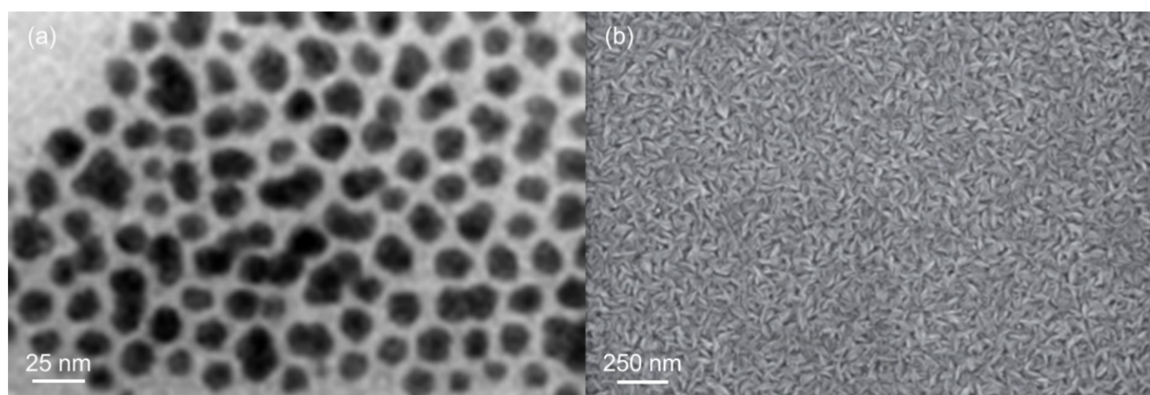

Figure 2.7: (a) TEM image of Zn_3N_2 nanoparticles prepared by Taylor *et al.*[44] (b) Surface of a polycrystalline Zn_3N_2 film grown by ALD.[45]

Furthermore, Wang *et al.* and Suda and Kakishita demonstrated metal-organic CVD (MOCVD) growth of Zn_3N_2 on Si, quartz and glass substrates using diethyl zinc and ammonia as reactants.[12,46] Wang *et al.* used a process pressure of 1066 Pa and a growth temperature of 450 °C. Suda and Kakishita used a pressure of 5000 Pa and growth temperatures in the range of 260-575 °C and achieved growth rates in the order of 4-30 nm/min. It is also mentioned that the growth rate increased with the growth temperature which suggests the MOCVD growth of Zn_3N_2 is limited by surface reactions.

Finally, Maile and Fischer reported the growth of Zn_3N_2 films on Si by MOCVD using bis[bis(trimethylsilyl)amido]zinc and ammonia as the precursors.[47] With this process, polycrystalline films are grown in the temperature range of 275-410 °C. At temperatures below 270 °C, film growth was not observed and at temperatures higher than 410 °C the films decomposed.

2.5. Physical vapour deposition

Previously reported processes for depositing Zn_3N_2 by Physical Vapour Deposition Techniques are outlined here. These include MBE, reactive sputtering and pulsed laser deposition (PLD) all of which use high purity metallic zinc as the source material. To deposit Zn_3N_2, these growth techniques involve the use of N_2 plasma as the source of active nitrogen species as well as a high-vacuum chamber.[24,26,48-52]

2.5.1. Molecular beam epitaxy

Suda and Kakishita, and Oshima and Fujita have demonstrated MBE growth of Zn_3N_2 films.[6,12] In both studies, Zn_3N_2 growth is achieved by the evaporation of zinc from a Knudsen cell in nitrogen plasma which is generated by radio-frequency (RF) power. The measured zinc beam flux was in the order of 0.5-7 nm/min. Films were grown on glass, quartz, and a-plane sapphire which had been thermally cleaned at 600-950 °C while the growth temperature varied in the range of 100-450 °C. In the experiments of Suda and Kakishita, growth at 450 °C resulted in the preferential orientation of (321) planes, whereas (400) orientation was obtained at lower growth temperatures. Oshima and Fujita reported the growth of (111)-oriented Zn_3N_2 on a-plane sapphire at 250 °C and calculated that the lattice mismatch between Zn_3N_2 and a-plane sapphire is approximately 6.5%, suggesting that a-plane sapphire is suitable for heteroepitaxial growth of Zn_3N_2.

In 2016, Peng *et al.* reported the single crystal growth of Zn_3N_2 (400) on a-plane sapphire and MgO (100) by MBE.[7] Epitaxial growth was obtained at low temperatures of 140-160 °C, whereas no growth was reported at temperatures higher than 270 °C. It is reasonable to expect single crystal growth to result in an improvement in material quality in terms of defects and impurities. While an improved Hall mobility was reported in these studies compared to other techniques, such as sputtering, the carrier concentration of the samples remained high (> 10^{18} cm^{-3}). The explanation given for the high levels of unintentional doping is related to unintentional oxygen doping from residual oxygen in the vacuum chamber and nitrogen vacancies in the crystal structure.

Reports of Zn_3N_2 samples prepared by MBE are relatively scarce in published literature, especially when compared to the number of studies performed on reactive sputtering processes. A list of the growth conditions in different MBE studies is shown in **Table 2.1**. Only some of the MBE studies have reported single crystal epitaxial samples.[6,7] However, the results that have been published so far report substrate temperatures in the

range of 140-450 °C during growth. These temperatures are low when compared to GaN or GaAs MBE processes, which tend to require much higher substrate temperatures, in the range of 500-800 °C.[53-55] The reported growth temperatures for Zn_3N_2 are similar to those used in other Zn-based MBE processes, such as those of ZnO, ZnSe, and $ZnSnN_2$.[56-58] Some of these studies have reported that the sticking coefficient of Zn at high temperatures is very low for many substrates. For instance, in the case of $ZnSnN_2$, a 20:1 ratio of Zn:Sn was used by Feldberg *et al.* so as to achieve stoichiometric epitaxial films.[58] The low growth temperatures reported for Zn_3N_2 MBE so far are likely related to the tendency for Zn to desorb from hot surfaces, which is a known issue in Zn-based MBE processes.[58-60]

Table 2.1: Details of MBE process parameters for Zn_3N_2 growth from previously published studies.

Substrate	Substrate Preparation	Substrate Temperature (°C)	Plasma Power (W)	Growth rate (nm/h)	Reference
a-plane sapphire	Thermal cleaning at 950 °C	200-400	300	8-20	6
quartz, glass	Thermal cleaning at 600 °C	100-450	250	30-420	12
a-plane sapphire, (100) MgO	Thermal cleaning at 800 °C	140, 160, 180	300	72-216	7

2.5.2. Reactive sputtering

Deposition of Zn_3N_2 by reactive sputtering constitutes a significant portion of recent Zn_3N_2 literature. As a result, a variety of growth conditions and substrates have been investigated. In most cases, the reactive sputtering of Zn_3N_2 involves the sputtering of a zinc target in N_2 plasma or plasma generated by a mixture of Ar and N_2 using flow rates in the range of 10-40 sccm. The films grown by sputtering tend to be more metallic at low N_2 concentrations and more N-rich at higher N_2 concentrations. The sputter power, which may be DC or RF, varies in the range of 25-350 W while the base pressure is usually in the range of 10^{-6} mbar, and the working pressure in the order of 10^{-3} mbar. **Table 2.2** displays a list of sputtering processing parameters in different studies. Common substrates used for deposition include quartz, glass, sapphire, and Si at temperatures up to 500 °C. The majority of the sputtered Zn_3N_2 are polycrystalline and have a grain morphology comparable to that shown in the SEM images in **Figure 2.8**.

Table 2.2: Details of sputtering process parameters for Zn_3N_2/ZnO:N film deposition from previously published studies.

Substrate	Target	Process gas	Power	Substrate Temperature (°C)	Pressure (mbar)	Reference
glass	Zn	Ar/N_2	70 W	150	7×10^{-3}	61
glass	Zn	Ar/N_2	75-90 W	Unheated	3×10^{-2}	62
glass	Zn	Ar/N_2	25 W	150	10^{-2}	26
glass	ZnO	Ar/N_2	100 W	150	N/A	42
sapphire, quartz	Zn	N_2	1.9 W/cm^2	Unheated	10^{-2}	63
quartz	Zn_3N_2	N_2	110 W	Unheated	10^{-2}	48
Si, glass	Zn_3N_2	Ar	100 W	Unheated	7×10^{-3}	64,65
quartz	Zn	Ar/N_2	50 W	200	10^{-2}	66
quartz	Zn	N_2	100 W	150-450	10^{-2}	49
Si, glass	Zn	Ar/N_2	25-200 W	25-250	10^{-2}	15,23,29,67,68
quartz, Si	Zn	Ar/N_2	2.14 W/cm^2	Unheated	10^{-2}	50,69
Si, glass	Zn	Ar/N_2	85 W	25-350	10^{-2}	18
Si	Zn	Ar/N_2	120 W	Unheated	10^{-2}	51
glass	Zn	Ar/N_2	350 W	Unheated	7×10^{-3}	52
quartz	ZnO	O/N_2	120 W	500	10^{-2}	70
YSZ	Zn	Ar/N_2	80	100-250	2×10^{-2}	8

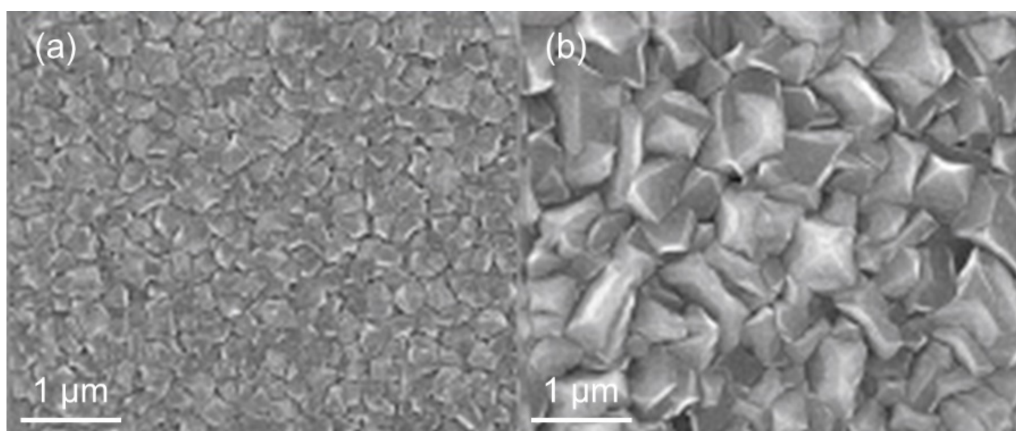

Figure 2.8: SEM images of polycrystalline Zn_3N_2 films grown by sputtering on (a) an unheated substrate and (b) a substrate temperature of 200 °C.[15]

The sputtering of a Zn_3N_2 target in Ar plasma has also been reported, however, these studies are few, due to the limited availability of Zn_3N_2 sputtering targets.[27,48,64] This is possibly related to the ambient stability of Zn_3N_2, as maintaining pristine Zn_3N_2 for extended periods of time requires storage in a vacuum environment. On a related note, a Zn or ZnO target is sometimes sputtered in a mixture of O/Ar/N_2 with the intention of growing nitrogen-doped ZnO films, or ZnO:N films.[42,43,70] The motivation behind the preparation of ZnO:N films is that they have been reported to have p-type conductivity, which is difficult to achieve in ZnO. The deposition of p-type ZnO is of interest for the fabrication of ZnO-based electronics. As a result, some of the studies referenced in this section only used Zn_3N_2 as a precursor which was subsequently oxidised to ZnO:N.

2.5.3. Pulsed laser deposition

Growth of Zn_3N_2 films by an RF-plasma assisted PLD process has been demonstrated independently by different authors.[25,71] PLD is carried out under high vacuum in a stainless-steel chamber with a base pressure in the order of 10^{-7} mbar. Ayouchi, Casteleiro *et al.* ablated a zinc target with a 1064 nm Nd:YAG laser. Samples were grown on quartz and sapphire substrates at a temperature of 400 °C. Simi, Navas *et al.* developed a process which used a ZnSe target instead of zinc, prepared by sintering ZnSe pellets at 1300 °C for 24 h. Both studies reported a wide band gap of about 3.3 eV.

2.6. Roadmap for applications

It should be evident by now that Zn_3N_2 is an interesting material and may have applications arising from its semiconducting properties. Based on the properties discussed here, there are three types of applications for which Zn_3N_2 seems like a good candidate:

a) as a catalyst in applications that require surface reactivity,
b) as a precursor for the fabrication of p-type ZnO in transparent electronics, and
c) as a low-cost, high mobility semiconducting layer in photonics devices using earth-abundant elements.

Considering that many catalytic and photocatalytic reactions depend on the reactivity of a surface, i.e. the presence of electrons and their ability to generate active species in chemical reactions, it seems likely based on what has been discussed so far that the surface of Zn_3N_2 could act as a catalyst. For instance, it is evident that the Zn_3N_2 surface readily reacts with oxygen and water molecules. Although the reactions of Zn_3N_2 with oxygen and

water are unwanted because they convert the material to another medium, they are an indication that Zn_3N_2 is highly reactive. Initial steps towards investigating the catalytic activity of the Zn_3N_2 surface have been taken by C.T. Li *et al.* who tested the performance of several Zn compounds as counter electrodes in dye-sensitised solar cells.[72] C.T. Li *et al.* found that Zn_3N_2 had the highest photovoltaic performance compared to the other Zn compounds (ZnO, ZnS, and ZnSe), and also compared to a Pt-based electrode. The improved electrocatalytic performance of Zn_3N_2 was attributed to its narrow bandgap (1.05 eV), which facilitates the excitation of electrons to the conduction band.

The fabrication of p-n junctions in ZnO materials is an important step for the development of transparent electronics. Evidently, the thermal oxidation of Zn_3N_2 samples results in the formation of N-doped ZnO films with p-type conductivity, which has previously proven to be a challenge in the development of ZnO-based electronics. The use of Zn_3N_2 as a precursor for p-type ZnO has been demonstrated in several experimental studies, where the conditions for obtaining p-type ZnO have been investigated.[61-64]

In the case of photonic devices, potentially the most suitable application for Zn_3N_2 is that of thin film solar cells. Thin films solar cells based on Zn_3N_2 materials would benefit from the high absorption and the narrow direct bandgap that are observed experimentally in Zn_3N_2 samples. So far, only simple devices such as TFTs have been demonstrated experimentally.[27,68,73-75] There are several topics that need to be addressed before more complex devices based on Zn_3N_2 can be realised, including the following:

a) Settle the bandgap controversy and identify the reasons behind the discrepancy in the reported bandgaps in Zn_3N_2 samples.
b) Achieve a better understanding of the origin of the high levels of unintentional doping and reduce the carrier density to intrinsic levels.
c) Identify compatible materials systems based on Zn_3N_2 with tuneable optical properties.
d) Investigate suitable p-type dopants for use in p-n junctions based on Zn_3N_2 materials.

The experiments in this work have taken steps towards addressing some of these issues. However, an equally important issue with the realisation of Zn_3N_2-based devices is its poor stability in ambient environments. Previous studies of Zn_3N_2 samples have demonstrated that Zn_3N_2 is prone to oxidation under ambient conditions. Núñez *et al.* reported that an intentionally grown capping layer of 20 nm of ZnO successfully prevented oxidation of the

Zn_3N_2 layer as it limited exposure to O_2 and H_2O.[68] However, further research is required to better understand the oxidation process and improve the stability of Zn_3N_2 in semiconductor devices.

2.7. Summary

The literature surrounding Zn_3N_2 was discussed in this chapter. Some trends and key topics were identified from previous studies which have guided the experiments and discussion in the rest of this work. The known properties of Zn_3N_2 are discussed with a focus on its crystal structure, and optical and electrical properties. This highlighted some key aspects of the research on Zn_3N_2. First, Zn_3N_2 samples have high levels of unintentional doping, which are attributed to structural defects and oxygen impurities. However, at degenerate levels of n-type doping Zn_3N_2 films exhibit relatively high carrier mobility which has been attributed to a low electron effective mass. This suggests that Zn_3N_2 may be a high mobility semiconductor as material quality improves and the doping level is lowered. Furthermore, a controversy surrounding the bandgap of Zn_3N_2 is present in experimental reports. The exact bandgap of Zn_3N_2 is still a topic of debate. However, a significant portion of the Zn_3N_2 samples in literature have an absorption onset in the range of 1.0-1.5 eV. As a result, the optical properties of Zn_3N_2 have placed it as a candidate for use as an earth-abundant solar absorber.

2.8. Bibliography

1. D. E. Partin, D. J. Williams, and M. O'Keeffe, Journal of Solid State Chemistry **132,** 56 (1997).
2. R. Long, Y. Dai, L. Yu, B. Huang, and S. Han, Thin Solid Films **516,** 1297 (2008).
3. N. Jiang, J. L. Roehl, S. V. Khare, D. G. Georgiev, and A. H. Jayatissa, Thin Solid Films **564,** 331 (2014).
4. S. Yoo, A. Walsh, D. O. Scanlon, and A. Soon, RSC Advances **4,** 3306 (2014).
5. X. Cao, A. Sato, Y. Ninomiya, and N. Yamada, The Journal of Physical Chemistry C **119,** 5327 (2015).
6. T. Oshima and S. Fujita, Japanese Journal of Applied Physics **45,** 8653 (2006).
7. W. Peng, T. Tiedje, H. Alimohammadi, V. Bahrami-Yekta, M. Masnadi-Shirazi, and W. Cong, Semiconductor Science and Technology **31,** 10LT01 (2016).
8. X. Cao, Y. Yamaguchi, Y. Ninomiya, and N. Yamada, Journal of Applied Physics **119,** 025104 (2016).
9. R. Wyckoff, *Crystal Structures (Hexagonal closest packed, hcp, structure)*, Vol. I (Interscience Publishers, New York, New York, 1963).
10. H. Sowa and H. Ahsbahs, Journal of Applied Crystallography **39,** 169 (2006).
11. W. Nakwaski, Physica B: Condensed Matter **210,** 1 (1995).

[12] T. Suda and K. Kakishita, Journal of Applied Physics **99,** 076101 (2006).
[13] Y. Naoomi, W. Kouki, Y. Takahiro, S. Atsushi, and N. Yoshihiko, Japanese Journal of Applied Physics **53,** 05FX01 (2014).
[14] D. M. Szmyd, P. Porro, A. Majerfeld, and S. Lagomarsino, Journal of Applied Physics **68,** 2367 (1990).
[15] C. G. Núñez, J. L. Pau, M. J. Hernández, M. Cervera, E. Ruiz, and J. Piqueras, Thin Solid Films **520,** 1924 (2012).
[16] F. J. Zong, H. L. Ma, C. S. Xue, H. Z. Zhuang, X. J. Zhang, H. D. Xiao, J. Ma, and F. Ji, Solid State Communications **132,** 521 (2004).
[17] K. Toyoura, H. Tsujimura, T. Goto, K. Hachiya, R. Hagiwara, and Y. Ito, Thin Solid Films **492,** 88 (2005).
[18] N. Jiang, D. G. Georgiev, T. Wen, and A. H. Jayatissa, Thin Solid Films **520,** 1698 (2012).
[19] K. G. Saw, N. M. Aznan, F. K. Yam, S. S. Ng, and S. Y. Pung, PLOS ONE **10,** e0141180 (2015).
[20] P. K. Chakraborty, G. C. Datta, and K. P. Ghatak, Physica B: Condensed Matter **339,** 198 (2003).
[21] Y. Kumagai, K. Harada, H. Akamatsu, K. Matsuzaki, and F. Oba, Physical Review Applied **8,** 014015 (2017).
[22] M. Ullah, G. Murtaza, M. Yaseen, and S. A. Khan, Journal of Alloys and Compounds (2017).
[23] C. G. Núñez, J. L. Pau, M. J. Hernández, M. Cervera, and J. Piqueras, Applied Physics Letters **99,** 232112 (2011).
[24] N. Jiang, D. G. Georgiev, A. H. Jayatissa, R. W. Collins, J. Chen, and E. McCullen, Journal of Physics D: Applied Physics **45,** 135101 (2012).
[25] R. Ayouchi, C. Casteleiro, L. Santos, and R. Schwarz, physica status solidi (c) **7,** 2294 (2010).
[26] M. Futsuhara, K. Yoshioka, and O. Takai, Thin Solid Films **322,** 274 (1998).
[27] E. Aperathitis, V. Kambilafka, and M. Modreanu, Thin Solid Films **518,** 1036 (2009).
[28] K. Kuriyama, Y. Takahashi, and F. Sunohara, Physical Review B **48,** 2781 (1993).
[29] C. G. Núñez, J. L. Pau, M. J. Hernández, M. Cervera, E. Ruíz, and J. Piqueras, Thin Solid Films **522,** 208 (2012).
[30] G. Cody, *Hydrogenated amorphous silicon, Part B, Optical properties, semiconductors and semimetals* (Orlando: Academic Press Vol, 1984).
[31] F. Zong, H. Ma, J. Ma, C. Xue, X. Zhang, H. Xiao, F. Ji, and H. Zhuang, Materials Letters **59,** 2643 (2005).
[32] W. S. Khan and C. Cao, Journal of Crystal Growth **312,** 1838 (2010).
[33] C. L. Bloxam, J. M. Thomson, and A. G. Bloxam, *Chemistry Inorganic and Organic with experiments*, 9th ed. (P. Blakiston's Son & Co., Philadelphia, 1903).
[34] W. J. Savoye and A. R. Edwards, *Zinc Nitride, Its formation, properties and alloys* (Armour Institute of Technology, 1921).
[35] G. Paniconi, Z. Stoeva, R. I. Smith, P. C. Dippo, B. L. Gallagher, and D. H. Gregory, Journal of Solid State Chemistry **181,** 158 (2008).
[36] F. Zong, H. Ma, C. Xue, H. Zhuang, X. Zhang, J. Ma, F. Ji, and H. Xiao, Science in China Series G: Physics Mechanics and Astronomy **48,** 201 (2005).
[37] F. Zong, H. Ma, C. Xue, W. Du, X. Zhang, H. Xiao, J. Ma, and F. Ji, Materials Letters **60,** 905 (2006).

[38] W. S. Khan, C. Cao, D. Y. Ping, G. Nabi, S. Hussain, F. K. Butt, and T. Cao, Materials Letters **65,** 1264 (2011).
[39] W. S. Khan, C. Cao, F. K. Butt, Z. Ali, M. Safdar, L. Pan, M. Y. Rafique, Q. u. Ain, Z. Usman, and G. Nabi, Applied Surface Science **257,** 7314 (2011).
[40] W. S. Khan, C. Cao, Z. Ali, F. K. Butt, N. Ahmad Niaz, A. Baig, R. ud Din, M. H. Farooq, F. Wang, and Q. ul Ain, Materials Letters **65,** 2127 (2011).
[41] P. C. Wei, S. C. Tong, C. M. Tseng, C. C. Chang, C. H. Hsu, and J. L. Shen, Journal of Applied Physics **116** (2014).
[42] M. Futsuhara, K. Yoshioka, and O. Takai, Thin Solid Films **317,** 322 (1998).
[43] V. Tiron and L. Sirghi, Surface and Coatings Technology **282,** 103 (2015).
[44] P. N. Taylor, M. A. Schreuder, T. M. Smeeton, A. J. D. Grundy, J. A. R. Dimmock, S. E. Hooper, J. Heffernan, and M. Kauer, Journal of Materials Chemistry C **2,** 4379 (2014).
[45] S. Sinha and S. K. Sarkar, RSC Advances **4,** 47177 (2014).
[46] D. Wang, Y. C. Liu, R. Mu, J. Y. Zhang, Y. M. Lu, D. Z. Shen, and X. W. Fan, Journal of Physics: Condensed Matter **16,** 4635 (2004).
[47] E. Maile and R. A. Fischer, Chemical Vapor Deposition **11,** 409 (2005).
[48] F. Zong, H. Ma, W. Du, J. Ma, X. Zhang, H. Xiao, F. Ji, and C. Xue, Applied Surface Science **252,** 7983 (2006).
[49] G. Z. Xing, D. D. Wang, B. Yao, L. F. N. A. Qune, T. Yang, Q. He, J. H. Yang, and L. L. Yang, Journal of Applied Physics **108,** 083710 (2010).
[50] A. H. Jayatissa, T. Wen, and M. Gautam, Journal of Physics D: Applied Physics **45,** 045402 (2012).
[51] J. M. Khoshman, N. Peica, C. Thomsen, J. Maultzsch, B. Bastek, C. Wan, and M. E. Kordesch, Thin Solid Films **520,** 7230 (2012).
[52] T. Wen, M. Gautam, A. M. Soleimanpour, and A. H. Jayatissa, Materials Science in Semiconductor Processing **16,** 318 (2013).
[53] Y. Cordier, B. Damilano, P. Aing, C. Chaix, F. Linez, F. Tuomisto, P. Vennéguès, E. Frayssinet, D. Lefebvre, M. Portail, and M. Nemoz, Journal of Crystal Growth **433,** 165 (2016).
[54] R. Calarco and M. Marso, Applied Physics A **87,** 499 (2007).
[55] N. Chand, Journal of Crystal Growth **97,** 415 (1989).
[56] M. Coke, Thesis, UCL (University College London), 2017.
[57] V. Méndez-García, M. López-López, and I. Hernández-Calderón, Superficies y vacío **8** (1999).
[58] N. Feldberg, J. D. Aldous, P. A. Stampe, R. J. Kennedy, T. D. Veal, and S. M. Durbin, Journal of Electronic Materials **43,** 884 (2014).
[59] N. Feldberg, B. Keen, J. Aldous, D. O. Scanlon, P. A. Stampe, and R. J. Kennedy, in *IEEE Photovoltaic Specialists Conference (PVSC)* (2012), p. 002524.
[60] N. Feldberg, J. D. Aldous, W. M. Linhart, L. J. Phillips, K. Durose, P. A. Stampe, R. J. Kennedy, D. O. Scanlon, G. Vardar, R. L. Field, T. Y. Jen, R. S. Goldman, T. D. Veal, and S. M. Durbin, Applied Physics Letters **103,** 042109 (2013).
[61] C. Wang, Z. Ji, K. Liu, Y. Xiang, and Z. Ye, Journal of Crystal Growth **259,** 279 (2003).
[62] C. W. Zou, R. Q. Chen, and W. Gao, Solid State Communications **149,** 2085 (2009).
[63] E. Kaminska, A. Piotrowska, J. Kossut, A. Barcz, R. Butkute, W. Dobrowolski, E. Dynowska, R. Jakiela, E. Przezdziecka, R. Lukasiewicz, M. Aleszkiewicz, P. Wojnar, and E. Kowalczyk, Solid State Communications **135,** 11 (2005).

[64] V. Kambilafka, P. Voulgaropoulou, S. Dounis, E. Iliopoulos, M. Androulidaki, K. Tsagaraki, V. Šály, M. Ružinský, P. Prokein, and E. Aperathitis, Thin Solid Films **515,** 8573 (2007).
[65] V. Kambilafka, A. Kostopoulos, M. Androulidaki, K. Tsagaraki, M. Modreanu, and E. Aperathitis, Thin Solid Films **520,** 1202 (2011).
[66] T. Yang, Z. Zhang, Y. Li, M. Lv, S. Song, Z. Wu, J. Yan, and S. Han, Applied Surface Science **255,** 3544 (2009).
[67] C. G. Núñez, J. Jiménez-Trillo, M. G. Vélez, J. Piqueras, J. L. Pau, C. Coya, and A. L. Álvarez, Applied Surface Science **285, Part B,** 783 (2013).
[68] C. G. Núñez, J. L. Pau, E. Ruiz, and J. Piqueras, Applied Physics Letters **101,** 253501 (2012).
[69] A. H. Jayatissa and T. Wen, Surface and Coatings Technology **211,** 163 (2012).
[70] Z. Wang, Y. Yue, and Y. Cao, Vacuum **101,** 313 (2014).
[71] S. Simi, I. Navas, R. Vinodkumar, S. R. Chalana, M. Gangrade, V. Ganesan, and V. P. M. Pillai, Applied Surface Science **257,** 9269 (2011).
[72] L. Chun-Ting, C. Hung-Yu, L. Yu-Yan, H. Yi-June, T. Yu-Lin, R. Vittal, S. Yu-Jane, and H. Kuo-Chuan, ACS Applied Materials & Interfaces **7,** 28254 (2015).
[73] S. R. Bhattacharyya, R. Ayouchi, M. Pinnisch, and R. Schwarz, physica status solidi (c) **9,** 469 (2012).
[74] S. Sinha, D. Choudhury, G. Rajaraman, and S. K. Sarkar, RSC Advances **5,** 22712 (2015).
[75] M. A. Dominguez, J. L. Pau, M. Gómez-Castaño, J. A. Luna-Lopez, and P. Rosales, Thin Solid Films **619,** 261 (2016).

Chapter 3: Experimental Techniques and Methodologies

3.1. Physical vapour deposition techniques

3.1.1. Sputter deposition

Sputtering is a physical vapour deposition technique commonly used to deposit thin films and coatings. A widespread commercial application of sputtering techniques has been in the production of data storage disks for computer systems.[1] Because of its principle of operation, sputtering can be a scalable, low-cost, and commercially viable technique compared to its alternatives. A diagram of a sputtering process is shown in **Figure 3.1a**. In a sputtering process, a vapour of atoms is ejected from a target material by plasma-induced ion bombardment. To generate plasma, a current is applied to the target in the presence of a chemically inert sputter gas, such as argon, under high vacuum conditions. The generated electric field ionises the gas, generating a plasma. To increase the sputter yield, a series of magnets are usually placed behind the target. The magnetic field generated by the magnets accelerates ions towards the surface of the target, making the sputter process more efficient. Because of the magnetic field lines of the magnets, the sputter process forms a circular pattern on the target, called the “racetrack”, from which most of the material is sputtered.[2] A photograph of a sputtering process in nitrogen plasma is shown in **Figure 3.1b**.

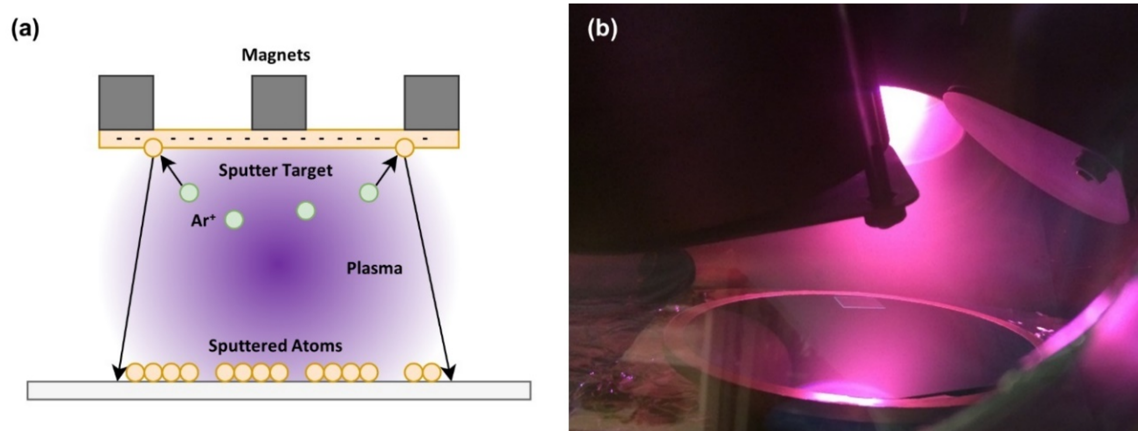

Figure 3.1: (a) Diagram of a sputtering process. (b) A sputter process in nitrogen plasma. In this chamber, the sputter guns are placed at an angle to allow multiple sputter guns to be fitted around the substrate stage.

One of the benefits of sputter deposition is that it can be applied to different materials irrespective of their melting point and rates of thermal evaporation. The deposition of materials that are otherwise difficult to evaporate, e.g. heavy metals such as

tungsten or molybdenum, can be enabled or become more cost-effective through sputtering.[3] The electrical conductivity of the target material is more relevant to the sputtering process, rather than its rate of thermal evaporation. Poor electrical conductivity can lead to a charge build-up on the surface of the target, which is detrimental to the stability of the process and can lead to arcing.[2] As a result, metals and metal alloys are typically easy to sputter because of their high electrical conductivity. Charge build-up issues in non-conductive materials can be avoided by use of a radio-frequency (RF) power supply instead of a DC power supply. By using RF technologies, thin films of semiconductor or even insulating targets can be deposited by sputtering.[4]

To deposit compound films from a metal target, a variation of the sputtering process is commonly used, called reactive sputtering. In reactive sputtering, a reactive gas (e.g. O_2, N_2) is mixed into the sputtering gas. A mixture of the reactive gas with Ar, or a gas phase of the reactive gas exclusively may be used as the process gas. Sputtering in such an environment will result in the formation and deposition of a compound material at the substrate, allowing for a wide variety of compounds to be deposited. The compound material also forms on the surface of the target, an effect known as target poisoning.[5] Depending on the sputtering conditions, the racetrack of the target may become fully poisoned. Because the compound material is often less conductive and has a lower sputter yield than the metal target, conditions of significant target poisoning are associated with charge build-up, arcing, and low deposition rates.[2,5] The deposition rate drops sharply at a certain reactive gas flow rate, at which point the racetrack becomes fully poisoned with the compound material.[5] The reactive sputtering process is characterised by a hysteresis effect, in which the previous state is achieved by decreasing the reactive gas to a lower flow rate than the original decrease. Limiting the effects of the racetrack poisoning is an important aspect to maintaining good control and reproducibility of the reactive sputtering process. This is achieved by controlling the reactive gas flow rate to obtain a stable process.

The reactively sputtered Zn_3N_2 films in this study were deposited in a Denton Vacuum Explorer sputtering system. The base pressure of the deposition chamber was 8×10^{-7} mbar. Zn was sputtered from a 3" Zn target (99.999%) that was supplied by Kurt J. Lesker and was installed on one of the magnetron guns in the vacuum chamber. A DC power supply was used to apply a constant current to the metal target. Gas was supplied in the chamber through a mass flow controller with a maximum flow of 100 sccm (standard cubic centimetres per minute). At regular process conditions, the pressure in the deposition

chamber was in the range of 10^{-3}-10^{-2} mbar. The gas supply could be switched between argon or nitrogen. The gas line was purged at a flow of 100 sccm for 5 minutes before the start of each experiment. An argon sputtering process was used to condition the target (15 minutes prior to deposition) and remove any surface contaminants. The Zn_3N_2 films were deposited by switching the gas supply to nitrogen. A 10-minute pre-sputter process in nitrogen was applied to ensure stable sputtering conditions before opening the main shutter. Zn_3N_2 thin films were deposited on borosilicate glass substrates. The substrate temperature for different samples was unheated or controlled up to 150 °C, measured with a thermocouple. Results from these experiments are presented in Chapter 4.

Sputtering from a multicomponent target

Sputtering from multi-component targets is a common technique to deposit alloy films. The two metals in a two-element sputter target usually exhibit different sputter yields.[6] Therefore, the surface of the target has regions where the ratio of the two elements is different from the bulk of the target. In reactive sputtering, the metal compounds also form at the surface of the target. Because the metal compounds are also likely to have different sputter yields, their formation at the surface of the target affects the overall removal rate of the two metals from the target.

In this study, the formation of an AlZnN alloy is investigated. To deposit AlZnN alloys a reactive sputtering process was developed using a 3" $Zn_{0.8}Al_{0.2}$ sputter target supplied by Pi-KEM. AlZnN films were deposited on unheated glass substrates by DC sputtering in N_2 plasma. A current of 400 mA was applied to the target resulting in powers of 100-120 W. For all samples, a 15-minute pre-sputter process was run to achieve a stable voltage before opening the shutter.

3.1.2. Nanoparticle deposition by gas-phase aggregation

The gas-phase aggregation of nanoparticles is a process by which clusters of atoms, or nanoparticles, are generated by gas-phase condensation of an atomic vapour.[7] The atomic vapour is typically generated using a DC or RF magnetron sputter gun which operates as described in the previous section. The use of sputtering as an underlying mechanism for the generation of the atomic vapour enables a flexible and scalable technique for the formation of nanoparticles. Research interest in the development of scalable processes for nanoparticle generation stems from the various properties that

nanomaterials exhibit, such as improved catalytic or optical activity[8,9], and mechanical or magnetic properties that are not evident in bulk materials.[10-12] Gas-phase aggregation technologies have had significant developments in recent years, enabling processes that can generate well-designed core-shell nanoparticle heterostructures for advanced applications.[12-15]

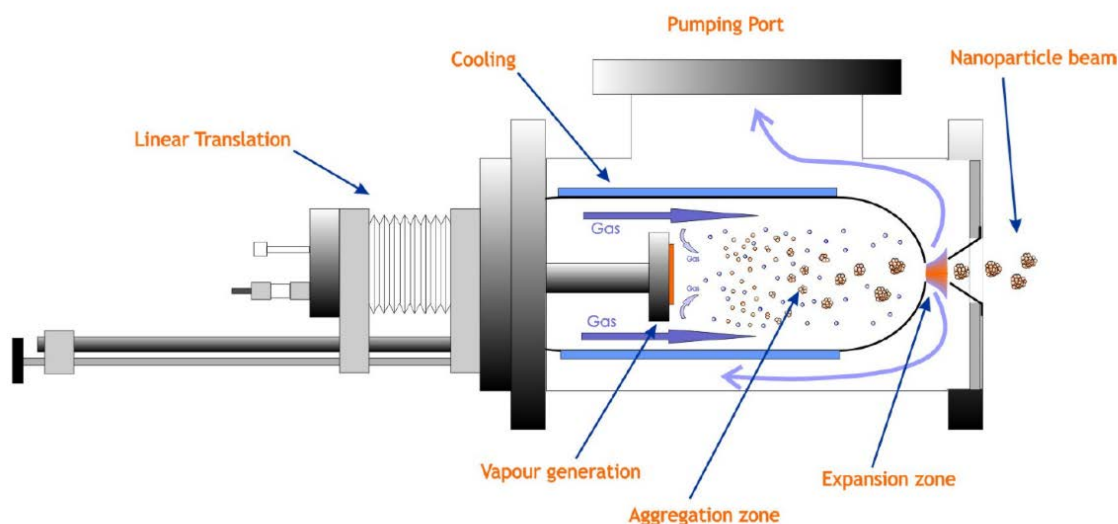

Figure 3.2: Schematic of a gas-phase aggregation nanoparticle deposition source (taken from the NanoGen50 manual provided by Mantis Deposition Ltd).

A diagram of a gas-phase aggregation nanoparticle source is shown in **Figure 3.2**. The first stage of the aggregation process involves collisions between sputtered atoms which lead to the formation of nuclei seeds for the formation of clusters.[7] This stage is made possible after the thermalisation of hot sputtered atoms by argon or other mixed gases. Nanoclusters grow by subsequent collisions of these seeds with other sputtered atoms.[13] The coalescence process takes place in the area in front of the sputter source, which is called the aggregation zone. The aggregation zone has an aperture at one end through which nanoparticles may escape into a high vacuum chamber. Helium or other gases may be mixed in with argon to decrease the residence time of the nanoparticles in the aggregation chamber, allowing for control of the average nanoparticle size. High pressure is generated in the aggregation zone (typically 10^{-2}-10^{-1} mbar) because of its geometry and the gas flow required to operate the sputter source. The aggregation zone is differentially pumped, resulting in a pressure difference of 1-2 orders of magnitude between the aggregation zone and the main vacuum chamber. This results in a beam of nanoparticles being pumped into the main chamber because of the pressure differential.

To enable size selectivity of the generated nanoparticles, a quadrupole mass spectrometer (QMS) can be placed at the exit aperture of the aggregation zone. The QMS separates charged nanoparticles by their mass-to-charge ratio and can be set so that nanoparticles of a certain size maintain their trajectory. This is achieved by applying an alternating current which generates an electric field between four cylindrical rods.[7] Additional sputter sources may be used in parallel (co-sputtering), allowing the deposition of an array of core-shell heterostructures.

To synthesise Zn_3N_2 nanoparticles by gas-phase aggregation, a process for Zn nanoparticle deposition was developed using a commercial NanoGen50 source supplied by Mantis Deposition Ltd. The NanoGen source was installed on a physical vapour deposition system manufactured by Mantis Deposition Ltd with a separate entry lock. The base pressure in the main chamber was 2×10^{-8} mbar. A 2" Zn sputter target (99.995%) supplied by Testbourne Ltd. was installed on the NanoGen source. A current of 150-225 mA was applied to generate plasma in argon gas. The resulting power applied to the target was in the range of 50-75 W. The argon gas flow was set to 100 sccm which generated a pressure of 10^{-3} mbar in the main chamber. Prior to deposition, the argon line was purged for 30 minutes at 100 sccm and the Zn target was conditioned in argon plasma at 175 mA for 10 minutes. The target could be inserted into the aggregation zone by up to 100 mm, effectively reducing the length of the aggregation zone. An RF Plasma source was operated with nitrogen gas to provide the source of active nitrogen species, the operation of which is detailed in Chapter 5. Deposition of Zn and Zn_3N_2 nanoparticles was carried out on unheated glass and silicon (100) substrates for up to 3 h. Results from these experiments are presented in Chapter 8.

3.1.3. Molecular beam epitaxy

Molecular beam epitaxy (MBE) is a physical vapour deposition technique used in the epitaxial growth of high-quality samples with a single crystal structure. The main principle of MBE is based on the generation of a molecular beam from an evaporated or sublimated material (e.g. a metal). To generate a molecular beam from a metal (e.g. in the form of pellets or ingots), it is heated to high temperatures in an effusion cell under ultra-high vacuum conditions. The flux Φ_e of species effusing in vacuum from an evaporated liquid or solid is calculated by Knudsen's and Langmuir's theories as:

$$\Phi_e = A_e p(T) \left(\frac{N_A}{2\pi M k_B T}\right)^{1/2} \tag{3.1}$$

where N_A is Avogadro's number, k_B is Boltzmann's constant, M is the molecular weight of the evaporated species, T is the absolute temperature, and $p(T)$ is the equilibrium pressure of the evaporated species as a function of temperature.[16,17]

Because of the high-vacuum conditions, evaporated molecules have a very large mean free path and can travel very large distances before colliding with other species.[17] For instance, the mean free path for collisions between atoms at operating pressures of 10^{-6}-10^{-4} Torr is in the range of 5-0.05 m, as calculated using the kinetic theory of gases.[18] As a result, the generated beam is well-collimated, in contrast to the atomic vapour which is generated by sputtering, or the vapour generated in Metal Organic Vapour Epitaxy (MOVPE), in which the mean free path is in the order of μm. By varying the growth conditions, MBE is used to grow a variety of different material structures such as epitaxial layers (e.g. thin films and quantum wells), nanowires, and quantum dots.[17,19]

One of the reasons for which a high-purity environment (i.e. high-vacuum) is beneficial in MBE growth is to minimise impurities incorporated into the grown materials. To maintain a high-purity environment over time, modern MBE systems have separate chambers for loading and unloading samples and for growing the materials. The former is usually referred to as the load-lock or entry-lock, and the latter is referred to as the growth chamber.

The growth of high-quality epitaxial layers usually requires high substrate temperatures, which are in the range of 400-800 °C for III-V semiconductors.[20-22] On a hot surface, the adsorbed atoms (adatoms) have increased surface mobility and can diffuse and crystallise in optimal structures, minimising structural defects. As a result, higher material quality is typically obtained at higher temperatures. Group III-V semiconductors are commonly grown with MBE using elements such as Al, Ga, In, As, Sb, and Bi.[17] For the growth of nitride semiconductors (e.g. GaN, InN, Zn_3N_2), active nitrogen species must be introduced into the vacuum chamber. There are two common approaches to achieve that: plasma-assisted MBE (PAMBE), and ammonia MBE (NH_3-MBE).[21,23-25] In the case of plasma-assisted nitride growth, a high purity N_2 gas supply is ionised to generate atomic nitrogen species in the form of an RF plasma. The generation of atomic nitrogen is necessary because molecular nitrogen is chemically inert. In contrast, the generation of

plasma is not necessary in NH_3-MBE. The use of NH_3 as a source of nitrogen is known to allow for higher growth temperatures, which are closer to the conditions used in MOVPE.[25]

The MBE experiments in this study were carried out in an MBE system manufactured by Mantis Deposition Ltd. The system consists of an entry lock and a main chamber. The base pressure in the main chamber was 2×10^{-8} mbar. Several sources were installed on the main chamber, including an effusion evaporator cell for Zn. Zn pellets (99.995%) were supplied by Testbourne Ltd. and loaded into the cell. The cell was heated at 250-320 °C to generate a measurable Zn flux. The arrival rate of Zn was measured with a quartz crystal monitor (QCM) positioned in front of the main shutter. The Zn cell had a relatively long flux transient, so the cell shutter was kept open for at least 20 minutes to allow the Zn flux to settle before opening the main shutter. An RF Plasma source was operated with nitrogen gas to provide the source of active nitrogen species. Zn_3N_2 was deposited on glass, silicon, (100) yttria-stabilised zirconia (YSZ) and a-plane sapphire substrates for up to 2 h. The initial investigation of the growth process was carried out on unheated substrates. The substrate was heated up to 250 °C in subsequent experiments. Results from these experiments are presented in Chapter 5.

3.2. Characterisation techniques

3.2.1. Scanning electron microscopy

Scanning Electron Microscopy (SEM) is used to produce magnified images of the surface of a sample by scanning a region with a high-energy electron beam. When the electron beam reaches a surface (primary electrons), a portion of it is scattered elastically at the surface (back-scattered electrons). At that point, excitation of the sample atoms by the primary electrons results in the generation of secondary electrons. The measured signals of secondary and back-scattered electrons are used to generate an image of the scanned surface.[26] Modern SEM instruments can produce images with magnifications up to 300,000 times and a maximum resolution better than 1 nm, which provide information about surface morphology and features.

In addition to back-scattered and secondary electrons, other phenomena are also observed, such as the emission of Auger electrons, characteristic X-rays, and cathodoluminescence. Secondary electrons are emitted from atoms closer to the surface of the sample, whereas characteristic X-rays are generated from a region of the sample into which the primary electrons are scattered (penetration depth). The penetration depth of the

electron beam is typically in the order of a few μm, as shown in **Figure 3.3**, and can be controlled with the accelerating voltage. A larger accelerating voltage results in a larger penetration depth. SEM instruments are sometimes equipped with an X-ray detector that can detect the characteristic X-rays emitted by the atoms in the sample.[27] The emitted X-rays are characteristic of the atomic structure from which they originate because they are the result of atomic transitions. As a result, the X-ray spectra can be used to perform compositional analysis of a sample with a technique called Energy Dispersive X-ray Spectroscopy (EDS or EDX). EDS is a non-destructive technique and can be both qualitative and quantitative. EDS can yield very accurate results with the use of high-quality standard samples. However, if the use of high-quality standards is omitted in the quantitative analysis of results it is also prone to large systematic errors.[27] As a result, some caution is required when interpreting the EDS spectra quantitatively.

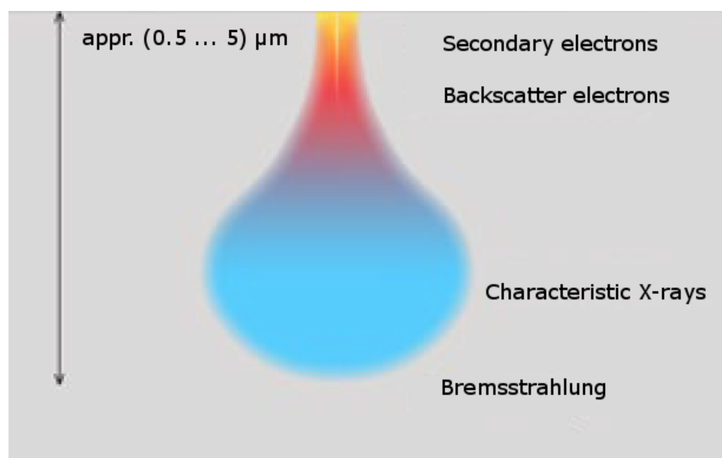

Figure 3.3: Representation of the analysis volume of a material exposed to a high-energy electron beam, from Bruker's "*Introduction to EDS analysis*" reference manual.

Throughout this study, SEM images of thin films were recorded on a Raith Field Emission Scanning Electron Microscope (FESEM) with accelerating voltages of 2-10 kV. The accelerating voltage was selected based on the conductivity of the surface and the thickness of the films, to avoid charge build-up issues and achieve good image quality. Cross-sectional images were recorded in some occasions to measure the thickness of the films. EDS spectra were acquired on a Bruker Quantax EDS system installed on the Raith FESEM. To eliminate the effects of the substrate to the measured EDS spectrum, the accelerating voltage was selected so that the penetration depth of the electron beam did not exceed the thickness of the sample. This is demonstrated in **Figure 3.4**, which shows measured EDS spectra at different accelerating voltages. Peaks attributed to the substrate, in this case Al K from a sapphire substrate (Al_2O_3), are observed at high accelerating

voltages in which the penetration depth of the electron beam is greater than the film thickness. The composition of some of the samples deposited in this study was evaluated by quantification of the EDS spectra using a standardless analysis (P/B-ZAF). The P/B-ZAF analysis utilises the measured background (bremsstrahlung) to calibrate the intensity of the particular characteristic X-rays (so-called *P/B* ratios). The *P/B* ratios are used to calculate necessary corrections to atomic number effects (*Z*), absorption (*A*), and fluorescence (*F*) without the use of standards (*ZAF* corrections).

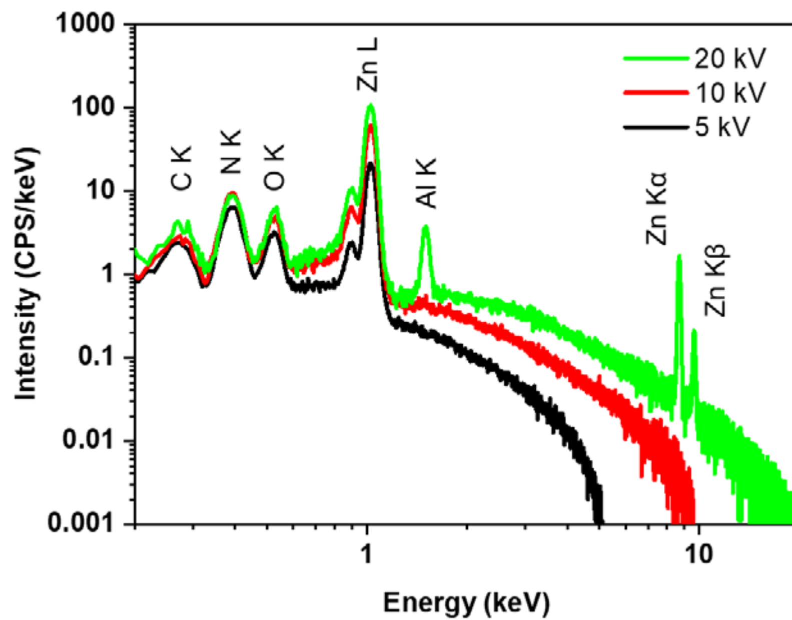

Figure 3.4: Measured EDS spectra of a thin film at different accelerating voltages. An Al peak from the Al_2O_3 substrate emerges at high accelerating voltages because of the increased penetration depth of the electron beam.

3.2.2. X-ray diffraction and reflectivity

X-ray Diffraction (XRD) is used to study the crystal structure of materials based on the diffraction of an X-ray beam off an atomic structure. A simple diagram of an X-ray diffractometer is shown in **Figure 3.5a**. Crystal structures display unique diffraction patterns which are caused by the distance between the atomic planes at which the X-rays are diffracted. A visual representation of this process is shown in **Figure 3.5b**.

Bragg's law of diffraction is used to determine the interatomic distances in a crystal structure based on the positions of diffraction peaks, or vice-versa. Bragg's law of diffraction is commonly written in the following form:

$$n\lambda = 2d\,\sin(\theta) \tag{3.2}$$

where *n* is the order of diffraction (positive integer), λ is the wavelength of the X-ray beam, *d* is the spacing between adjacent lattice planes and θ is the Bragg angle of the observed diffraction. The spacing *d* for a specific crystal plane is calculated based on the lattice constant and the Miller indices for that plane. For instance, for a cubic structure the following equation is used:

$$\mathrm{d_{hkl}} = \frac{a}{\sqrt{h^2+k^2+l^2}} \tag{3.3}$$

where α is the lattice parameter of a cubic crystal structure, and *h*, *k* and *l* are the Miller indices of a crystal plane. The width of diffraction peaks in an experimental XRD pattern is affected by a few parameters including defects and strain in the crystal structure, the size of the crystallites, and instrument-induced broadening. Therefore, the diffraction patterns of highly crystalline materials display narrow diffraction peaks, whereas defective materials or polycrystalline structures with very small crystallite size show broader features.

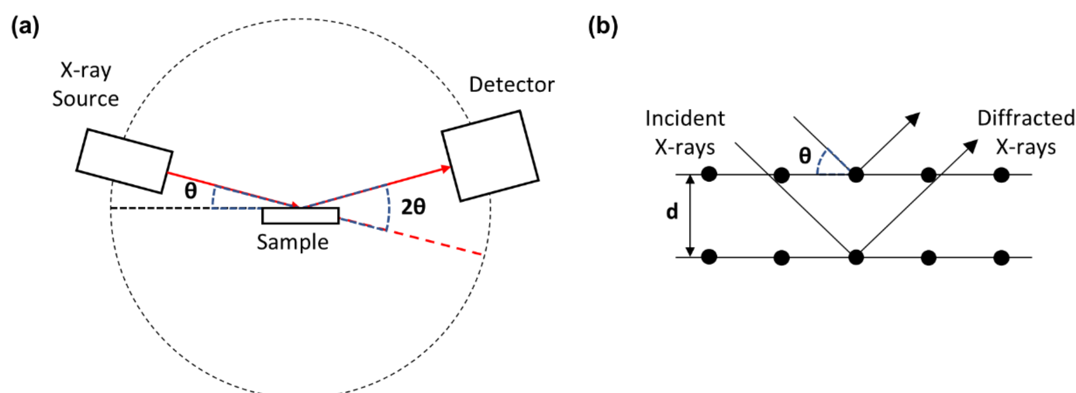

Figure 3.5: (a) Diagram of an X-ray diffractometer showing the *θ-2θ* geometry. (b) Representation of Bragg's law of diffraction.

In a standard out-of-plane XRD measurement (Bragg-Brentano geometry), the X-ray beam and the detector rotate around the sample with a relative angle relationship of *θ-2θ*, as shown in **Figure 3.5a**. An alternative measurement setup is the grazing incidence geometry. In a grazing incidence measurement, the incident beam is fixed at a shallow angle, typically 0.3-3.0°, while the detector scans a range of wider angles. When measuring thin films, the grazing incidence geometry limits the penetration depth of the beam to the sample surface and increases the sample-to-substrate signal ratio. In a standard *θ-2θ* measurement, only planes that satisfy Bragg's condition for diffraction are observed, whereas in a grazing incidence measurement, different crystal orientations which, for instance, may be present in polycrystalline films will also be observed.

In X-ray Reflectivity (XRR), low-angle diffraction of the X-ray beam is measured in the standard out-of-plane geometry. XRR is a surface-sensitive technique that is used to characterize layer structures and interfaces in a sample in terms of their thickness, roughness, and densities. Internal reflections within the thin layers cause a series of oscillations which are observed in XRR measurements. An example XRR measurement of a thin film structure is shown in **Figure 3.6**. These measurements can be analysed or modelled to obtain information about the structure. The angle of maximum reflection in an XRR scan is called the critical angle and it depends on the electron density and density of the sample.

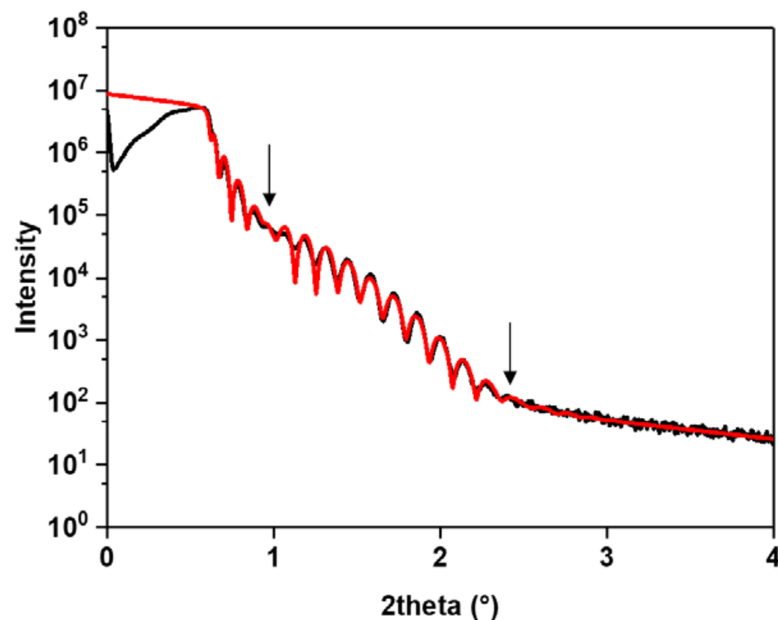

Figure 3.6: Example of an X-ray Reflectivity measurement and model of a thin film with a surface oxide layer. The high-frequency oscillations indicate the presence of a uniform layer. The envelope between the two arrows is caused by a much thinner layer on the surface of the sample.

The XRD patterns examined in this study were measured on a Bruker D8 DISCOVER diffractometer with a LynxEye detector rotated by 90° and set to 1D mode. This detector mode was selected to optimise the measured signal in polycrystalline samples. Both in-plane and out-of-plane measurements were possible using the same experimental setup. Grazing incidence measurements, where available, were performed at an incidence angle of 1-3°. XRR measurements of some samples were obtained with an out-of-plane scan in the 2θ range of 0-6° with the detector set to 0D mode.

3.2.3. Transmittance and reflectance spectroscopy

Transmittance and reflectance spectroscopy are optical techniques that measure how light interacts with a material. Features observed in the transmittance and reflectance spectra of semiconductor thin films depend on the thickness and the optical properties (refractive index and extinction coefficient) of all components of an optical system (e.g. substrate and thin film layer structure). For example, the reflectance spectrum of a material measured on different substrates may differ because of the different optical properties of each substrate. Experimentally, transmittance and reflectance measurements require the measurement of a baseline, i.e. the spectrum of a light source such as a white light source. The same light source is then measured when transmitted (reflected) off a sample. Transmittance (reflectance) is calculated by dividing the transmitted (reflected) spectrum by the baseline:

$$\mathrm{T} = \frac{Transmitted}{Baseline}, \ \mathrm{R} = \frac{Reflected}{Baseline} \tag{3.4}$$

where T, R are the spectrally dependent transmittance and reflectance respectively. As such transmittance (reflectance) takes values between 1 for a fully transmissive (reflective) medium and 0 for a non-transmissive (non-reflective) medium.

In this study, transmittance and reflectance measurements were recorded on a J. A. Woollam RC2 ellipsometer. Transmittance at normal incidence and reflectance at 15° incidence were measured in the spectral range of 300-1700 nm.

Refractive index and film thickness

In the non-absorbing region of a semiconductor thin film, internal reflections of the incident beam interfere with the reflected or transmitted beam and cause destructive and constructive effects due to the phase difference of the reflected beams. As a result, the measured spectra may have oscillations which are caused by optical interference. The spacing of the observed oscillations depends on the thickness and the refractive index of the film that is causing them.

A diagram of the mechanism of optical interference is shown in **Figure 3.7a**. An example of interference patterns in the reflectance spectrum of a thin film are shown in **Figure 3.7b**. Assuming the refractive index of the thin film n is $n > 1$, the positions of the constructive interferences (maxima) are described by the following equation:[28]

$$2nd\cos(\beta) = \left(m - \frac{1}{2}\right)\lambda_r \tag{3.5}$$

where n and d are the refractive index and thickness of the film respectively, β is the angle of the beam in the film calculated by Snell's law, m is the order of reflection, and λ_r is the wavelength of the maximum reflection. This equation allows the estimation of the refractive index or the thickness of a thin film from experimental optical data in the spectral range in which minima and maxima are observed. The order of reflection m must be known or be determined experimentally. This can be done by measuring a film thin enough to observe the first order of reflection, at which point the interference pattern stops.

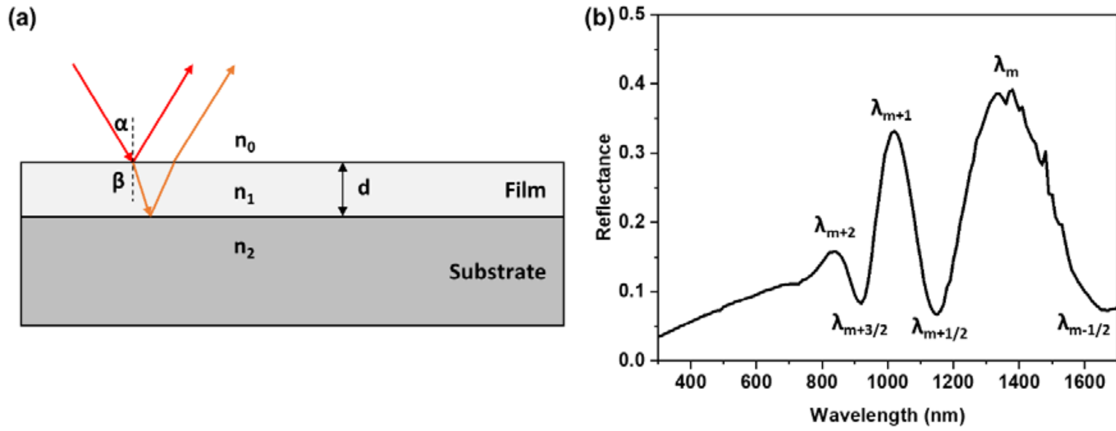

Figure 3.7: (a) Diagram of optical interference effects in an ambient, film, substrate system. (b) Example of an optical interference pattern observed in reflectance spectra of a semiconductor thin film.

Alternatively, the order of reflection can be approximated using the following equation:

$$m = \frac{\lambda_m}{2(\lambda_m - \lambda_{m+\frac{1}{2}})} \tag{3.6}$$

where λ_m and $\lambda_{m+1/2}$ are the spectral positions of two successive extremes, which have an order difference of ½ (e.g. minimum → maximum or vice-versa). This approximation is only valid under the assumptions that the refractive index between the two extremes is approximately constant and that the measurements are taken at normal or close to normal incidence, so that $cos(\beta) \approx 1$. Therefore, this approximation is more accurate in the non-absorbing regions of a semiconductor where the refractive index does not vary strongly with wavelength.

Absorption and extinction coefficient

Transmittance and reflectance measurements can be used to calculate the extinction coefficient and the optical bandgap of a semiconductor. This requires the calculation of the absorption coefficient of the film with the following equation:[29]

$$a = \frac{1}{d} \ln \frac{(1-R)\left(1+\frac{A}{T}\right)+\sqrt{(1-R)^2\left(1+\frac{A}{T}\right)^2+4R}}{2} \tag{3.7}$$

where α, d, and A are the absorption coefficient, thickness, and absorptance of the film respectively. Absorptance is defined as $A = 1 - (R+T)$, which simplifies the equation to:

$$a = \frac{1}{d} \ln \frac{\frac{(1-R)^2}{T}+\sqrt{\frac{(1-R)^2}{T^2}+4R}}{2} \tag{3.8}$$

These equations are derived from Fresnel's equations of reflectance, often using different assumptions about the complex dielectric function of the medium and by substituting the extinction coefficient k with $k = \alpha\lambda/4\pi$. Analysis of the optical bandgap from the absorption coefficient is commonly done with a Tauc plot, which relies on the proportionality of an expression of the absorption coefficient with the photon energy hv in the absorbing region of semiconductors.[30] The relation between the bandgap and the absorption coefficient can be written as follows:

$$ahv \propto \left(E_g - hv\right)^r \tag{3.9}$$

where E_g is the optical bandgap of the material and r a constant in the order of 1, which depends on the dominant transition type in the semiconductor (direct or indirect). The r constant takes values of ½ and 2 for direct and indirect semiconductors respectively.

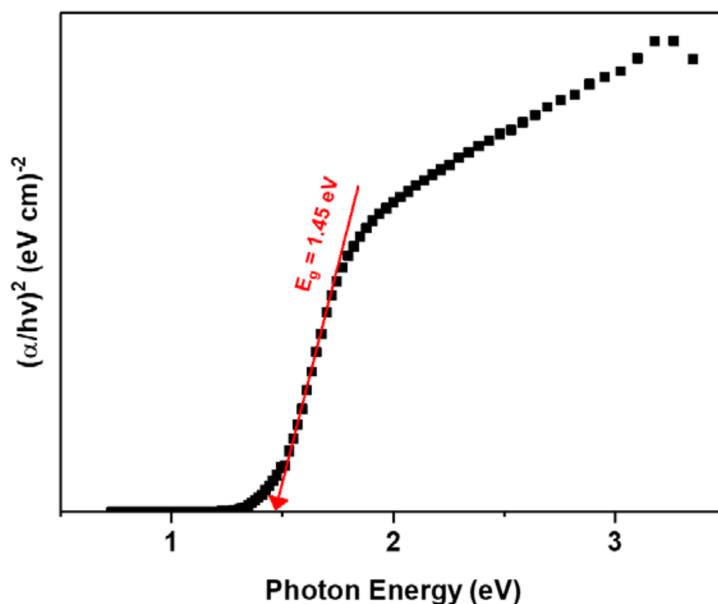

Figure 3.8: Example of an absorption plot used to calculate the optical bandgap of a Zn_3N_2 sample deposited by Molecular Beam Epitaxy. The arrow shows the linear fit to the absorption data which is used to extract the optical bandgap. For this plot, the Cody expression is used with $r = ½$.

Cody *et al.*[31] suggested an alternative expression similar to that derived by the Tauc-Lorentz model:

$$\frac{a}{hv} \propto \left(E_g - hv\right)^r \quad (3.10)$$

In the Cody-Lorentz model, absorption above the bandgap is greater in magnitude and therefore the Cody expression can more accurately describe films with high absorption. Experimentally, the optical bandgap of a material may be estimated from these expressions by plotting a function $F(\alpha)^{1/r}$ against the photon energy and extrapolating the linear region at the cross-section with the energy axis. An example of this absorption plot is shown in **Figure 3.8**. Depending on the shape of the experimental absorption coefficient spectra, its interpretation is often challenging. Therefore, the parameters for a Tauc/Cody absorption plot analysis, e.g. energy region, absorption expression, *r* parameter, must be selected carefully.

3.2.4. Spectroscopic ellipsometry

Spectroscopic Ellipsometry is an optical technique that measures how the state of polarisation of light changes when reflected at the surface of a medium. The polarisation state of a light beam refers to the orientation of the electric field in the propagation direction of the electromagnetic wave.[32] Ordinary light sources are non-polarised because the orientation of the electric field oscillates randomly. An unpolarised beam of light can be polarised using a polariser, which is an optical component that only transmits light of a certain orientation.

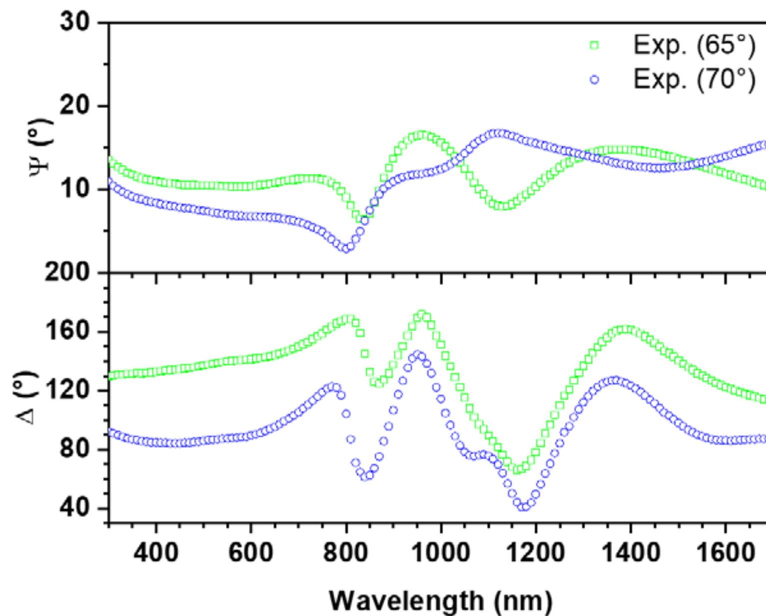

Figure 3.9: Example measurements of the ellipsometric parameters Ψ (top) and Δ (bottom) for a thin semiconductor film grown on a glass substrate. Optical interference extrema which depend on the thickness of the film are observed below the bandgap of the semiconductor.

In ellipsometry, the changes in the state of polarisation of the reflected beam are measured and expressed as Ψ and Δ, which are known as the ellipsometric parameters. An example set of measured ellipsometric parameters is shown in **Figure 3.9**. The ellipsometric parameters are related to the Fresnel reflection coefficients by the following equation:[32]

$$\frac{r_p}{r_s} = \tan(\Psi)\, e^{i\Delta} = \rho \tag{3.11}$$

where r_p and r_s are the Fresnel coefficients for p and s polarized light respectively and ρ is the complex reflection coefficient. For a model of a substrate, a film and ambient, the complex reflection coefficient is a function of the following parameters:

$$\rho = f(n_0, n_1, n_2, \lambda, d, \alpha) \tag{3.12}$$

where n_0, n_1, n_2 are the refractive indices of ambient, the film and the substrate respectively, λ is the wavelength of light, d is the film thickness, and α is the angle of incidence, as shown in **Figure 3.7a**. An optical model can fit the unknown parameters, e.g. n_1, d, to the experimental data to characterize the system. Amongst other parameters such as surface and interfacial roughness, spectroscopic ellipsometry measurements can determine the thickness of a layer, the refractive index, and the extinction coefficient of a material by modelling its dielectric function with a series of oscillators, such as the Tauc-Lorentz and Cody-Lorentz models for semiconductors.

Because ellipsometry measures a phase change (Δ) and a change in the ratio of amplitudes (Ψ) between s and p components of polarized light, it is more sensitive and reproducible than a simple intensity reflectance measurement. The optical interference oscillations that are observed in transmittance and reflectance measurements are also present in measurements of the ellipsometric parameters and are caused by the same effect. The ellipsometric parameters are typically measured in more than one angle of incidence (e.g. 65° and 70°) to increase the degree of confidence for any developed models. While ellipsometry can be very precise, realistic modelling of an optical system can often be challenging due to rough surfaces, anisotropy or other non-ideal features that can be difficult to model. Furthermore, examining the uniqueness of a model is crucial to reliably determine the properties of an optical system.

Spectroscopic Ellipsometry measurements were obtained on a J. A. Woollam RC2 ellipsometer at incidence angles of 65 and 70° in the spectral range of 300-1700 nm. Semiconductor layers were modelled with the WVASE software using an oscillator based

on a Herzinger-Johs parameterised function.[33] Where necessary, roughness was modelled as an intermix of ambient with the film.

3.2.5. Photoluminescence spectroscopy

Photoluminescence spectroscopy is an optical technique which uses a source of excitation to cause transitions in the electronic structure of a material and measure light emitted from the relaxation process of these transitions.[34] The source of the excitation is single wavelength light, typically produced by a laser. In a semiconductor material, electrons in the valence band may be excited to the conduction band if the incident photon energy is greater than the bandgap. This generates what is known as an electron-hole pair, with the electron occupying the conduction band and the hole occupying the valence band. When an electron recombines with a hole, it may do so with a radiative or non-radiative transition.[35] In photoluminescence spectroscopy, the nature of different radiative recombination processes of a semiconductor can be studied and characterised to infer information about the band structure of the material. For instance, band-to-band, band-to-defect (donor or acceptor), donor-acceptor pairs, or excitonic transitions may be observed.[35] This process is shown in **Figure 3.10a** for some of the possible radiative recombination transitions.

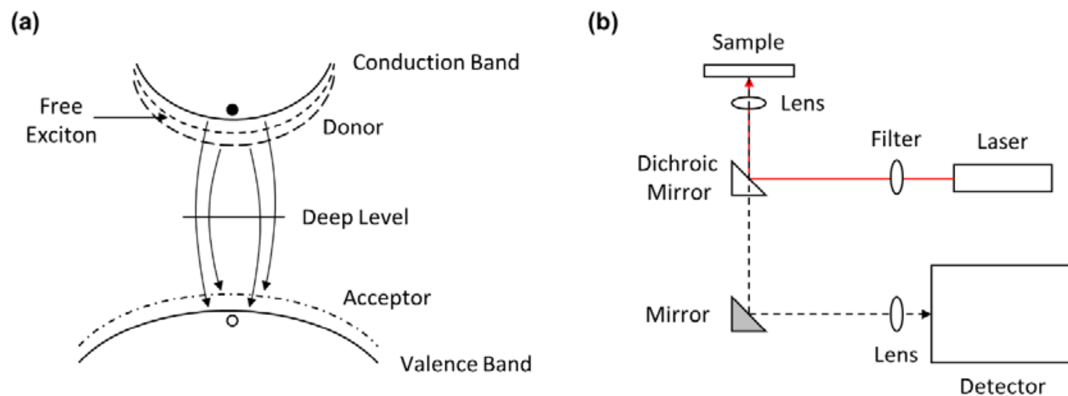

Figure 3.10: (a) Some radiative recombination processes that may be observed in semiconductor materials. (b) Diagram of an experimental photoluminescence setup which uses the same optical path for excitation of the sample and collection of the photoluminescence signal.

A diagram of a typical experimental photoluminescence setup is shown in **Figure 3.10b**. An experimental photoluminescence setup consists of a laser, the sample stage, and a set of mirrors and lenses which collect emitted light and direct it towards a detector or spectrometer. The setup presented in **Figure 3.10b** uses a dichroic mirror, which has the property to reflect specific wavelengths of light while transmitting others. A dichroic mirror

is selected to reflect the excitation beam but transmit the wavelengths of interest for photoluminescence. This optical setup enables the use of the same optical path for the excitation and collection of the emitted light. While this type of optical setup is preferred in modern photoluminescence experiments, other experimental setups are used in which the excitation beam has a non-normal angle of incidence onto the sample.[34] Because the temperature dependence of photoluminescence is often of interest, photoluminescence experiments may be set up around a cryostat with the ability to reach and maintain lower temperatures using liquid nitrogen or helium.

To account for the spectral dependence of optics such as mirrors and lenses, and the grating which are used in the spectrometer of an experimental setup, any measured PL spectra should be corrected. To correct for the spectral dependence of the experimental setup, the spectrum of a well-characterised light source (e.g. a white light source) is measured through the optical path used for the PL measurements. A spectral correction factor is then calculated by using a reference spectrum of the light source, as such:

$$Correction\ Factor\ (\lambda) = \frac{Reference\ Spectrum\ (\lambda)}{Measured\ Spectrum\ \ (\lambda)} \tag{3.13}$$

Correcting the measured spectra is more important than it may seem. For instance, the measured shape of the PL spectrum may change dramatically in wavelength regions where the efficiency of the grating or the detector vary. As a result, the real shape of the PL can only be obtained after correcting for any such effects that are introduced by experimental apparatus.

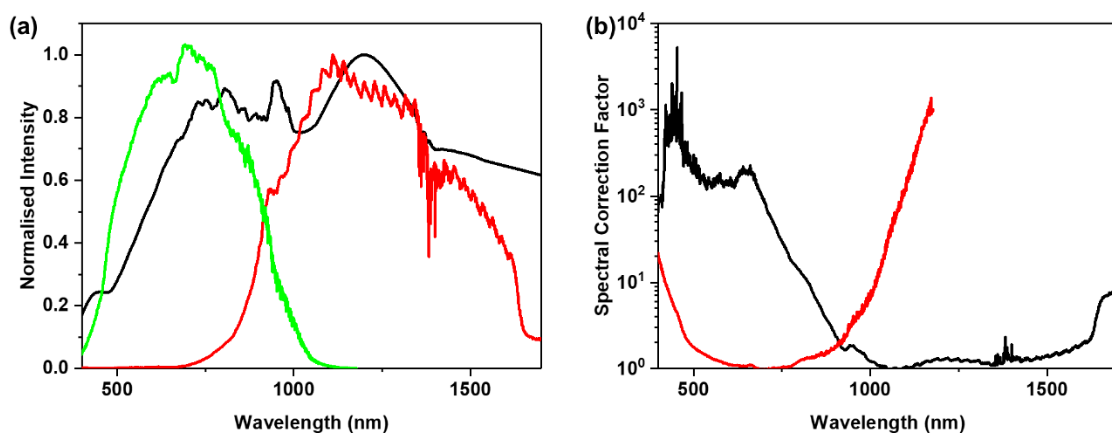

Figure 3.11: (a) Reference spectrum of a white-light source (black) and corresponding measured spectra with InGaAs (red) and Si (green) detectors. (b) Calculated spectral correction factors for InGaAs (black) and Si (red) detectors.

In this study, photoluminescence measurements were performed with the samples mounted on a copper plate inside an Oxford Instruments Optistat Dry cryostat. For low

temperature measurements, the cryostat chamber was pumped down to 10^{-4} mbar and subsequently cooled down to 3.7 K using a closed-cycle He compressor. The samples were excited using a 100 mW 642 nm laser. A variable neutral density filter was used to attenuate the power of the excitation beam. The emitted light was collected from the surface of the sample and focused into an Andor 500i spectrometer which enabled measurements in the spectral range of 600-1600 nm. The measured spectra were corrected for the spectral dependence of the optics and the grating used in the spectrometer using a well-characterised tungsten halogen white light source (SLS201L) manufactured by Thorlabs. Some of the measurements used to calculate the spectral correction factor are shown in **Figure 3.11**, which shows the measured spectra and the calculated correction factors for the two detectors. It is noted that the correction factors in **Figure 3.11b** take larger values in the spectral regions where the detectors have a lower efficiency. In general, care should be taken so that the correction factors are only used within a range that is acceptable for the detector and gratings being used. Outside this range, correction factors may take very high values (e.g. 10-100) and their use does not necessarily produce a properly corrected spectrum.

3.2.6. Hall effect measurements

The Hall effect is a phenomenon in which a voltage difference is produced across a conducting material when a magnetic field is applied perpendicular to the flow of current. Measurements of the Hall effect in semiconductors are used to derive the resistivity, charge carrier concentration and charge carrier mobility, as well as the majority charge carrier (n or p-type conductivity). The van der Pauw method is commonly used to derive these parameters. In the van der Pauw method, a series of resistance measurements are performed by measuring the potential difference across two contacts on the sample when a current is applied at two different contacts on the corners of the sample. The sheet resistance (R_s) is calculated by a numerical method using the following equation:[36,37]

$$e^{-\pi R_V/R_s} + e^{-\pi R_H/R_s} = 1 \tag{3.14}$$

where R_V and R_H are the characteristic vertical and horizontal resistances respectively. R_V and R_H are calculated by the average of 4 resistance measurements at the contacts (2 for the two sides of the sample, doubled for reverse polarities).

The Hall Voltage (V_H) is calculated by measuring the voltage difference across two diagonal contacts, while applying current across the other two contacts under a positive and

negative perpendicular magnetic field. The overall Hall Voltage is calculated as the average difference of 8 measurements. These quantities are then used to calculate a series of electrical properties, using the following equations:

Resistivity: $\rho = R_s d$ (3.15)

Conductivity: $\sigma = \frac{1}{R_s d}$ (3.16)

Hall Coefficient: $R_{Hall} = \frac{V_H d}{IB}$ (3.17)

Sheet and bulk carrier density: $n_s = \frac{IB}{e\,|V_H|}, n = \frac{n_s}{d}$ (3.18)

Carrier mobility: $\mu = \frac{1}{e n_s R_s}$ (3.19)

where d is the thickness of the films, I is the applied current, B is the strength of the magnetic field and e is the electron charge. The sign of R_{Hall} is used to indicate whether holes (p-type conductivity) or electrons (n-type conductivity) are the majority carrier in the conducting material.

The Hall effect measurements in this study were acquired on an Ecopia HMS-5000 Hall Effect system. The strength of the magnetic field was 0.556 T. Metallic contacts were prepared by placing high purity indium at the corners of a square sample and annealing at 320-350 °C for 60 seconds. Alternatively, indium contacts were soldered onto the sample using a soldering iron. In this case, the metallic contacts were annealed locally without heating the rest of the sample to high temperatures.

3.3. Bibliography

1. G. Strasser, Vakuum in Forschung und Praxis **9,** 42 (1997).
2. A. Anders, Thin Solid Films **502,** 22 (2006).
3. W. Eckstein and J. László, Journal of Nuclear Materials **183,** 19 (1991).
4. B. A. Probyn, Vacuum **18,** 253 (1968).
5. S. Berg and T. Nyberg, Thin Solid Films **476,** 215 (2005).
6. M. Moradi, C. Nender, S. Berg, H. O. Blom, A. Belkind, and Z. Orban, Journal of Vacuum Science & Technology A: Vacuum, Surfaces, and Films **9,** 619 (1991).
7. P. Grammatikopoulos, S. Steinhauer, J. Vernieres, V. Singh, and M. Sowwan, Advances in Physics: X **1,** 81 (2016).
8. B. Hvolbæk, T. V. W. Janssens, B. S. Clausen, H. Falsig, C. H. Christensen, and J. K. Nørskov, Nano Today **2,** 14 (2007).
9. S. H. Joo, J. Y. Park, J. R. Renzas, D. R. Butcher, W. Huang, and G. A. Somorjai, Nano Letters **10,** 2709 (2010).
10. M. B. Cortie and A. M. McDonagh, Chemical Reviews **111,** 3713 (2011).

[11] M. Bohra, P. Grammatikopoulos, R. E. Diaz, V. Singh, J. Zhao, J.-F. Bobo, A. Kuronen, F. Djurabekova, K. Nordlund, and M. Sowwan, Chemistry of Materials **27,** 3216 (2015).
[12] I. Khan, K. Saeed, and I. Khan, Arabian Journal of Chemistry (2017).
[13] Y. H. Xu and J. P. Wang, Advanced Materials **20,** 994 (2008).
[14] S. In, A. H. Kean, A. Orlov, M. S. Tikhov, and R. M. Lambert, Energy & Environmental Science **2,** 1277 (2009).
[15] J. Tang, E. Verrelli, and D. Tsoukalas, Microelectronic Engineering **86,** 898 (2009).
[16] A. Y. Cho and J. R. Arthur, Progress in Solid State Chemistry **10,** 157 (1975).
[17] S. Franchi, in *Molecular Beam Epitaxy* (Elsevier, Oxford, 2013), p. 1.
[18] M. A. Herman and H. Sitter, *Molecular beam epitaxy: fundamentals and current status*, Vol. 7 (Springer Science & Business Media, 2012).
[19] A. Colli, F. Martelli, and S. Rubini, in *Molecular Beam Epitaxy* (Elsevier, Oxford, 2013), p. 55.
[20] N. Chand, Journal of Crystal Growth **97,** 415 (1989).
[21] B. M. McSkimming, C. Chaix, and J. S. Speck, Journal of Vacuum Science & Technology A **33,** 05E128 (2015).
[22] Y. Cordier, B. Damilano, P. Aing, C. Chaix, F. Linez, F. Tuomisto, P. Vennéguès, E. Frayssinet, D. Lefebvre, M. Portail, and M. Nemoz, Journal of Crystal Growth **433,** 165 (2016).
[23] A. N. Alexeev, V. P. Chaly, D. M. Krasovitsky, V. V. Mamaev, S. I. Petrov, and V. G. Sidorov, Journal of Physics: Conference Series **541,** 012030 (2014).
[24] J. R. Lang and J. S. Speck, Journal of Crystal Growth **346,** 50 (2012).
[25] M. H. Wong, F. Wu, C. A. Hurni, S. Choi, J. S. Speck, and U. K. Mishra, Applied Physics Letters **100,** 072107 (2012).
[26] W. Zhou, R. Apkarian, Z. L. Wang, and D. Joy, in *Scanning microscopy for nanotechnology* (Springer, 2006), p. 1.
[27] N. W. Ritchie, Scanning **35,** 141 (2013).
[28] J. E. Greivenkamp Jr, in *Handbook of optics* (New York: McGraw-Hill, 1995).
[29] D. Ritter and K. Weiser, Optics Communications **57,** 336 (1986).
[30] J. Tauc, in *Amorphous and Liquid Semiconductors* (Springer, 1974), p. 159.
[31] G. Cody, *Hydrogenated amorphous silicon, Part B, Optical properties, semiconductors and semimetals* (Orlando: Academic Press Vol, 1984).
[32] D. Gonçalves and E. A. Irene, Química Nova **25,** 794 (2002).
[33] B. Johs, C. M. Herzinger, J. H. Dinan, A. Cornfeld, and J. D. Benson, Thin Solid Films **313,** 137 (1998).
[34] I. Pelant and J. Valenta, *Luminescence spectroscopy of semiconductors* (Oxford University Press, 2012).
[35] G. D. Gilliland, Materials Science and Engineering: R: Reports **18,** 99 (1997).
[36] L. J. van der Pauw, in *Semiconductor Devices: Pioneering Papers* (WORLD SCIENTIFIC, 1991), p. 174.
[37] E. H. Putley, Journal of the American Chemical Society **83,** 4303 (1961).

Chapter 4: Zinc Nitride Grown by Sputtering

4.1. Sputtering process

As outlined in Chapter 1, this work is focused on developing Zn_3N_2, which is a relatively little studied material. The first approach followed to develop Zn_3N_2 in this study was with a reactive sputtering process. Zn_3N_2 thin films were deposited under a variety of different growth conditions and characterised in terms of their structural, electrical and optical properties. The properties of the material after full oxidation are also discussed in this chapter. The results presented here serve as a baseline for the discussion in Chapters 5, 6, and 7, which discuss MBE-grown Zn_3N_2 samples, the properties of a ternary AlZnN alloy, and the effect of thermal annealing on Zn_3N_2 respectively.

4.1.1. Deposition rate and ambient stability

The initial characterisation and optimisation of the sputtering process was done on an unheated rotating substrate. The process of optimisation required mapping of the following experimental parameters:

a) the current applied to the Zn target, and
b) the nitrogen gas flow rate.

Film deposition was observed for nitrogen flow rates in the range of 15-45 sccm (standard cubic centimeters per minute). Outside this range, the plasma was either extinguished or the sputter process became unstable and resulted in arcing. A current of 50, 100, and 200 mA was applied to the target, resulting in a sputter power in the range of 20-100 W.

The thickness of the films was determined ex-situ by a combination of cross-sectional SEM, and profilometer and optical measurements. The obtained deposition rate is plotted as a function of sputter power for three different nitrogen flow rates in **Figure 4.1a**. Two trends were identified from these experiments. Firstly, as the power applied to the target increased, the deposition rate also increased. Secondly, increasing the nitrogen flow rate resulted in lower deposition rates. The decreased deposition rate at higher nitrogen flow rates is attributed to an increased formation of Zn_3N_2 at the surface of the target enabled by the surplus of nitrogen. Because Zn_3N_2 is expected to have a lower sputter yield than metallic Zn, this results in a decreased deposition rate. Overall, the deposition rate for

the nitrogen sputtering process ranged between 0.05 and 2.00 μm/h, based on the process conditions.

The as-deposited films had an opaque dark color, shown in **Figure 4.1b**. It was found that when stored in ambient the samples were transformed to a transparent material. The change in opacity was a gradual process which lasted for a period of several days to several weeks, depending on the thickness of the films. This behaviour has been observed in literature and is attributed to oxidation of Zn_3N_2 films.[1-3] Further investigation revealed this to be the case with our samples. The contrast between as-deposited and fully oxidised samples is shown in **Figure 4.1b**. With this effect in mind, all characterisation was done as soon as possible after exposing the samples to ambient, to minimise the effect of the oxidation process on the measured properties.

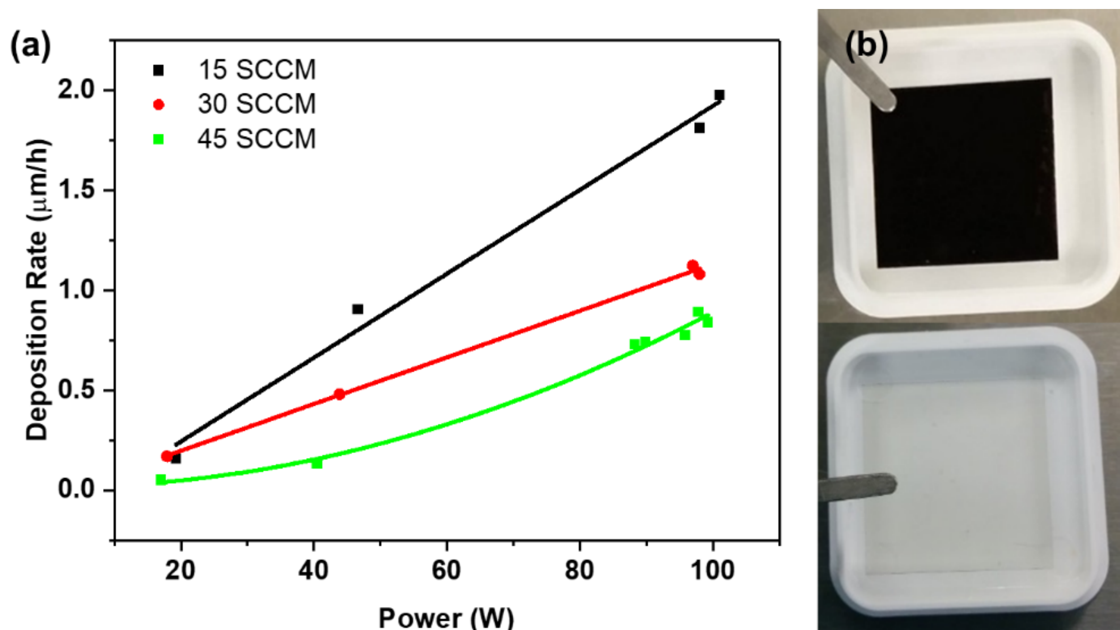

Figure 4.1: (a) Sputter deposition rates as a function of sputter power and nitrogen flow rate. (b) Photographs of an as-deposited Zinc Nitride film (top) and the same sample after several weeks of exposure to ambient air (bottom).

The stoichiometry of the films deposited under these conditions varied from excessively Zn-rich to more stoichiometric Zn_3N_2. Evidence of this was seen initially in transmittance measurements, but also in quantitative EDS measurements. The transmittance spectra of three samples deposited at nitrogen flows of 15, 30 and 45 sccm and a constant sputter current of 200 mA are shown in **Figure 4.2**. The samples deposited at nitrogen flows of 15 and 30 sccm had very poor transmittance throughout the measured spectrum, which is characteristic of metallic films. For samples deposited at a nitrogen flow

rate of 45 sccm, a clear absorption edge and optical interference were observed in the region of 1000 nm.

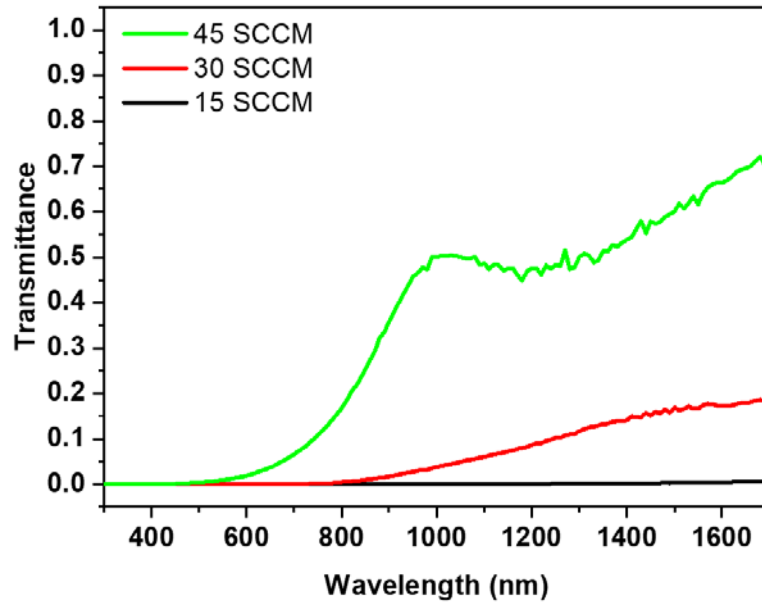

Figure 4.2: Transmittance spectra of samples deposited at a nitrogen flow of 15, 30, and 45 sccm and a sputter current of 200 mA.

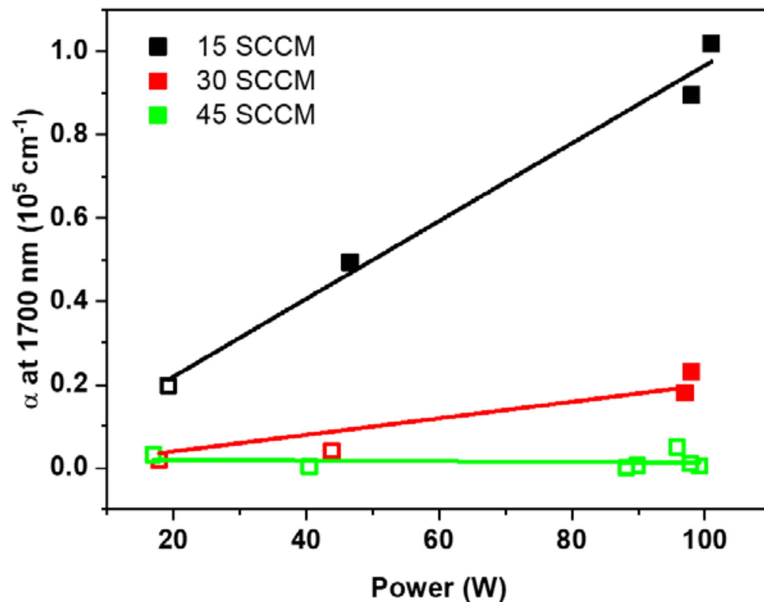

Figure 4.3: Absorption coefficient, α, of sputtered samples at 1700 nm as a function of sputter power and nitrogen flow. The unfilled data points indicate samples which were prone to oxidation.

A graph of the calculated absorption coefficient at 1700 nm for different deposition conditions is shown in **Figure 4.3**. The graph shows that films deposited at lower nitrogen flow rates and higher sputter powers were more absorbing in the near infrared. This was attributed to these samples being more metallic (Zn-rich), which was confirmed with

further investigation. On the other hand, samples deposited at higher nitrogen flow rates were close to stoichiometry. Furthermore, the samples that were not absorbing in the infrared were prone to oxidation (indicated by the unfilled points on the graph). This is further indication that the samples are close to stoichiometric Zn_3N_2, because Zn_3N_2 is known to oxidise in ambient, whereas metallic Zn films are stable. As a result, optimisation of the substrate temperature was performed on samples which were closer to the stoichiometry of Zn_3N_2, i.e. grown at a nitrogen flow rate of 45 sccm. A sputter current of 200 mA was selected to maximise the deposition rate. More characterisation of samples deposited in this study is shown throughout this chapter. A list of samples examined in this chapter (labelled *ZN-#*) is given in **Table 4.1**. To highlight the effects of oxidation on the properties of the deposited films, one of the samples is also examined after full oxidation had occurred (labelled ZN-3A).

Table 4.1: Growth conditions and thicknesses of Zn_3N_2 samples discussed in this chapter.

Sample	N_2 gas flow (sccm)	Substrate Temperature (°C)	Growth Duration (min)	Thickness (nm)
ZN-1	15	20	15	461
ZN-2	30	20	27	481
ZN-3	45	20	60	735
ZN-4	45	50	70	886
ZN-5	45	100	70	853
ZN-6	45	150	70	365
ZN-3A	45	20	60	1132

4.2. Surface morphology and film composition

The morphology and microstructure of the deposited films were investigated by SEM measurements. The images in **Figure 4.4** show the surface of samples ZN-1 to ZN-6 at 160,000x magnification. Sample ZN-1 consisted of randomly oriented flakes but a clearer grain structure emerged in ZN-2 to ZN-6 as the N_2 flow rate increased. The grains were approximately rhombic in shape with lateral dimensions of around 100 nm. As the substrate temperature increased in samples ZN-5 and ZN-6, the grain boundaries started to coalesce and became less apparent. Specifically, the surface of sample ZN-6 appeared to be more uniform and smoother when compared to that of the other samples. An improvement in surface morphology is expected for films that are grown at higher substrate temperatures.

This effect is associated with increased diffusion during growth which is enabled by the increased thermal energy.

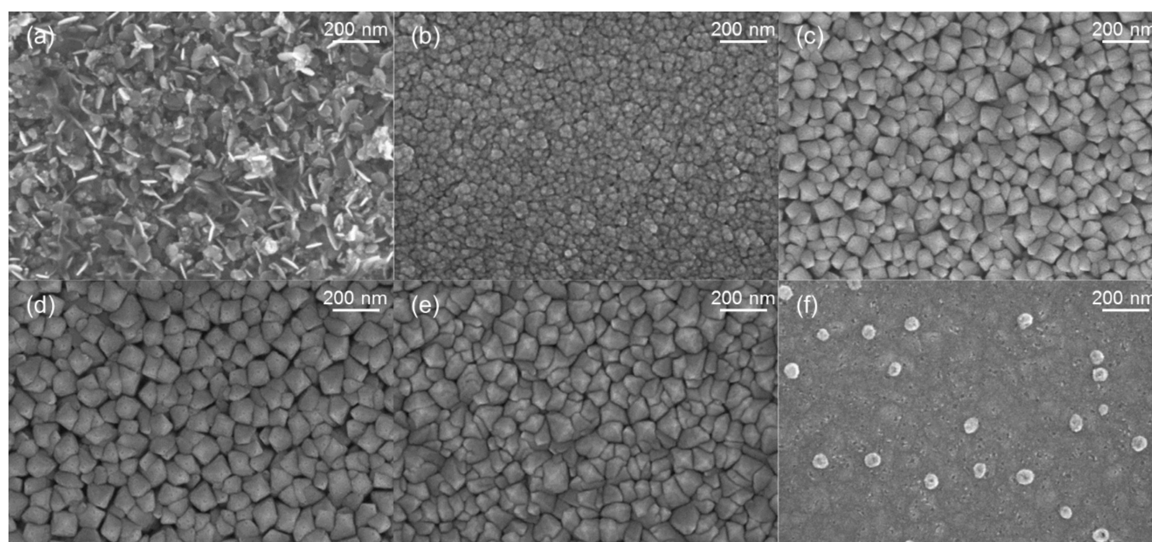

Figure 4.4: SEM images of samples: (a) ZN-1, (b) ZN-2, (c) ZN-3, (d) ZN-4, (e) ZN-5, and (f) ZN-6 at 160,000x magnification.

As a general indication of the film composition, a quantitative EDS analysis was performed on all samples. The following characteristic X-rays were identified in all samples: C: Kα at 0.277 keV, N: Kα at 0.392 keV, O: Kα at 0.525 keV and several Zn: L lines (Ll, Le, Lα, Lβ) in the region of 0.882-1.108 eV.[4,5] The compositional data obtained from analysis of the EDS spectra are listed in **Table 4.2**. It is noted that a varying amount of carbon and oxygen (3-6 at. % and 5-13 at. % respectively) was detected in all samples. The estimated composition of carbon and oxygen decreased as the analysis depth increased with accelerating voltage. This suggests that a significant portion of the measured carbon and oxygen were caused by surface contamination of the samples.

The estimated Zn:N atomic ratio for samples grown at different conditions is shown in **Figure 4.5**. It is noted in **Figure 4.5a** that the film composition approached stoichiometry at higher N_2 flow rates. Specifically, as the N_2 flow rate increased the average Zn:N ratio decreased from 1.92 to 1.55. At higher substrate temperatures, the average Zn:N ratio decreased further to 1.52, 1.41, and 1.27, as shown in **Figure 4.5b**. The improvement of the stoichiometry at higher N_2 flows suggests that the sputtering process was under N-poor conditions for N_2 flow rates lower than 45 sccm. The decrease of the Zn:N ratio at higher substrate temperatures suggests that Zn was being thermally reemitted during deposition. This was indicated by a significantly decreased deposition rate at 150 °C, shown in **Table 4.1**.

Table 4.2: Compositional data for different Zn_3N_2 samples as estimated by the quantitative analysis of EDS spectra.

Sample	C (at. %)	N (at. %)	O (at. %)	Zn (at. %)	Zn:N
ZN-1	5	29	11	55	1.92
ZN-2	6	30	12	51	1.69
ZN-3	4	34	9	53	1.55
ZN-4	6	33	11	50	1.52
ZN-5	4	38	5	53	1.40
ZN-6	4	38	11	48	1.27

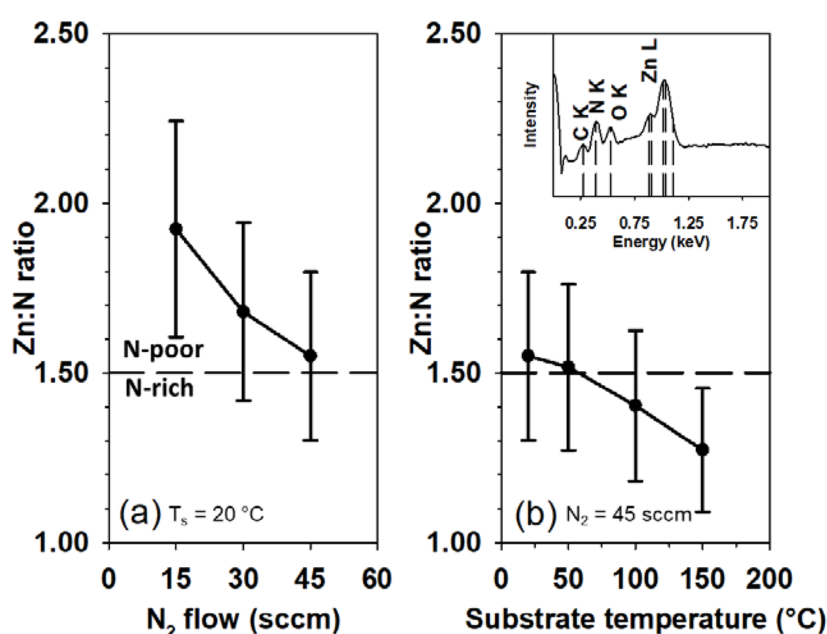

Figure 4.5: Zn:N atomic ratio of deposited samples as a function of (a) N_2 flow and (b) substrate temperature. The dashed line marks the stoichiometric Zn:N ratio of Zn_3N_2. Inset: The EDS spectrum of ZN-3.

The error bars displayed in **Figure 4.5** represent the systematic errors estimated by the quantitative EDS analysis, which is based on internal standards and depend on the atoms that are analysed. The experimental error between multiple measurements of the same sample were also considered but were insignificant. Because of the errors associated with measuring nitrogen by EDS, the relative error of the calculated Zn:N ratio is approximately 16%. Although that is a significant relative error, it is typical of standardless EDS analysis[6], which was performed here due to the lack of high-quality Zn_3N_2 standard samples. As a result, small fluctuations in the average Zn:N ratio should be interpreted with caution. In addition, there could be a systematic offset in the calculated Zn:N ratio because of the relative errors in the measurement of nitrogen by EDS. With that said, there is enough supporting evidence from analysis of X-ray Diffraction (XRD), Hall Effect and optical

measurements, discussed in the following sections, to suggest that the overall observed trend is real. As a result, it can be concluded from the EDS analysis that samples ZN-3 to ZN-6 were closer to stoichiometry, whereas ZN-1 and ZN-2 were significantly Zn-rich.

4.3. Crystal structure

Having confirmed the presence of both Zn and N in the deposited samples with EDS analysis, further evidence for the formation of Zn_3N_2 was obtained by XRD measurements. The XRD patterns of samples grown at different conditions are shown in **Figure 4.6**. Several diffraction peaks of the cubic anti-bixbyite crystal structure of Zn_3N_2 were identified in samples ZN-1 to ZN-6 and are listed in **Figure 4.6**.[7-9] The location of possible Zn diffraction peaks are marked by the asterisks in **Figure 4.6** and correspond to the (100), (101), (102) and $(2\bar{1}0)$ diffraction peaks of the Zn crystal structure at 39.09, 43.33, 54.46 and 70.82° 2θ respectively.[10] The broad and weak features observed in samples ZN-1 and ZN-2 are indicative of a defective polycrystalline structure. In sample ZN-1 there is an overlap between some of the peaks of the Zn_3N_2 and Zn crystal structures, making interpretation of this diffraction pattern more difficult. The disappearance of some of these features in the XRD pattern of ZN-2 suggests they are related to a Zn phase which is evident only in samples deposited at the most Zn-rich conditions.

The narrower features observed in samples ZN-3 to ZN-5 show that there was an improvement in the crystal structure of the films deposited under these conditions. As discussed in Chapter 2, (400) is the strongest (100)-oriented diffraction peak in the Zn_3N_2 crystal structure, and it is commonly the preferred orientation in polycrystalline Zn_3N_2 samples.[11] This was observed in samples grown at a nitrogen flow rate of 45 sccm, in which the (400) peak became the dominant feature of the diffraction pattern. It is noted that the crystallinity of sample ZN-6 decreased, as evident by the broad (400) peak in its diffraction pattern, despite the higher substrate temperature during growth. This is likely related to the thermal desorption of Zn under these conditions (as indicated by the decrease in the deposition rate), which may affect stoichiometry and result in strain. This argument is backed by the EDS analysis presented in **§4.2**.

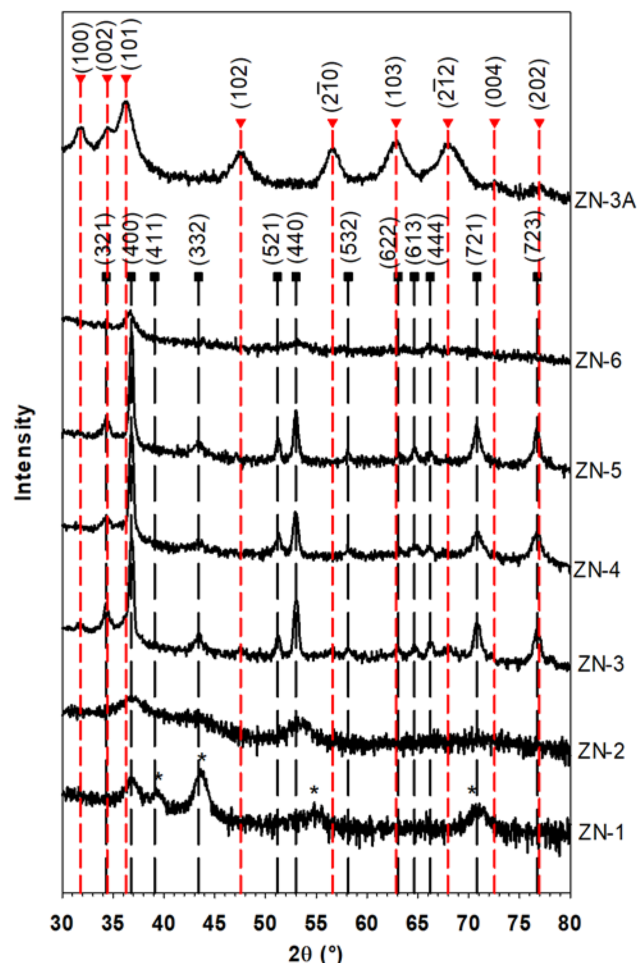

Figure 4.6: XRD patterns of Zn_3N_2 samples grown at different conditions. Rectangles and triangles indicate diffraction peaks attributed to crystal planes of Zn_3N_2 and ZnO crystal structures respectively. Asterisks indicate diffraction peaks related to crystal planes of Zn. The intensity axis is on a logarithmic scale.

Based on the positions of the (400) and (440) diffraction peaks, the lattice constant of the Zn_3N_2 samples was calculated at ~9.77 Å, which is in good agreement with previous studies.[7,9,12] Finally, the XRD pattern of sample ZN-3A revealed that the Zn_3N_2 films were converted to a ZnO-based crystal phase after prolonged exposure to ambient air.[13] This is indicated by the complete transformation of the diffraction pattern of ZN-3A, which is clear evidence that the as-deposited and oxidised samples are distinctly different materials. After full oxidation, the ZnO diffraction peaks (100), (002), and (101) were observed, amongst others of the ZnO crystal structure which are common in polycrystalline ZnO samples or ZnO powder.[14,15]

The results of the XRD measurements are in good agreement with the morphological and compositional analysis made by SEM/EDS. As seen in **Figure 4.4**, a more defined grain structure was observed in the better crystallised ZN-3 to ZN-5 samples. Furthermore, the same samples which exhibited a more oriented crystal structure were close to the

stoichiometric ratio of Zn_3N_2 as evident by the compositional analysis. In contrast, samples ZN-1 and ZN-2 which deviated to very N-poor stoichiometries were almost amorphous. The feedback of the crystal structure from XRD measurements assisted in identifying the growth conditions that resulted in the highest quality Zn_3N_2 samples.

4.4. Charge transport properties

To identify optimal deposition conditions in terms of electrical properties, the dependence of the electrical properties of Zn_3N_2 films on the deposition conditions was investigated by Hall Effect measurements. The resistivity, carrier concentration and carrier mobility derived from van der Pauw Hall Effect measurements are shown as a function of different growth parameters in **Figure 4.7**. The results for the sample set examined in this chapter are listed in detail in **Table 4.3**. Overall, the resistivity and carrier mobility of the films increased significantly with the N_2 flow rate, whereas the carrier concentration decreased, as shown in **Figure 4.7a, b**. As a function of substrate temperature, the resistivity and carrier mobility of the films consistently decreased and increased respectively, while the carrier concentration overall increased after reaching a minimum for the sample deposited at 50 °C. These parameters are shown in **Figure 4.7c, d**.

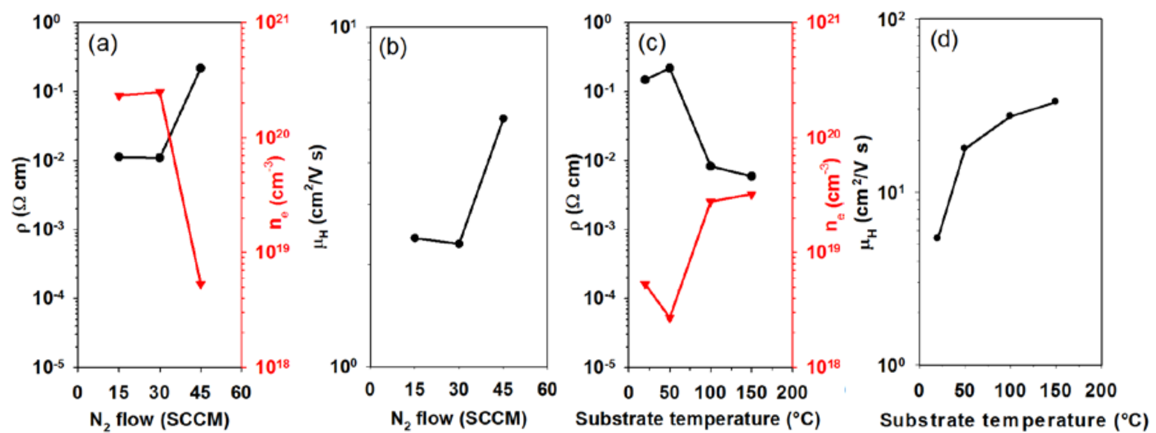

Figure 4.7: Resistivity ρ (circles), charge carrier concentration n_e (triangles) and mobility μ_H of deposited Zn_3N_2 samples as a function of (a, b) N_2 flow at room temperature, and (c, d) substrate temperature at a N_2 flow rate of 45 sccm.

To clarify the differences in the electrical properties of these samples, the resistivity and carrier mobility of different samples were re-plotted as a function of the carrier concentration in **Figure 4.8**. Two different profiles were observed in the dependence of resistivity and carrier mobility on the carrier concentration amongst the samples examined here. For the samples deposited on an unheated substrate, both the resistivity and carrier

mobility increased at lower carrier concentrations which were obtained by varying the growth conditions. Whilst it is difficult to definitively assess which types of defects or impurities are responsible for the decrease in carrier density, I will discuss here some possible candidates. Because n-type conductivity was maintained in all samples, and the samples were unintentionally doped to very high levels (10^{18}-10^{19} cm^{-3}), the discussion of n-type dopants to the Zn_3N_2 crystal structure is relevant. There are two types of common defects that are currently understood to be n-type dopants in Zn_3N_2. These are nitrogen vacancies and oxygen impurities.[16] If present within the crystal lattice in these samples, oxygen is an unintentional dopant. Therefore, although oxygen impurities may be contributing to the measured n-type doping, it is unlikely that the level of unintentional oxygen doping has changed significantly throughout these samples as they were deposited in the same chamber and under similar conditions. However, there is evidence for an improvement in crystal structure and stoichiometry from samples ZN-1 to ZN-4. As a result, it is suggested that the decrease in carrier density is caused by a decrease in the number of intrinsic defects such as nitrogen vacancies in samples grown at varying sputtering process conditions.

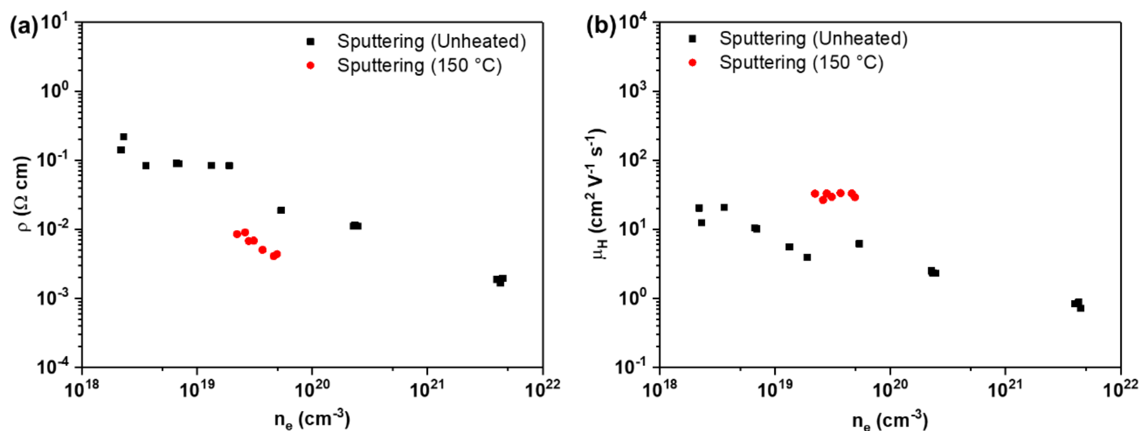

Figure 4.8: (a) Resistivity ρ and (b) charge carrier mobility μ_H as a function of carrier concentration for Zn_3N_2 samples grown at different conditions.

To interpret the improvement in mobility, it is worth discussing the parameters that affect charge carrier mobility in semiconductors. These parameters typically involve several scattering mechanisms such as scattering at phonons and neutral or ionised defects and impurities.[17,18] At high carrier concentrations, scattering at defects and impurities is typically the dominant scattering mechanism. Therefore, as the defect density decreased by 2 orders of magnitude in samples ZN-1 to ZN-3, the most likely explanation for the improved carrier mobility is that scattering at defects is significantly reduced (noting that

these defects are also responsible for the free carriers in the sample). A somewhat different profile was observed in the samples deposited at high substrate temperatures. Specifically, the resistivity was lower, and the carrier mobility was higher than other samples with similar carrier concentrations. In this case, the improvement in mobility cannot be attributed to decreased scattering at ionised impurities because it was obtained at a higher carrier concentration. Instead, the improvement in carrier mobility is attributed to the improvement in the morphology of the films deposited at these conditions, which was observed in the SEM images of these samples (**Figure 4.4e, f**). Because the surface of these samples is more uniform, scattering at grain boundaries is reduced which leads to the improved the carrier mobility. As the maximum mobility of ~33 cm^2 V^{-1} s^{-1} in these samples was achieved at a relatively high charge carrier concentration, further optimisation of the material quality should result in higher charge carrier mobility, which has been reported in previous studies.[19-22]

Table 4.3: Resistivity (ρ), carrier concentration (n_e) and carrier mobility (μ_H) of the different Zn_3N_2 samples discussed in this chapter.

Sample	Conductivity Type	ρ (Ω cm)	n_e (cm^{-3})	μ_H (cm^2 V^{-1} s^{-1})
ZN-1	n-type	1.13×10^{-2}	2.32×10^{20}	2.39
ZN-2	n-type	1.10×10^{-2}	2.48×10^{20}	2.30
ZN-3	n-type	2.18×10^{-1}	5.32×10^{18}	5.38
ZN-4	n-type	1.47×10^{-1}	2.70×10^{18}	17.80
ZN-5	n-type	8.28×10^{-3}	2.78×10^{19}	27.43
ZN-6	n-type	5.91×10^{-3}	3.23×10^{19}	33.18

4.5. Absorption coefficient and refractive index

The optical transmittance and reflectance spectra of different Zn_3N_2 samples as well as a fully oxidised sample are shown in **Figure 4.9**. As mentioned earlier, samples deposited at low N_2 flow rates, i.e. samples ZN-1 and ZN-2, were highly absorbing across the measured spectrum. Samples deposited at higher N_2 flow rates were more transparent in the infrared region, revealing an absorption edge around 1000 nm. The significant amount of excess Zn in samples ZN-1 and ZN-2 combined with their poor morphology, evidenced by SEM/EDS, are the cause of their poor transparency throughout the measured

spectrum. The observation of optical interference oscillations in samples ZN-3 to ZN-6 shows there was an improvement in the microstructure and thickness uniformity of the films, which reduce optical scattering. The transmittance spectrum of the oxidised ZN-3A sample shows that the absorption edge shifted to the UV region at around 400 nm after prolonged exposure to ambient, which resulted in the drastic difference in the appearance of the as-grown and oxidised material shown in **Figure 4.1b**.

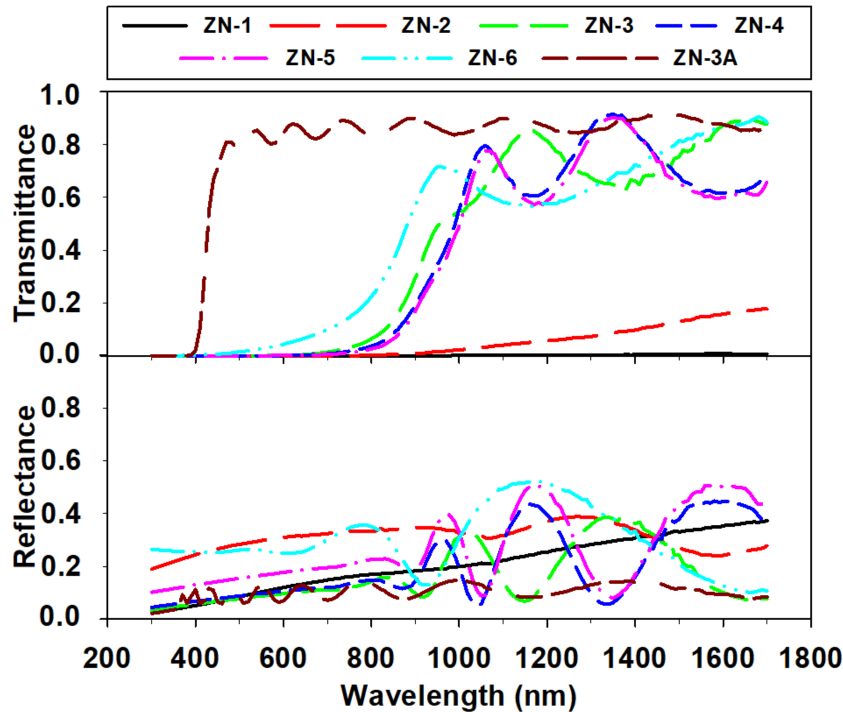

Figure 4.9: Optical transmittance and reflectance spectra of sputtered Zn_3N_2 samples deposited at different conditions.

To further investigate the optical bandgap of these films, their absorption coefficient was calculated from optical measurements. The absorption coefficient of ZN-3 is shown in **Figure 4.10a**. The high absorption coefficient ($\alpha > 10^4$ cm^{-1}) obtained in region A shortly after the onset of absorption suggests that the dominant transition type is direct, as has been suggested in previous studies.[2,19,23,24] To estimate the optical bandgap, the expression $(a/hv)^{1/r}$ was plotted against the photon energy, hv. The optical bandgap was then assigned at the intersection of the extrapolated linear region with the energy axis of the diagram. This methodology is based on a property of the absorption coefficient which is derived from the Cody expression for the imaginary part of the dielectric function[25], and is commonly expressed in the following form:

$$\frac{a}{hv} \propto \left(hv - E_g\right)^r \quad (4.1)$$

where E_g is the optical bandgap and r is a constant which depends on the type of dominant transitions.

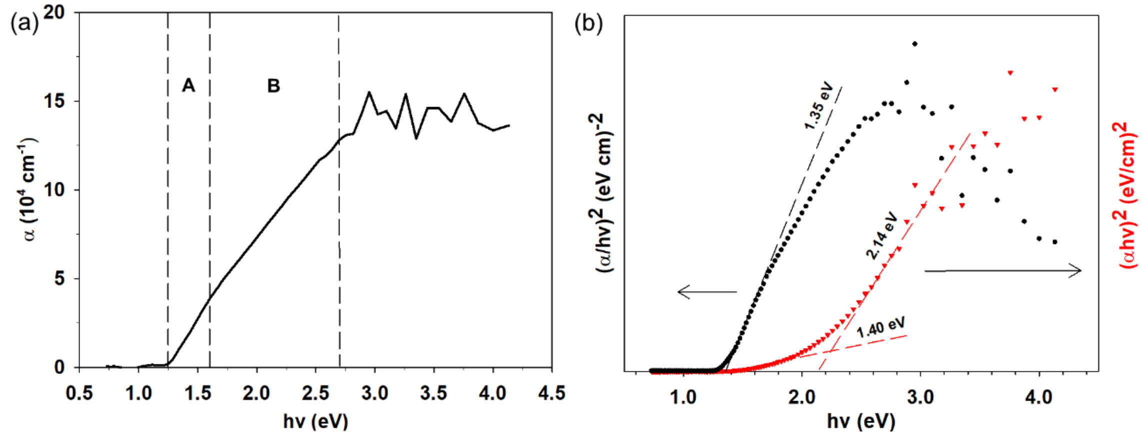

Figure 4.10: (a) Absorption coefficient as calculated for sample ZN-3. (b) Comparison of the Cody (left) and Tauc (right) expressions used to estimate the optical bandgap.

Using the value of $r = ½$ for a direct bandgap, it was found that the plots based on the Cody expression had a more distinct linear region and were easier to interpret than those based on the Tauc expression, $(ahv)^{1/r}$, which is more commonly used. This is demonstrated in **Figure 4.10b** which shows a comparison of the absorption plots obtained by using the two different expressions. When the Tauc expression is used, the estimated bandgap may range from 1.4 to 2.2 eV, because a reasonable linear fit ($R^2 > 0.99$) is obtained at a region extended above the absorption onset. The ambiguity in fitting the absorption plot to a linear region is caused by the shape of the absorption coefficient of Zn_3N_2. The increasingly high absorption, which is evident in these samples for energies greater than the absorption edge as shown in region B of **Figure 4.10a**, results in increasingly higher values of the Tauc absorption expression $(\alpha hv)^{1/r}$. Because absorption is normalised by the photon energy in the Cody expression $(\alpha/hv)^{1/r}$, the shape of the absorption plot is different, and can be easier to interpret. The Cody expression is known to describe highly absorbing films more accurately[26], which may be the reason that it is better suited for the analysis of Zn_3N_2 samples. It is evident for the analysis performed here that the use of the Tauc expression could easily lead to an overestimation of the optical bandgap of Zn_3N_2 samples in the range of 1.35-2.14 eV. As a result, it is suggested that such variance in the interpretation of absorption coefficient spectra is one of the contributing factors for the discrepancy in the bandgap values reported for Zn_3N_2.

The extracted optical bandgaps and calculated refractive indices from several samples are shown in **Figure 4.11a** and **Figure 4.11b** respectively. The as-grown Zn_3N_2

samples ZN-3, ZN-4, ZN-5 and ZN-6 shown here had optical bandgaps in the range of 1.3-1.5 eV and a refractive index in the range of 2.3-2.7. In contrast to the as-grown Zn_3N_2 samples, the optical bandgap of the oxidised ZN-3A sample was estimated at 3.44 eV and its refractive index was in the range of 1.6-1.8. This significant blue-shift of the bandgap in the oxidised material is clear evidence that it is a different material. It should be noted that the refractive index of the oxidised ZN-3A sample is closer to that of $Zn(OH)_2$ minerals[27] (~1.63) than to pure ZnO (1.9-2.1)[28], suggesting the material is more likely a mixed ZnO/$Zn(OH)_2$ phase. The formation of $Zn(OH)_2$ has been previously reported for Zn_3N_2 grown with a different technique, as a result of the reaction of Zn_3N_2 with water.[29] Although the XRD pattern of ZN-3A did not show a $Zn(OH)_2$ phase, the width of the ZnO peaks observed suggests there is a considerable number of structural defects and possibly deviation from stoichiometry.

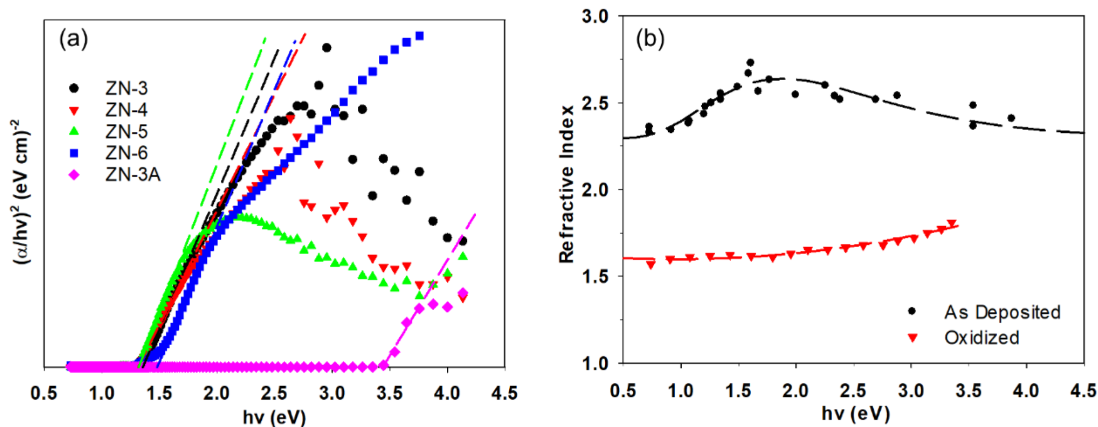

Figure 4.11: Absorption plots used to estimate the optical bandgap of several Zn_3N_2 samples and a fully oxidised sample. (b) The refractive index of as deposited and oxidised Zn_3N_2 films as estimated from optical interference extrema in reflectance spectra.

A comparison of the optical properties obtained here with those obtained in other studies for Zn_3N_2 is made in **Table 4.4**. The results from the analysis performed here are comparable to the results of Núñez, Pau *et al.* and Jiang, Georgiev *et al.*[20,30]. However, the optical properties reported by Ayouchi, Casteleiro *et al.* and Simil, Navas *et al.*[31,32] for Zn_3N_2 films are closer to the optical properties of the oxidised Zn_3N_2 samples. It should be mentioned that there is a well-known relationship between the refractive index and the bandgap of semiconductors.[33] That dependence can be described with empirical equations such as the Ravindra equation:

$$n = 4.16 - 1.12E_g + 0.31E_g^2 - 0.08E_g^3 \tag{4.2}$$

or with equations derived from the general theory of photoconductivity, such as the Moss relation:

$$n^4 E_g = 95\ eV \tag{4.3}$$

Because of this dependence, a larger bandgap often results in a lower refractive index. The observations made in **Table 4.4** follow this trend. However, the similarity between the optical properties reported for Zn_3N_2 in some of these publications and the properties of $ZnO/Zn(OH)_2$ supports the argument that wide bandgap reports for Zn_3N_2 are the result of unintentional oxidation rather than a difference in sample quality.

Table 4.4: Refractive index and optical bandgap of Zn_3N_2 films reported here and in other studies.

Material	Refractive Index	Optical Band Gap (eV)	Reference
Zn_3N_2	2.3-2.7	1.31-1.48	this study
Zn_3N_2	2.0-2.8	< 1.50	Núñez, Pau *et al.*[20]
Zn_3N_2	2.6-2.8	1.26	Jiang, Georgiev *et al.*[30]
$ZnO/Zn(OH)_2$	1.6-1.8	3.44	this study
Zn_3N_2	1.8-1.9	3.20-3.50	Simi, Navas *et al.*[31]
Zn_3N_2	1.7-2.4	3.20	Ayouchi, Casteleiro *et al.*[32]

4.6. Photoluminescence

Further investigation of the bandgap was done by performing photoluminescence (PL) measurements on the deposited Zn_3N_2 samples. Photoluminescence is a powerful method for determining the bandgap and other properties such as the presence of impurities or defects in a material. Photoluminescence in Zn_3N_2 samples is relatively rare in literature. In this study, photoluminescence features were only observed in samples deposited at certain conditions. Specifically, samples sputtered at a substrate temperature of 150 °C displayed relatively bright PL features at room temperature. The temperature dependence of the PL was also studied to observe transitions states which were not efficient at room temperature, and how the bandgap changes at low temperatures. The samples were placed in a He-cooled cryostat for the low temperature measurements. The temperature dependent PL for one of these samples is shown in **Figure 4.12**. The spectrum at T = 3.7 K featured a narrow band at 1.44 eV (band A) and a second band (band B) on the low-energy side of band A. With increasing temperature, the intensity of band A decreased, and its position

shifted to 1.38 eV at T = 300 K. The intensity of band B decreased rapidly with increasing temperature and it could not be resolved at elevated temperatures. In addition to these measurements, the optical bandgap of the sample was estimated as 1.43 eV at room temperature based on analysis of the optical measurements described in the previous paragraph. Therefore, it is evident from the PL measurements that the sample exhibited a photoluminescence band near the absorption onset at room temperature.

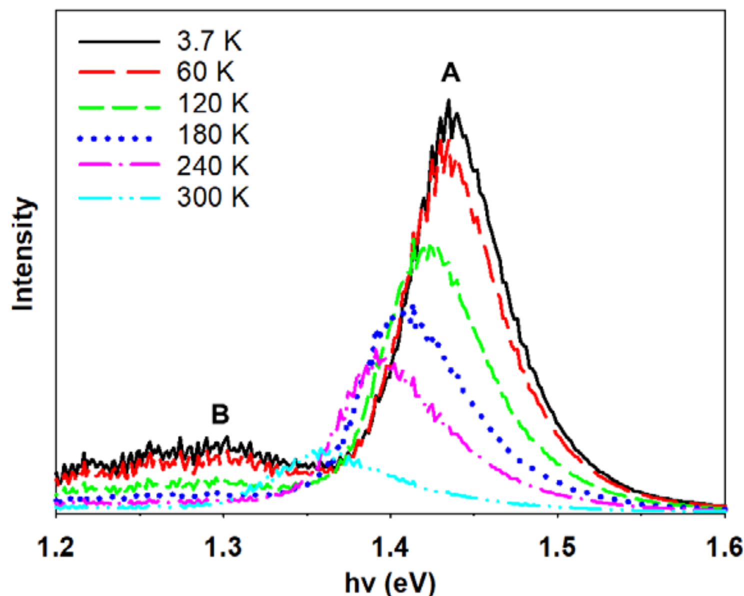

Figure 4.12: Temperature dependent PL of a sample shortly after growth. Measured with an excitation power of 30 mW.

Furthermore, the temperature dependence of band A, which is the highest energy band observed, matches the profile of band to band transitions. The observed red-shift with increasing temperature follows the well-known Varshni equation, which is an empirical equation that describes the effect of thermal vibrations on the bandgap of semiconductors.[34,35] Band A exhibits a high-energy tail, more clearly observed at T = 300 K. Such a band shape is indicative of transitions that involve the recombination of free carriers. The asymmetry of PL bands that involve free carriers is related to the kinetic energy of free carriers which has an exponential distribution function.[34] The FWHM of this band increases at higher temperatures because free electrons occupy states further from the conduction band. This observation correlates well with a high n-type carrier density which is evident for these samples with carrier concentrations in the order of 10^{19} cm^{-3}.

Since much of the debate over the bandgap of Zn_3N_2 is based on the possible effects of oxidation, the effect of ambient oxidation on the observed PL was also investigated. PL measurements of the same sample after prolonged exposure to ambient air are shown in

Figure 4.13a. The repeated measurements revealed the presence of a low-energy broad band at 0.90 eV (band C), in addition to bands A and B which were initially observed. The intensity of band C decreased with increasing temperature, however, its position did not shift. Bands A and B behaved similarly to the original measurements. The very large width and poor temperature dependence of band C suggest it is related to deep-level defects. Wei *et al.* observed a very similar feature and concluded that it is caused by deep-level states introduced by oxygen contamination of the Zn_3N_2 film.[36] A closer comparison of the spectra before and after prolonged exposure to ambient is shown in **Figure 4.13b**. The repeated measurement revealed that band A had blue shifted and decreased in intensity in comparison to the original measurement. The decrease in the intensity of band A with time shows that the sample had been partially oxidised resulting in decreased PL efficiency.

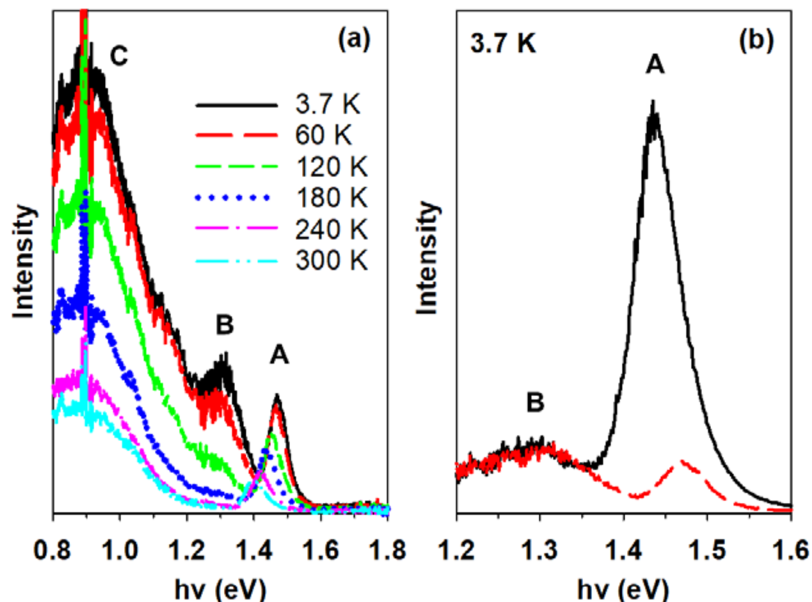

Figure 4.13: (a) Temperature dependent PL of the zinc nitride sample after prolonged exposure to ambient. (b) Comparison of the high-energy bands in the same sample before (solid) and after (dashed) prolonged exposure to ambient.

To provide more information on the origin of the observed high-energy bands, power dependent PL was performed at both low and high temperatures. The spectra in **Figure 4.14a, b** show low and room temperature measurements for different excitation powers. A red-shift in the emission energies of bands A and B was observed as the excitation power increased. Band C, which is not shown here, displayed a similar shift. Furthermore, the relative intensities of bands A and B changed significantly with excitation power. The intensities and emission energies of bands A and B at 3.7 and 294 K are plotted as a function of excitation power in **Figure 4.14c, d**. At low excitation powers band B was

more efficient than band A, but at higher excitation powers it deteriorated to the point where it could no longer be resolved, while band A reached a maximum intensity. The shift of the emission energies with excitation power was linear and occurred at a similar rate for both bands.

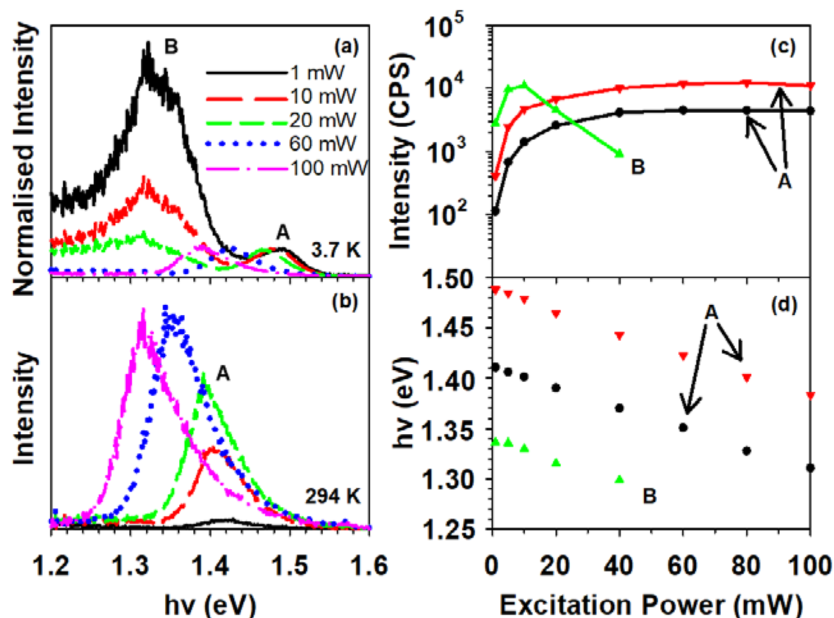

Figure 4.14: PL spectra of bands A and B at (a) 3.7 and (b) 294 K at different excitation powers. (c) Peak intensities and (d) emission energies of band A at 294 K (●) and bands A (▼) and B (▲) at 3.7 K as a function of excitation power. The spectra in (a) have been normalised at the maximum intensity of band A.

The saturation of band A with excitation power suggests that the recombination process involves a transition from or to a bound donor or acceptor state. At high excitation powers, these bound states are fully populated, resulting in a saturation of the PL intensity.[34] This is in contrast to the observations of Wei *et al.*, who reported a linear power dependence of a similar band and concluded it was caused by band-to-band recombination.[36] The observed red-shift with increased excitation power is more unusual. Such an effect may be observed in a Type-II transition, when high-energy photogenerated carriers overflow to nearby bands and subsequently relax to lower energy conduction band valleys. However, density of states calculations for Zn_3N_2 show no evidence for such band alignment in pristine Zn_3N_2.[12,16,37] Furthermore, the energy shift observed with excitation intensity is comparable to the shift observed in the temperature range of 3.7-300 K. As a result, the red-shift is too significant to be exclusively caused by a thermal effect due to the higher power density on the sample. Instead, we suggest that the observed shift with excitation power is related to inhomogeneities in the sample. For instance, defects may be introduced in oxygen-doped or strained regions of the sample which have a different conduction band

minimum than the rest of the film. As the excitation power is increased, the photogenerated carriers are activated and become more mobile, allowing them to relax to lower energy states. As a result, a red-shift is observed with increased excitation intensity. Prasada Rao *et al.* have observed similar behaviour in ZnO PL and attributed it to a high concentration of intrinsic defects.[38] Similarly, we suggest that this effect is related to structural defects and impurities specific to these samples. After further exposure to ambient, the samples became increasingly non-uniform and only emitted light with a similar power dependence from certain regions of the sample. After full oxidation there was no PL at these energies.

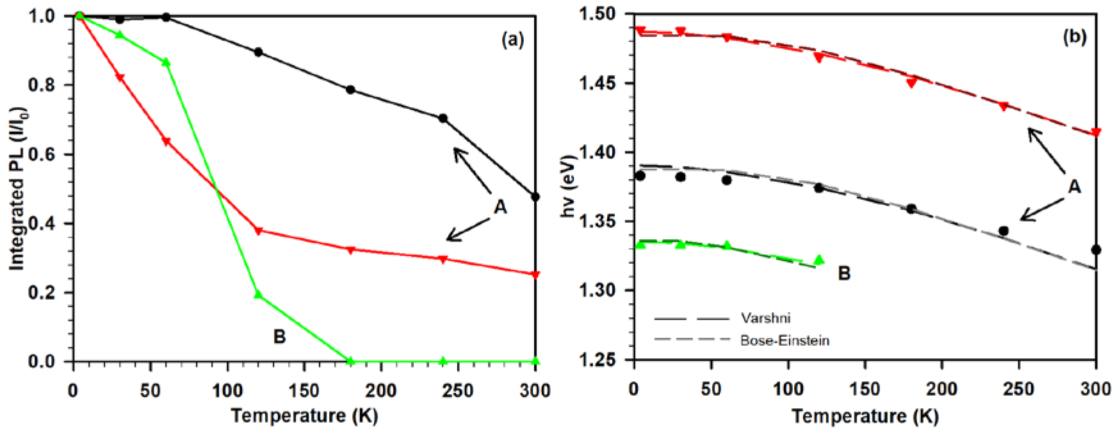

Figure 4.15: Temperature dependence of (a) relative integrated intensities (*I/I₀*) and (b) the emission energies of band A at an excitation power of 100 mW (●) and bands A (▼) and B (▲) at an excitation power of 1 mW.

The relative integrated intensities (I/I_0) of bands A and B at excitation powers of 1 and 100 mW are shown in **Figure 4.15a**. It is noticed that the thermal quenching of band A is offset to higher temperatures when excited with a power of 100 mW. This is an indication of heating caused by the laser, which affected the measurement of I_0 at the lowest temperatures and can, to some extent, be expected at high excitation powers. The temperature dependent intensities of these bands were used to calculate the activation energies (E_A) of the defects associated with these transitions, using the following equation:[39]

$$\frac{I}{I_0} = \frac{1}{1+\alpha_1 \exp\left(-\frac{E_{A_1}}{kT}\right)+\alpha_2 \exp\left(-\frac{E_{A_2}}{kT}\right)} \qquad (4.4)$$

From this analysis, the thermal quenching of band A was fitted more closely using two competitive non-radiative centres with activation energies of 50 and 5 meV. In contrast, the thermal quenching of band B was fitted with a lower activation energy of 36 meV. While the origin of these activation energies is not at present understood, the calculations are mentioned for future reference.

Finally, the emission energies of bands A and B at excitation powers of 1 and 100 mW are shown as a function of temperature in **Figure 4.15b**. To evaluate the temperature dependence of these bands, the data were fitted to the Varshni equation: $E_g(T) = E_{g_0} - aT^2/(T + \beta)$, and a Bose-Einstein function[40,41]:

$$E_g(T) = E_{g_0} - \frac{2a_B}{\exp\left(\frac{\Theta_E}{T}\right) - 1} \quad (4.5)$$

The dashed lines in **Figure 4.15b** show fits of the data with each function. The fitting parameters were $\alpha = 5.92\times10^{-4}$ eV/K, $\beta = 409.9$ K for the Varshni equation, and $\alpha_B = 65$ meV, $\Theta_E = 305.8$ K for the Bose-Einstein function. The Debye temperature of the material, calculated as $\Theta_D = 4\Theta_E/3$, is approximately 408 K. This is in good agreement with the Varshni parameter β, which is often related to the Debye temperature. However, these values are significantly lower than the computationally calculated value of ~610 K by Li *et al.*[42]

Whilst care must be taken in the use of the Varshni equation with PL results, the close fit and the fitting parameters, which are similar to other semiconductors such as GaAs[43,44], suggest again that the bands observed in this study originate from shallow defects in a narrow band-gap semiconductor. Other defects such as conduction band filling, band tail states, unintentional oxygen contamination and strain may still influence the observed band gap, potentially making it wider.[45,46] The significance of such effects remains to be investigated. However, the observation of PL which exhibits a temperature dependence typical of band to band transitions strongly suggests that the intrinsic bandgap of Zn_3N_2 is in the energy region of 1.4 eV, and ultimately sheds some light on the bandgap controversy surrounding Zn_3N_2.

4.7. Summary

The properties of Zn_3N_2 films deposited by reactive sputtering were discussed in this chapter. A variety of growth conditions were investigated by changing the N_2 flow and the substrate temperature during growth. This resulted in the growth of Zn_3N_2 with different microstructures and degrees of crystallinity. Hall effect measurements showed that the Zn_3N_2 films were highly doped in the order of 10^{18} cm^{-3}. The source of the doping is believed to be intrinsic structural defects. The carrier mobility increased up to 33 cm^2 V^{-1} s^{-1} in samples deposited at high substrate temperatures. This was attributed to a combination

of an improved microstructure of the films grown at these conditions and decreased scattering at defects.

Optical measurements showed that the Zn_3N_2 films had an absorption edge in the wavelength region of 1000 nm as the films became less metallic. The optical bandgap and refractive index of these samples were estimated in the range of 1.31-1.48 eV and 2.3-2.7 respectively. The Zn_3N_2 films had a high absorption coefficient, indicative of a direct bandgap semiconductor, as well as high absorption for energies above the bandgap. It is suggested that the Tauc analysis which is often used to extract the bandgap may lead to overestimation because of a high absorption above the bandgap. Furthermore, XRD and optical measurements of a fully oxidised sample revealed that the as-deposited Zn_3N_2 films were converted to a polycrystalline ZnO-based structure after prolonged ambient exposure.

Finally, the photoluminescence of the Zn_3N_2 films was studied. Samples grown at 150 °C displayed narrow features at around 1.40 eV which were attributed to recombination in shallow donor or acceptor states. The temperature dependence of the bandgap of Zn_3N_2 was observed by studying these bands at low temperatures. The observed PL was shown to follow the empirical Varshni equation in a manner that is comparable to other semiconductors. These results further suggest that Zn_3N_2 is intrinsically a narrow bandgap material. A red-shift of the observed bands with increased excitation power was attributed to inhomogeneities due to defects in the material.

4.8. Bibliography

1. C. G. Núñez, J. L. Pau, M. J. Hernández, M. Cervera, E. Ruíz, and J. Piqueras, Thin Solid Films **522,** 208 (2012).
2. C. G. Núñez, J. L. Pau, M. J. Hernández, M. Cervera, E. Ruiz, and J. Piqueras, Thin Solid Films **520,** 1924 (2012).
3. M. Gómez-Castaño, A. Redondo-Cubero, L. Vázquez, and J. L. Pau, ACS Applied Materials & Interfaces **8,** 29163 (2016).
4. M. O. Krause and J. H. Oliver, Journal of Physical and Chemical Reference Data **8,** 329 (1979).
5. J. A. Bearden, Reviews of Modern Physics **39,** 78 (1967).
6. N. W. Ritchie, Scanning **35,** 141 (2013).
7. G. Paniconi, Z. Stoeva, R. I. Smith, P. C. Dippo, B. L. Gallagher, and D. H. Gregory, Journal of Solid State Chemistry **181,** 158 (2008).
8. P. N. Taylor, M. A. Schreuder, T. M. Smeeton, A. J. D. Grundy, J. A. R. Dimmock, S. E. Hooper, J. Heffernan, and M. Kauer, Journal of Materials Chemistry C **2,** 4379 (2014).
9. D. E. Partin, D. J. Williams, and M. O'Keeffe, Journal of Solid State Chemistry **132,** 56 (1997).

[10] E. R. Jette and F. Foote, The Journal of Chemical Physics **3,** 605 (1935).
[11] G. Z. Xing, D. D. Wang, B. Yao, L. F. N. A. Qune, T. Yang, Q. He, J. H. Yang, and L. L. Yang, Journal of Applied Physics **108,** 083710 (2010).
[12] S. Yoo, A. Walsh, D. O. Scanlon, and A. Soon, RSC Advances **4,** 3306 (2014).
[13] Y. Xu and W. Y. Ching, Physical Review B **48,** 4335 (1993).
[14] J. Alvarez-Quintana, E. Martínez, E. Pérez-Tijerina, S. A. Pérez-García, and J. Rodríguez-Viejo, Journal of Applied Physics **107,** 063713 (2010).
[15] S. Hussain, Y. Khan, V. Khranovskyy, R. Muhammad, and R. Yakimova, Progress in Natural Science: Materials International **23,** 44 (2013).
[16] N. Jiang, J. L. Roehl, S. V. Khare, D. G. Georgiev, and A. H. Jayatissa, Thin Solid Films **564,** 331 (2014).
[17] L. Stilbans, Journal of Physics and Chemistry of Solids **8,** 123 (1959).
[18] S. S. Li, in *Semiconductor physical electronics* (Springer Science & Business Media, 2012).
[19] M. Futsuhara, K. Yoshioka, and O. Takai, Thin Solid Films **322,** 274 (1998).
[20] C. G. Núñez, J. L. Pau, M. J. Hernández, M. Cervera, and J. Piqueras, Applied Physics Letters **99,** 232112 (2011).
[21] N. Jiang, D. G. Georgiev, T. Wen, and A. H. Jayatissa, Thin Solid Films **520,** 1698 (2012).
[22] W. Peng, T. Tiedje, H. Alimohammadi, V. Bahrami-Yekta, M. Masnadi-Shirazi, and W. Cong, Semiconductor Science and Technology **31,** 10LT01 (2016).
[23] T. Suda and K. Kakishita, Journal of Applied Physics **99,** 076101 (2006).
[24] A. H. Jayatissa, T. Wen, and M. Gautam, Journal of Physics D: Applied Physics **45,** 045402 (2012).
[25] G. Cody, *Hydrogenated amorphous silicon, Part B, Optical properties, semiconductors and semimetals* (Orlando: Academic Press Vol, 1984).
[26] A. C. Diebold, in *Advances in Solid State Physics* (Springer, 2009), p. 371.
[27] J. W. Anthony, R. A. Bideaux, K. W. Bladh, and M. C. Nichols, (Mineralogical Society of America, Chantilly, USA).
[28] W. L. Bond, Journal of Applied Physics **36,** 1674 (1965).
[29] K. Toyoura, H. Tsujimura, T. Goto, K. Hachiya, R. Hagiwara, and Y. Ito, Thin Solid Films **492,** 88 (2005).
[30] N. Jiang, D. G. Georgiev, A. H. Jayatissa, R. W. Collins, J. Chen, and E. McCullen, Journal of Physics D: Applied Physics **45,** 135101 (2012).
[31] S. Simi, I. Navas, R. Vinodkumar, S. R. Chalana, M. Gangrade, V. Ganesan, and V. P. M. Pillai, Applied Surface Science **257,** 9269 (2011).
[32] R. Ayouchi, C. Casteleiro, L. Santos, and R. Schwarz, physica status solidi (c) **7,** 2294 (2010).
[33] N. M. Ravindra, P. Ganapathy, and J. Choi, Infrared Physics & Technology **50,** 21 (2007).
[34] I. Pelant and J. Valenta, *Luminescence spectroscopy of semiconductors* (Oxford University Press, 2012).
[35] G. D. Gilliland, Materials Science and Engineering: R: Reports **18,** 99 (1997).
[36] P. C. Wei, S. C. Tong, C. M. Tseng, C. C. Chang, C. H. Hsu, and J. L. Shen, Journal of Applied Physics **116** (2014).
[37] Y. Kumagai, K. Harada, H. Akamatsu, K. Matsuzaki, and F. Oba, Physical Review Applied **8,** 014015 (2017).
[38] T. Prasada Rao, G. K. Goswami, and K. K. Nanda, Journal of Applied Physics **115,** 213513 (2014).

[39] M. Leroux, N. Grandjean, B. Beaumont, G. Nataf, F. Semond, J. Massies, and P. Gibart, Journal of Applied Physics **86,** 3721 (1999).
[40] L. Viña, S. Logothetidis, and M. Cardona, Physical Review B **30,** 1979 (1984).
[41] B. Pejova, B. Abay, and I. Bineva, The Journal of Physical Chemistry C **114,** 15280 (2010).
[42] Z. Li, P. Wang, H. Chen, and X. Cheng, Physica B: Condensed Matter **406,** 1182 (2011).
[43] Y. P. Varshni, Physica **34,** 149 (1967).
[44] J. L. Shay, Physical Review B **4,** 1385 (1971).
[45] V. Tiron and L. Sirghi, Surface and Coatings Technology **282,** 103 (2015).
[46] H. Gao, X. Zhang, Y. Zhao, and B. Yan, AIP Advances **7,** 025111 (2017).

Chapter 5: Zinc Nitride Grown by Molecular Beam Epitaxy

5.1. Molecular Beam Epitaxy of Zinc Nitride

The initial motivation behind the development of a Molecular Beam Epitaxy (MBE) growth process for Zn_3N_2 was to develop single-crystal growth on lattice-matched substrates. Because intrinsic defects are minimised in single-crystal material, studying single-crystal Zn_3N_2 will allow a better understanding of the high doping levels in Zn_3N_2. The conditions for the growth of Zn_3N_2 by an MBE process were investigated for this work and are discussed in this chapter. The grown materials were characterised for their structural, electrical and optical properties. The results obtained in the MBE-grown samples are compared and correlated to those obtained by reactive sputtering throughout the chapter.

5.2. Growth process parameters

To enable the MBE growth of Zn_3N_2, two aspects of the growth process were initially established:

a) the generation of a molecular Zn beam, and
b) the generation of active nitrogen species.

The most common approaches to nitride MBE growth utilise ammonia or molecular nitrogen as the source of nitrogen species. The latter approach was used here. Because molecular nitrogen is chemically inert, it is common to form a plasma from nitrogen gas an with an RF plasma source which generates active nitrogen species. The conditions for the operation of a conventional RF nitrogen plasma source and the thermal evaporation of Zn are discussed first. Another aspect of the MBE growth process is substrate preparation to generate an active surface for growth initiation. Although the literature on Zn_3N_2 MBE is limited, the previously published studies acted as a general guideline for the initial investigations.[1-3] The growth process was initially investigated on glass substrates, and later yttria-stabilised zirconia (YSZ) and a-plane sapphire substrates.

5.2.1. Nitrogen plasma conditions

An RF plasma source manufactured by Veeco was used to introduce active nitrogen species into the chamber. A high purity nitrogen gas line (99.9999%) was fed into a mass flow controller which was connected to the plasma source. The RF plasma source operates in two modes: high-brightness mode typically used for nitride growth, and low-brightness mode used for dilute nitride growth.[4,5] Photographs of the plasma cell in the MBE chamber are shown in **Figure 5.1** for the two modes of operation. For the Zn_3N_2 growth process studied here, the plasma source was operated in high-brightness mode which generated a significant amount of active nitrogen species. The spectrum of the generated plasma was measured using an OceanOptics USB2000 portable spectrometer, with an optical fibre fitted to a window at the bottom of the plasma source. The plasma source could be operated in high-brightness mode at nitrogen flow rates of 1.5-4.0 sccm (standard cubic centimetres per minute) and RF powers of 175-450 W.

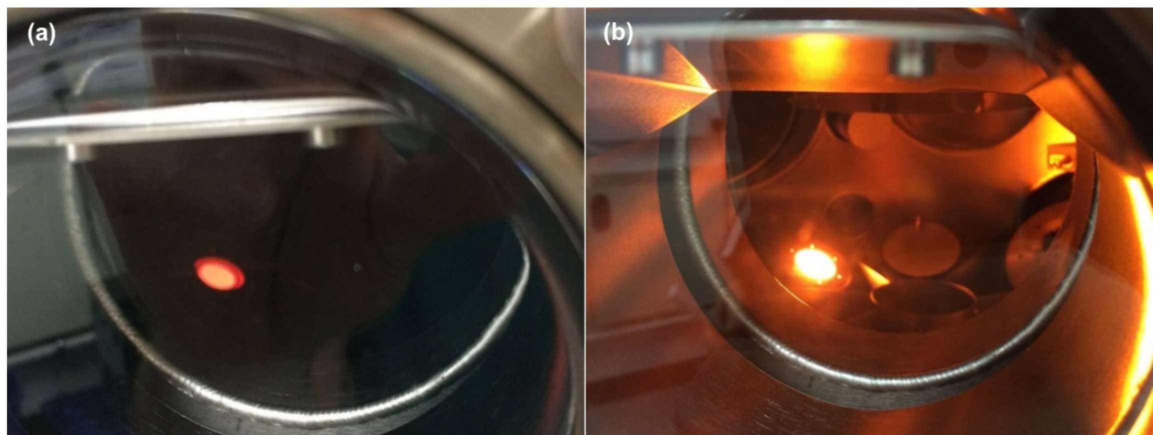

Figure 5.1: Photographs of the RF nitrogen plasma source operated in (a) low-brightness mode, and (b) high-brightness mode.

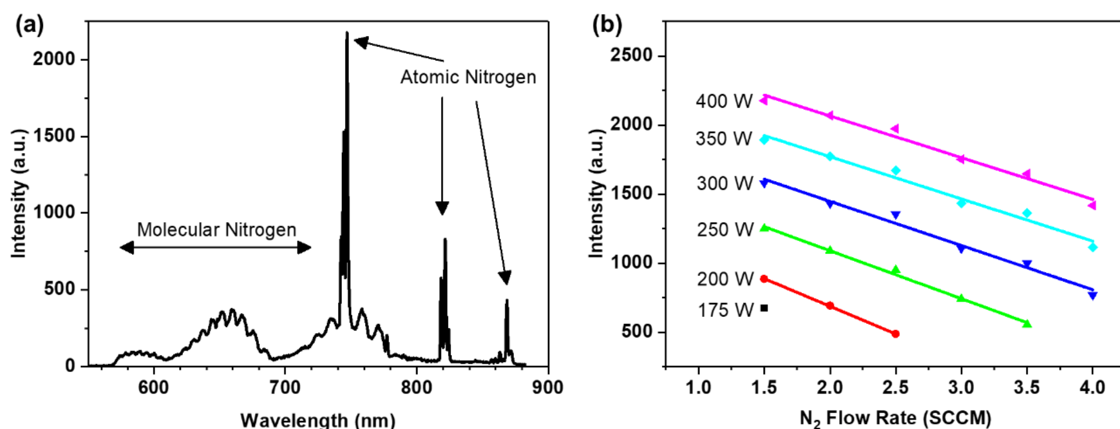

Figure 5.2: (a) Measured spectrum of the nitrogen plasma generated by the RF plasma source. (b) Intensity of the atomic nitrogen peak at 746 nm as a function of nitrogen flow rate and RF power.

The measured spectrum of the nitrogen plasma with the source in high-brightness mode is shown in **Figure 5.2a**. The sharp features observed at 747, 821 and 868 nm are well-known and associated with atomic transitions in nitrogen atoms.[6] In other words, the sharp spectrum features are an indication of the generation of active nitrogen species. On the other hand, the broad features in the low-wavelength side of the spectrum are associated with molecular nitrogen. The intensity of the strongest atomic nitrogen feature (746 nm) is shown in **Figure 5.2b** as a function of nitrogen flow rate and RF power. The graph shows that the intensity of the atomic nitrogen features decreased with increasing nitrogen flow rate but increased with increasing RF power. Previous studies of nitride MBE growth have shown that the compound growth rate is proportional to the intensity of the atomic nitrogen peaks in the spectrum.[7] However, high plasma power can also be detrimental to growth by damaging the surface of the sample due to ion bombardment.[5] Based on previous Zn_3N_2 MBE studies, a flow rate of 1.5 sccm and an operating power of 250 W were used as the starting conditions for the investigation of the growth process.[1-3] A nitrogen flow rate of 1.5 sccm generated a pressure of approximately 6×10^{-5} mbar in the growth chamber.

5.2.2. Zn flux

The output of the Zn cell was measured over a range of temperatures using a quartz crystal monitor (QCM). The flux measurements were performed with the QCM positioned in front of the shutter. It was found that after opening the shutter on the Zn effusion cell, the Zn flux decreased noticeably for an extended period. The transient flux of the Zn cell is shown in **Figure 5.3a**. The flux settled at a lower value approximately 20 minutes after opening the shutter. Changing the target temperature of the Zn cell with the shutter open displayed a similar response time. Shutter transients are well-known in Molecular Beam Epitaxy and are related to heat being reflected from the shutter back into the cell.[8] However, the timescale observed for the transient flux of the Zn cell in this study is longer than that of, for instance, group III metals.[9] In this case, the shutter transient is material-specific and related to the high vapour pressure of Zn. To elaborate, temperature variations as the cell reaches equilibrium (e.g. after adjusting the temperature or opening the shutter) result in significant changes to the flux because of the high vapour pressure of the evaporated material. Similar behaviour is known for As which responds very slowly to thermal adjustments.[10] As the time of the transient flux could not be reduced experimentally, the behaviour was accounted for and incorporated into the experimental process to ensure that

the flux measurements were reproducible, and that the Zn flux remained constant for the duration of each experiment.

Zn has a relatively low melting point of ~420 °C, and sublimates at temperatures lower than its melting point.[11,12] As a result, a considerable flux was obtained with the Zn cell heated in the range of 260-320 °C. The sublimation and evaporation processes for metals are known to follow an Arrhenius dependence.[13] The Arrhenius equation is a formula used to describe the temperature dependence of the rate of a reaction and has the following form:

$$J = Ae^{-\frac{E_a}{k_B T}} \tag{5.1}$$

where J is the rate constant (in this case the Zn sublimation rate), A is a proportionality constant, E_a is the activation energy for the reaction, k_B is the Boltzmann constant, and T is the absolute temperature. An Arrhenius plot of the measured Zn flux is shown in **Figure 5.3b**. The observed temperature dependence of the Zn flux follows the expected Arrhenius equation well, as indicated by the linear dependence of the data on the Arrhenius plot. Zn arrival rates in the order of 400 nm/h were measured by the QCM at 320 °C, which were deemed satisfactory for the scope of the experiments presented in this work. The growth duration was in the range of 2-5 hours for the samples examined here.

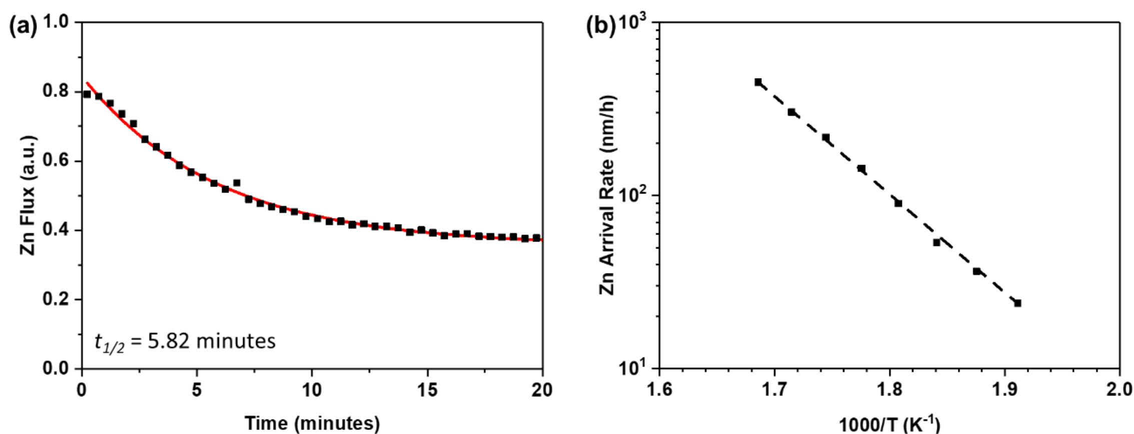

Figure 5.3: (a) Transient flux of the Zn cell after opening the cell shutter at $t = 0$. The cell shutter was opened as soon as the target temperature was reached (320 °C in this case). (b) Arrhenius plot of the Zn deposition rate measured by a QCM.

Early growth experiments indicated that substrate preparation is an important part for the deposition of Zn. Attempts to deposit Zn layers on glass resulted in no Zn deposition, even on an unheated substrate. As a result, the actual arrival rate of Zn could not be measured. Similar issues with the adhesion of Zn were reported in the thesis of M. Coke in the MBE growth of Zn/ZnO/Zn heterostructures.[14] Zn deposition in their experiments was

achieved after deposition of a thin wetting layer of Au on the surface of the substrate. In this work, the deposition of Zn layers was not investigated further, as it was not a vital component for the rest of the experiments.

5.3. Effect of experimental parameters on the growth rate

Zn_3N_2 was easily obtained under the presence of nitrogen plasma on unheated substrates. The initial conditions used for the nitrogen plasma source were a plasma power of 250 W and a nitrogen flow rate of 1.5 sccm. This result indicates that the presence of active nitrogen species was enough to initiate a reaction of the substrate surface with Zn, even on an otherwise untreated substrate. The thickness of the deposited samples was measured with ex-situ ellipsometry measurements using previously developed models for Zn_3N_2.

The effect of the following experimental parameters on the growth rate was investigated: (a) the Zn cell temperature, (b) the substrate temperature, and (c) the nitrogen plasma conditions. The semiconductor properties of these samples were also evaluated and are discussed in this chapter. It should be mentioned that the substrate temperature was measured by a thermocouple placed between the substrate heater and the substrate holder. Therefore, the actual substrate temperature may vary for the different sized and metal-coated substrates discussed in this chapter, so the temperatures mentioned here should only be considered suggestive of the actual temperature of the substrate, especially at the surface. With that said, when using identical substrates, the temperature measurements are consistent and directly comparable between different samples.

5.3.1. Zn cell temperature

The measured growth rate of Zn_3N_2 on unheated substrates is shown for three different Zn cell temperatures in **Figure 5.4a**. An exponential increase of the growth rate with cell temperature was observed in the temperature range of 295-320 °C. As shown by analysis with the Arrhenius equation in **Figure 5.3b**, the Zn flux has an exponential dependence on the cell temperature. As a result, a linear dependence was observed when the measured Zn_3N_2 growth rate was plotted against the Zn arrival rate, as shown in **Figure 5.4b**. This observation is relevant in the determination of an optimum Zn/N ratio for the growth process, as well as the optimisation of the Zn_3N_2 growth rate.

At a very high Zn flux the growth rate for the compound is expected to saturate at the point where the density of Zn atoms is greater than that which can react with the active nitrogen species. At fluxes higher than that point, the growth process will be N-limited and may be accompanied by the formation of metallic particles on the surface of the sample.[15] This is a common mechanism in MBE growth and has been reported for Zn_3N_2 previously.[1,2] The linear dependence of the Zn_3N_2 growth rate on the measured Zn arrival rate suggests that the growth process was still in a Zn-limited regime under the process conditions examined here.

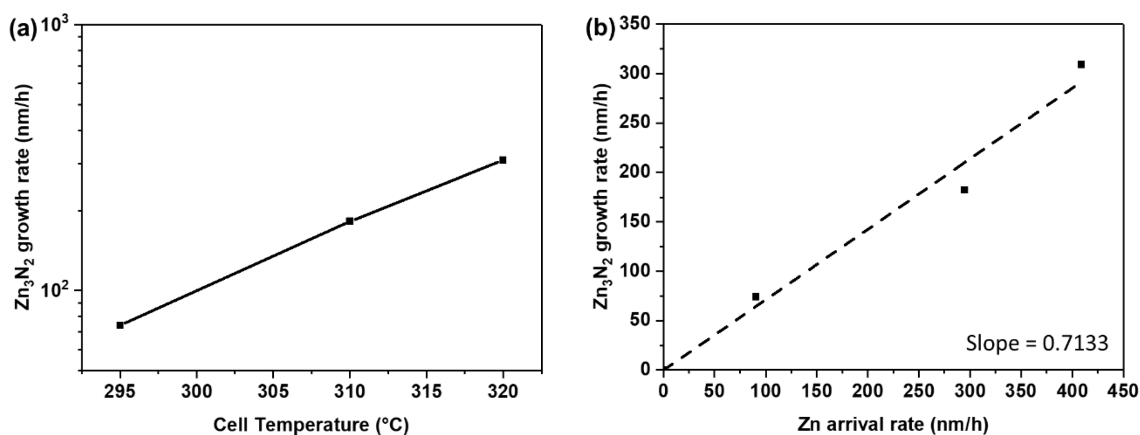

Figure 5.4: (a) Growth rate of Zn_3N_2 layers on unheated glass substrates at different Zn cell temperatures. (b) Measured growth rate of Zn_3N_2 films plotted against the Zn arrival rate measured in-situ with a QCM. The Zn_3N_2 film thickness was measured optically ex-situ.

A note should be made here about the slope of the line **Figure 5.4b**. If every Zn atom that reached a surface crystallised to form a Zn_3N_2 film then the Zn_3N_2 film would be approximately 30% thicker than a Zn film which contained the same number of Zn atoms; this is based on the density difference between Zn and Zn_3N_2. Therefore, under ideal conditions, the slope in **Figure 5.4b** should be approximately 1.3. Instead, the slope measured here is 0.7133. There are a few experimental parameters that may explain this discrepancy. First, the QCM is positioned at approximately 10 cm from the surface of the substrate. As a result, a tooling factor will apply to the QCM measurements, which could not be determined in these experiments due to difficulties in depositing Zn layers without the presence of nitrogen plasma. Second, whereas the Zn arrival rate was measured with a background pressure of 2×10^{-8} mbar, the Zn_3N_2 films were grown under a flow of nitrogen which generated a pressure in the order of 10^{-5} mbar. N_2 molecules which are not ionised during growth may affect the mean free path of Zn atoms, reducing the flux of Zn at the substrate. Finally, it is not necessary that the Zn beam should react in its entirety to form Zn_3N_2, because of the low sticking coefficient of Zn which was observed on bare substrates.

5.3.2. Substrate temperature

It was found that the growth rate of the Zn_3N_2 MBE process had a strong dependence on the substrate temperature in these experiments. More specifically, the growth process on untreated silicon and glass substrates disappeared at substrate temperatures as low as 150 °C. The observed drop in the growth rate with increased temperature is likely caused by a desorption of Zn from the growth surface at a faster rate than it can react with nitrogen species. Similar behaviour has been reported previously in $ZnSnN_2$ MBE by Feldberg *et al.* at substrates temperatures of 400 °C.[16] In Feldberg's experiments, issues with depositing Zn were observed at Zn:Sn ratios as high as 20:1, or in other words, under significantly Zn-rich conditions. To investigate this difficulty with growing Zn_3N_2 at high substrate temperatures, further samples were deposited with the Zn cell temperature set to 320 °C which resulted in the highest Zn flux for the range of parameters examined here. Two approaches were investigated to enable Zn_3N_2 growth at higher temperatures:

a) A two-step growth process in which a buffer layer was first deposited on an unheated substrate. The substrate temperature was then ramped to a target temperature (75-250 °C) for the second part of the growth process.
b) A thermal treatment of the substrate at a high temperature (800 °C), after which films were deposited at 75-150 °C.

Two-step growth process

It is common in epitaxial growth to grow a buffer layer that separates the substrate and the active layers in a structure. The use of buffer layers may serve various purposes; for instance: (a) to spatially separate the growth surface from impurities present on the surface of the substrate, (b) to control the generation of dislocations and other defects, and (c) to provide an atomically smooth surface for growth, better than could be achieved by substrate preparation.[17] In heteroepitaxial growth, a buffer layer may be grown for similar reasons or to separate the growth surface from an oxide layer.[18] Here, the growth of a thin Zn_3N_2 buffer layer was used to simply provide a surface with which Zn atoms may have better adhesion. A set of samples were grown with varying growth duration for the buffer layer: 120 min, 30 min, and 5 min. The total growth duration was set to 270 min for these three samples, by increasing the duration of high-temperature growth with each sample. The substrate temperature for the high-temperature step in these experiments was set to 150

°C. The total thickness of these three samples is shown in **Figure 5.5a** against the duration for the buffer layer growth. As the duration for the growth of the buffer layer decreased, the thickness of the films decreased from 780 to 346 nm.

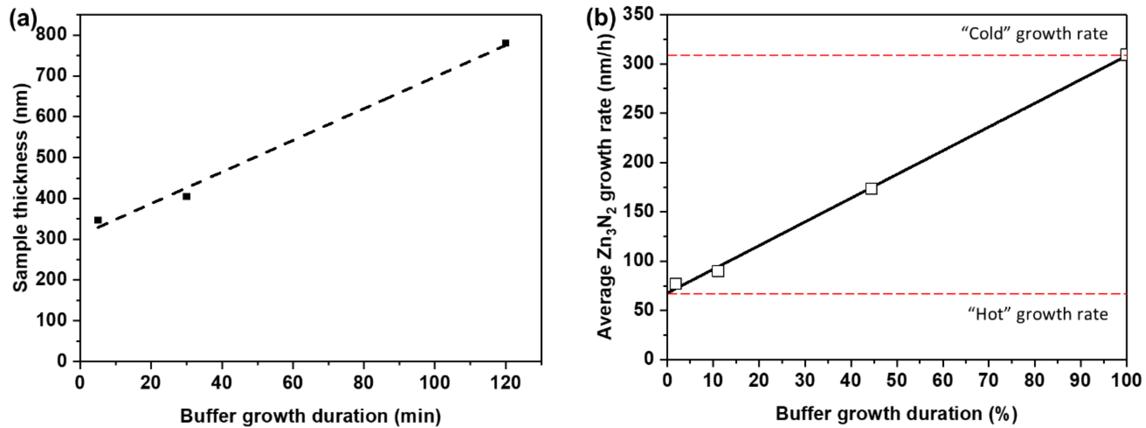

Figure 5.5: (a) Film thickness obtained with a two-step growth process for different durations of the buffer growth step. (b) Average growth rate plotted against the duration of the unheated growth step as a fraction of the total growth duration. Based on 270-minute experiments.

There are possibly two parameters contributing to the measured film thickness: the growth rate on the unheated substrate ("cold"), and the growth rate at 150 °C ("hot"). For this Zn flux, the average "cold" growth rate was measured in previous experiments at 309 nm/h. To determine whether there was a non-zero growth rate during the second part of the experiment, the average growth rate was plotted against the relative duration of the buffer layer growth. This graph is shown in **Figure 5.5b**. The data were fitted to the following linear equation:

$$y = Ax + B(x - 1) \quad (5.2)$$

where *A* and *B* are the two components of the measured growth rate. Parameters *A* and *B* were estimated as 308 nm/h and 68 nm/h respectively. As a result, the analysis of these samples shows that the growth of a buffer layer was successful in enabling the growth at 150 °C with an average growth rate of 68 nm/h. It is noted that if the growth rate on the buffer layer depended on the thickness of the buffer layer, then the points in **Figure 5.5b** would follow a non-linear trend, because parameter *B* would not be constant for different samples. As a result, this analysis shows that the Zn_3N_2 buffer layer thickness does not affect the "hot" growth rate. Instead, it is evident that the buffer layer provides a surface with which the Zn atoms can react faster than they desorb at 150 °C. Further samples to study the properties of films grown at higher temperatures were grown with a 5-minute buffer layer growth to minimise the thickness of the buffer layer.

Using the two-step process with a 5-minute buffer layer growth, the dependence of the growth rate on the substrate temperature was investigated further. The highest substrate temperature for which growth was observed was 200 °C. The results from these growths are shown in **Figure 5.6a**, which shows a sharp decrease of the average deposition rate with temperature. Similarly low growth rates were reported by Oshima and Fujita at 250 °C.[1] In addition, a similar drop-off in growth rate has been reported by Suda *et al.* in the temperature range of 200-450 °C.[3] The observation of growth at higher substrate temperatures by Suda *et al.* suggests they were using a different II/V ratio in their experiments (e.g. higher Zn flux). However, the Zn flux in these studies was measured in terms of pressure, so it cannot be directly compared to the experiments performed here. Furthermore, the substrate temperatures reported here are not directly comparable to these reported by Suda *et al.* because in this study substrate temperatures were measured with a thermocouple placed near the substrate holder. With that said, studies which have compared thermocouple and surface temperature measurements have found that the temperature at the surface of the substrate is generally lower (40-60 °C in the temperature range of 100-250 °C for a GaP wafer).[19]

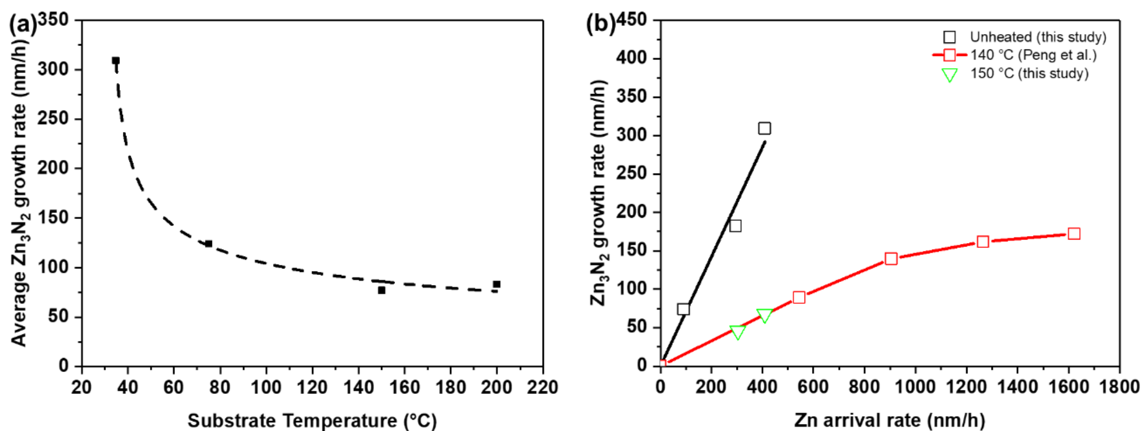

Figure 5.6: (a) Zn_3N_2 growth rate on glass as a function of substrate temperature. A 5-minute buffer layer was grown without heating the substrate to help initiate growth. (b) Growth rate as a function of the Zn flux on an unheated substrate and at 140-150 °C, using the data in this work and from Peng *et al.*[2]

A study by Peng *et al.* also reported the Zn arrival rate by QCM measurements.[2] The growth rates reported by Peng *et al.* are compared to those reported here in **Figure 5.6b**. This graph shows a good agreement between the growth rates reported here and by Peng *et al.* for a similar substrate temperature. Furthermore, it demonstrates that a significant surplus of Zn is evaporated compared to the small fraction which crystallises in the form of Zn_3N_2 at high substrate temperatures, evident by growth rates for the samples grown on an unheated substrate.

Thermal treatment of the substrate

Another approach that was investigated to enable Zn_3N_2 growth at high substrate temperatures is a thermal annealing treatment of the substrate. Previous MBE studies on Zn_3N_2 have reported similar treatment of crystalline substrates before growth, at temperatures as high as 800-1000 °C. Heating the substrate at such high temperatures can have the following effects: (a) reconstruction of atomic planes on the surface, which reduces roughness, and (b) decomposition and outgassing of contaminants on the substrate surface. Surface reconstruction achieved by thermal annealing is known to be beneficial to MBE growth, because it provides a smoother surface for the nucleation process.[20] In the presence of nitrogen plasma, nitridation of the surface may also occur, which can affect the initiation of growth and be beneficial to growth.[21,22]

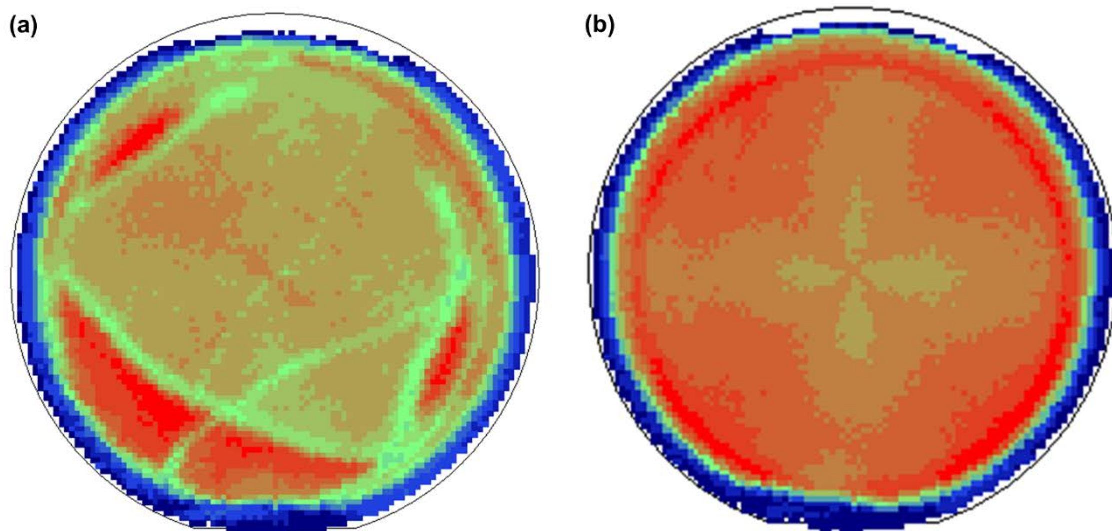

Figure 5.7: Surface maps of Zn_3N_2 growth on a-plane sapphire which had been thermally annealed at 800 °C (a) without back-coating, and (b) with a back-coating of 400 nm of Ti. These maps show the intensity of a white-light beam reflected off the surface of the sample.

The experiments for this investigation were carried out on a-plane sapphire and YSZ substrates. In contrast to the previous set of samples, no buffer layer was grown for these samples. The substrates were heated to 800 °C over 2 h and kept at that temperature for 40 minutes. The temperature was then lowered to the target temperature over several hours. Because a-plane sapphire and YSZ are both transparent, the effect of a metallic back-coating on the substrate was investigated. Metallic back-coatings (e.g. Ti, Mo) are used in GaN MBE to improve thermal coupling between the heater and a transparent substrate. Two Zn_3N_2 samples were deposited on thermally treated sapphire substrates; one without any back-coating, and one with a back-coating of Ti, which is used by some groups for

GaN MBE.[23] The Ti coating was approximately 400 nm and was deposited by sputtering. Surface maps of these two samples are shown in **Figure 5.7**. Zn_3N_2 growth was observed in both samples at 200 °C. However, growth on the uncoated substrate was only observed near the edges of the sample, indicated by the bright-red regions in **Figure 5.7a**. In contrast, growth on the substrate with the Ti back-coating was much more uniform, as shown in **Figure 5.7b**. The growth pattern of the uncoated sample suggests that the temperature of the substrate was not uniform during the thermal treatment process. AFM measurements performed on epi-ready and thermally treated substrates showed no significant changes in the surface of the substrates. Therefore, the mechanism responsible for enabling growth is likely thermal cleaning caused by the thermal treatment.

Table 5.1: Summary of growth rates obtained on heated substrates for the two pre-growth treatments discussed here.

Substrate	Pre-growth treatment	Substrate temperature (°C)	Average growth rate (nm/h)
glass, a-sapphire (2’’ diameter)	Two-step growth	200	83
YSZ (10×10 mm)	Two-step growth	200	59
YSZ (10×10 mm)	Thermal cleaning	150	46

Having shown that the thermal treatment was effective in enabling Zn_3N_2 growth at higher temperatures, the temperature dependence of the growth rate was investigated on YSZ substrates. The measured growth rates are shown in **Figure 5.8** for up to 150 °C. A similar drop in growth rate is observed as in the case of the two-step growth experiments. A summary of the growth rates obtained with the two pre-growth treatments discussed here in the range of 150-200 °C is shown in **Table 5.1**. The growth rates for the YSZ substrates were overall lower than for the a-sapphire and glass substrates. That is likely related to the size of the YSZ substrates (10×10 mm squares) which were smaller than glass and sapphire (2’’ wafers). The smaller substrate size results in a larger portion of the substrate holder being metallic, and therefore conducting heat more efficiently, which is likely to cause the actual temperature of the substrate to be higher. Furthermore, the average growth rate is lower for the YSZ sample grown without the buffer-layer step. This is attributed to the

thickness of the buffer layer which offsets the average growth rate for the two-step growth method, and other experimental sources of error such as variations in the Zn flux between experiments. Overall, the deposition rates reported here are close to those reported by Peng *et al.* for similar growth conditions, as shown in **Figure 5.6b,** and not far from other MBE studies of Zn_3N_2.

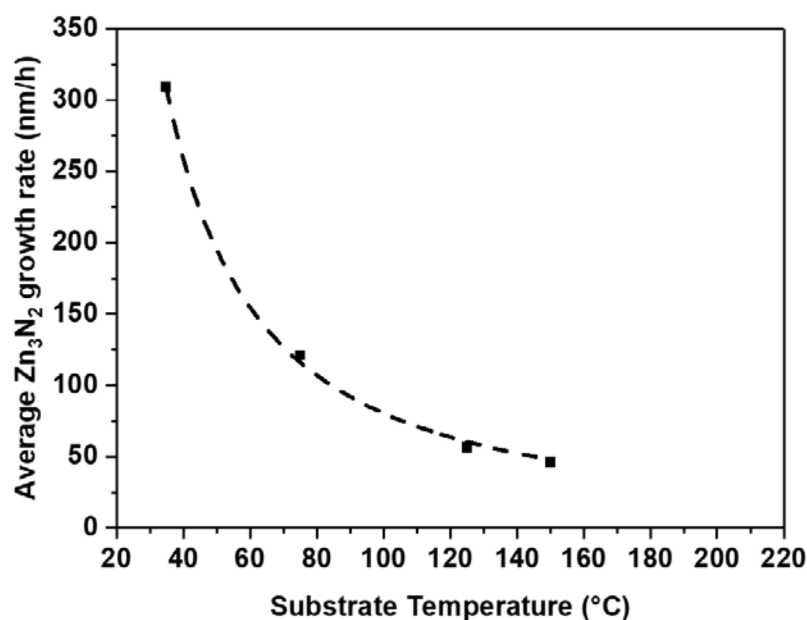

Figure 5.8: Average Zn_3N_2 growth rate as a function of substrate temperature for samples grown on YSZ without any buffer layers.

5.3.3. Nitrogen plasma conditions

The effect of the nitrogen plasma conditions on the growth of Zn_3N_2 was investigated next. From the analysis of the spectrum of the nitrogen plasma, shown in **Figure 5.2b**, it was shown that a higher flux of active nitrogen is generated at higher plasma powers and lower N_2 flow rates. The N_2 flow rate used up until now (1.5 sccm) is the lowest that could be controlled with the available mass flow controller. Early experiments indicated that higher N_2 flow rates were not beneficial for the growth process, so it was not investigated further. Instead, the plasma power was varied in three samples grown on YSZ substrates at plasma powers of 200, 250 and 300 W. The results are listed in **Table 5.2**.

There was a 17% decrease in the thickness of the sample grown at 200 W in comparison to the one grown at 250 W. This suggests that the growth process transitions to a N-limited regime in the range of 200 to 250 W. However, increasing the plasma power further to 300 W resulted in no film growth. This is discussed in **§5.4** which examines the crystal structure and surface morphology of the grown films.

Table 5.2: Summary of the film thicknesses obtained for different plasma powers. Based on 5 h experiments.

Substrate	Substrate temperature (°C)	Plasma Power (W)	Film thickness (nm)
YSZ	150	200	189
YSZ	150	250	230
YSZ	150	300	No film growth

5.4. Morphology and crystal structure

To investigate the structure of the MBE-grown samples, the surface morphology of the grown layers was investigated by Scanning Electron Microscopy (SEM) measurements, and the crystal structure was evaluated by X-ray Diffraction (XRD). The SEM images of samples grown at substrate temperatures of up to 200 °C with the two-step process are shown in **Figure 5.9**.

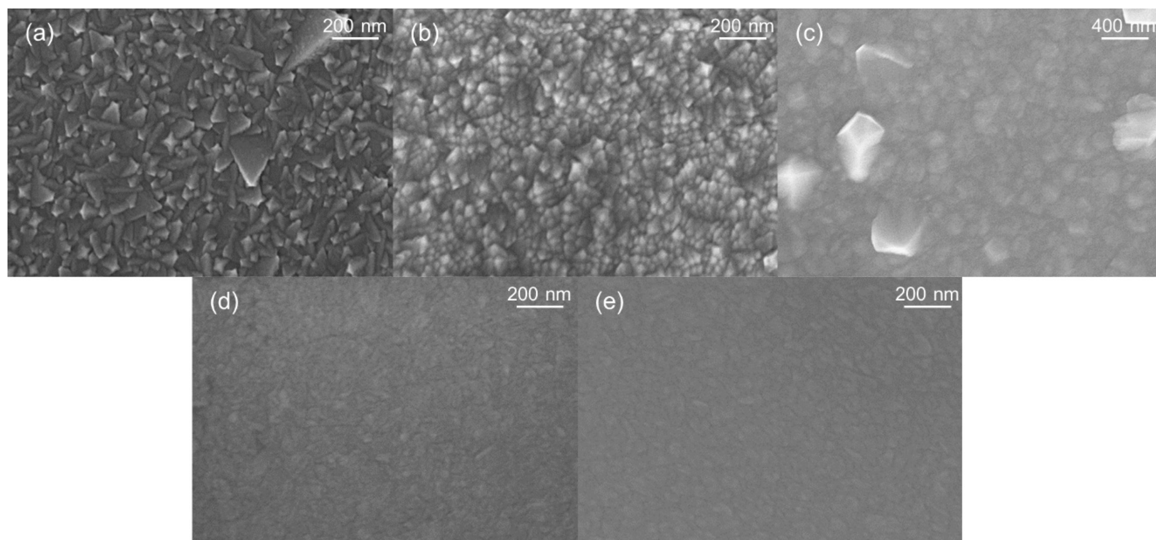

Figure 5.9: SEM images of Zn_3N_2 samples deposited (a) on an unheated substrate, at (b) 75 °C, (c) 150 °C, and (d) 200 °C on glass with a two-step growth process. Image (e) show a sample grown at 200 °C on a-plane sapphire.

The films grown at low temperatures displayed a rough surface, shown in **Figure 5.9a, b**. As the substrate temperature increased, the surface of the films became smoother and more uniform, up to 200 °C for glass and a-plane sapphire, shown in **Figure 5.9d, e**. The improved surface morphology is attributed to the increased energy during growth which allows atoms to diffuse as the crystals are formed. At 200 °C the surface morphology of the samples grown on glass and a-plane sapphire was similar.

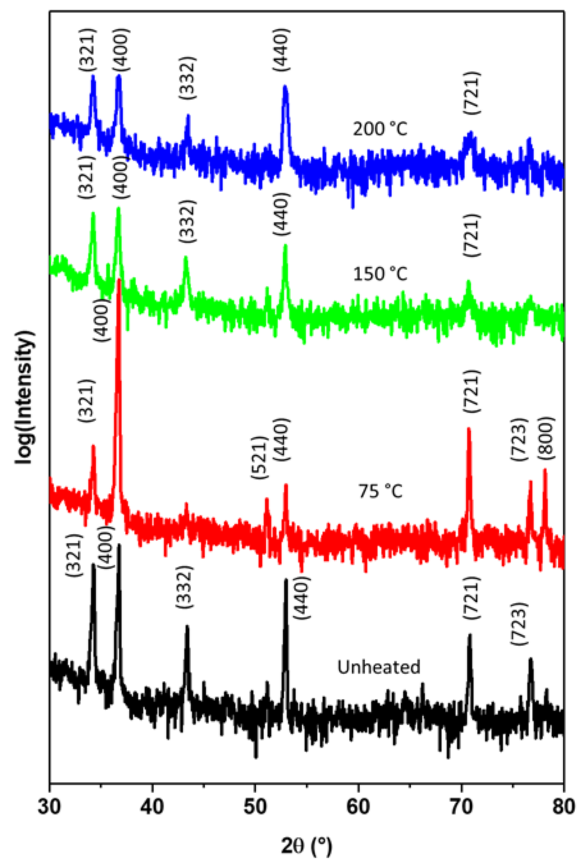

Figure 5.10: Out-of-plane diffraction patterns of Zn_3N_2 samples grown on unheated glass substrates and up to 200 °C with a two-step growth process.

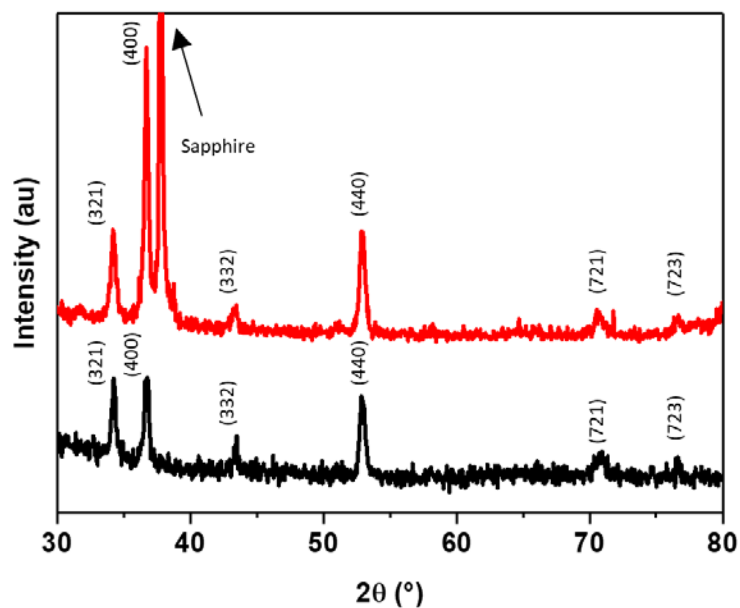

Figure 5.11: Out-of-plane diffraction patterns of Zn_3N_2 samples grown at 200 °C on glass (black) and sapphire (red) using a two-step growth process.

The diffraction patterns of Zn_3N_2 samples grown on glass for temperatures up to 200 °C are shown in **Figure 5.10**. Several diffraction peaks were observed and identified as part of the Zn_3N_2 anti-bixbyite crystal structure. As evident by the diffraction patterns, the deposited films were polycrystalline and displayed similar features as the sputtered Zn_3N_2 samples examined in the Chapter 4. The grown films were more (400)-oriented at a substrate temperature of 75 °C. At lower or higher temperatures, the ratio of the intensity of (400) to the rest of the peaks was lower. It can also be argued that the (440) peak is evolving at higher temperatures. The diffraction pattern of a sample deposited on a-plane sapphire at 200 °C is shown in **Figure 5.11**, where it is compared to a sample grown on glass under the same conditions. The sample grown on sapphire was more crystalline and more (400)-oriented compared to the sample grown on glass.

The decrease in orientation for the samples grown on glass may be related to the desorption of Zn at high substrate temperatures, which is evident by the significant decrease of the growth rate. This affects the stoichiometry of the grown films, resulting in increased strain within the crystal lattice. Similar behaviour was observed for the growth of sputtered Zn_3N_2 films in Chapter 4. The sample grown on a-plane sapphire is improved over the samples grown on glass under similar conditions. This is attributed to the approximate lattice matching between the substrate and Zn_3N_2 (lattice mismatch a-plane sapphire is approximately 6.5%).[1] However, there are other variables which prevent single-crystal or well-oriented growth, and which require further optimisation. These are the following: (a) the Zn:N ratio on the growth surface under the conditions for these experiments, (b) the substrate temperature, which may not be high enough to allow for sufficient diffusion of the deposited adatoms, and (c) an unoptimized growth surface provided by the buffer layer, which results in polycrystalline growth. To investigate the significance of the buffer layer surface, the next few samples were grown on YSZ without a buffer layer, using the thermal treatment described in **§5.3**.

The diffraction patterns and SEM images of samples grown on YSZ at substrate temperatures of 75-150 °C are shown in **Figure 5.12**. It can be argued that the samples grown on YSZ without a buffer layer became more (400) oriented at higher temperatures, as evident by the lack of other diffraction features, e.g. (440) and (721), which are more clearly observed in samples grown at lower substrate temperatures. In terms of surface morphology, the films became smoother at higher substrate temperatures, as evident by the SEM images.

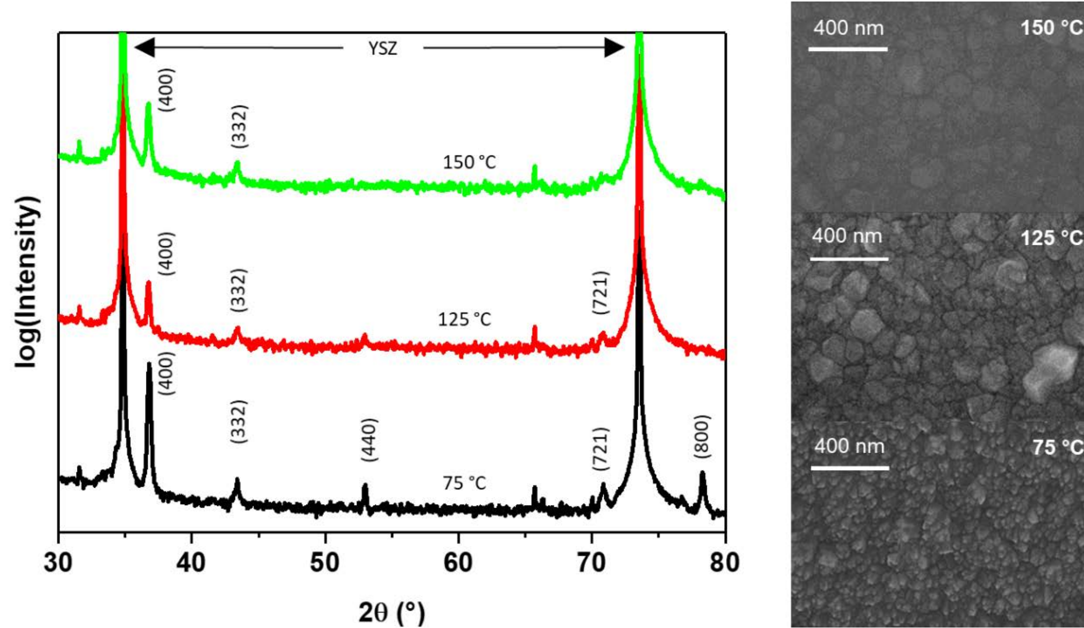

Figure 5.12: Diffraction patterns of Zn_3N_2 samples grown on YSZ at 75, 125 and 150 °C without a buffer layer.

Table 5.3: List of the FWHM of the (400) diffraction peak in Zn_3N_2 samples grown on different substrates with the two-step growth process.

Substrate	Substrate temperature (°C)	Plasma Power (W)	Film thickness (nm)	FWHM (°)
glass	Unheated	250	619	0.165
glass	75	250	650	0.145
glass	150	250	346	0.335
glass	200	250	458	0.384
a-plane sapphire	200	250	454	0.270

Table 5.4: List of the FWHM of the (400) diffraction peak in Zn_3N_2 samples grown on YSZ without a buffer layer.

Substrate	Substrate temperature (°C)	Plasma Power (W)	Film thickness (nm)	FWHM (°)
YSZ	75	250	606	0.137
YSZ	125	250	283	0.164
YSZ	150	250	230	0.201
YSZ	150	200	189	0.247

To investigate crystallinity further, the diffraction patterns discussed here were analysed by measuring the full-width half-maximum (FWHM) of the (400) peaks. The

results are listed in **Table 5.3** and **Table 5.4**, along with details about the growth conditions and the thickness of the samples. It is noted that the FWHM of the (400) peak reached a minimum of 0.145° at 75 °C and increased up to 0.384° at 200 °C for the samples grown on glass. The FWHM decreased to 0.270° for the sample grown on a-plane sapphire at 200 °C.

A similar trend of the FWHM was observed for the samples grown on YSZ. The FWHM of the (400) peak increases from 0.137° for the sample grown at 75 °C to 0.201° for the sample grown at 150 °C. When compared to the samples grown on glass and sapphire with the two-step growth process, the FWHM for the samples grown without a buffer layer was overall lower. This is shown in **Figure 5.13a** for several samples grown at different substrate temperatures. Although the overall trend shows that the FWHM increased at higher substrate temperatures, another variable that may affect the FWHM in XRD scans is film thickness. This is examined in **Figure 5.13b**, which shows the FWHM of different samples as a function of film thickness. This graph reveals that there is an overall trend of the FWHM decreasing in thicker layers. With that said, the samples grown directly on YSZ had better crystallinity and were more (400)-oriented than samples grown on other substrates or with the use of a buffer layer. This result suggests that if a buffer layer is to be utilised, its surface needs to be optimised, e.g. by thermal annealing after growth, to improve the crystal quality of the films grown on top of it.

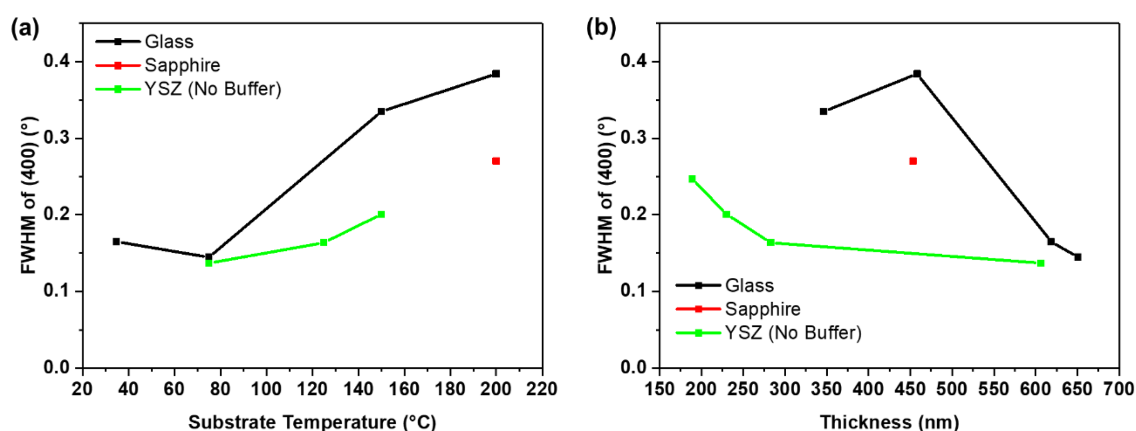

Figure 5.13: Full width at half maximum (FWHM) of the (400) diffraction peak as a function of (a) substrate temperature, and (b) thickness of different MBE-grown Zn_3N_2 samples.

The effect of the nitrogen conditions on the growth process was investigated by adjusting the power of the nitrogen plasma. Decreasing the plasma power to 200 W resulted in an increase of the FWHM of the grown film, as listed in **Table 5.4**. Increasing the plasma power to 300 W resulted in a non-uniform growth process which is shown in **Figure 5.14a**.

The SEM image showed features with dimensions in the order of 200 nm which did not form a film. A similar morphology was seen in a sample grown on a-plane sapphire without a buffer layer at 200 °C, shown in **Figure 5.14b**. A tilted view of the surface, shown in **Figure 5.15**, shows that these features were not only on the surface, but had considerable vertical dimensions. For both samples, XRR measurements suggest that there is a thin wetting layer in the range of 5-15 nm under the growth islands.

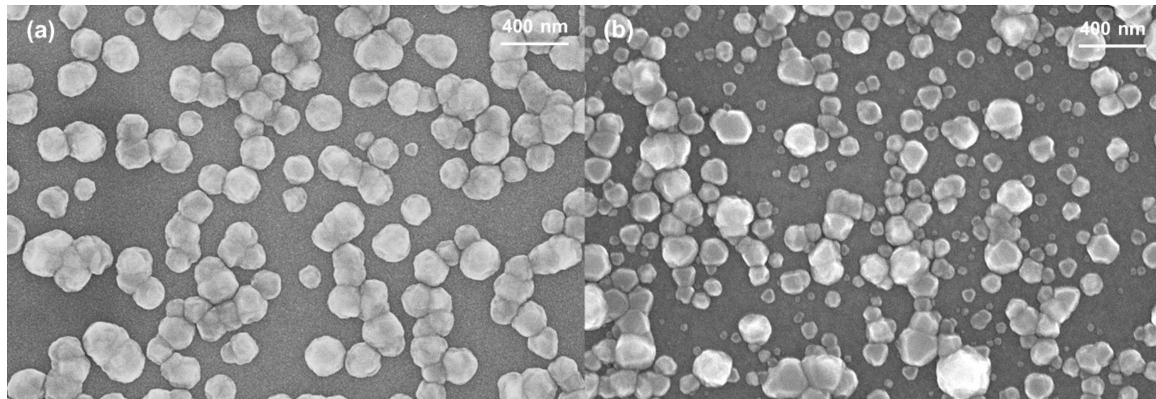

Figure 5.14: SEM images of samples where a uniform film grown was not observed: (a) At N-rich conditions with a plasma power of 300 W on a YSZ substrate, and (b) at 200 °C on a-plane sapphire. Both samples were grown without a buffer layer.

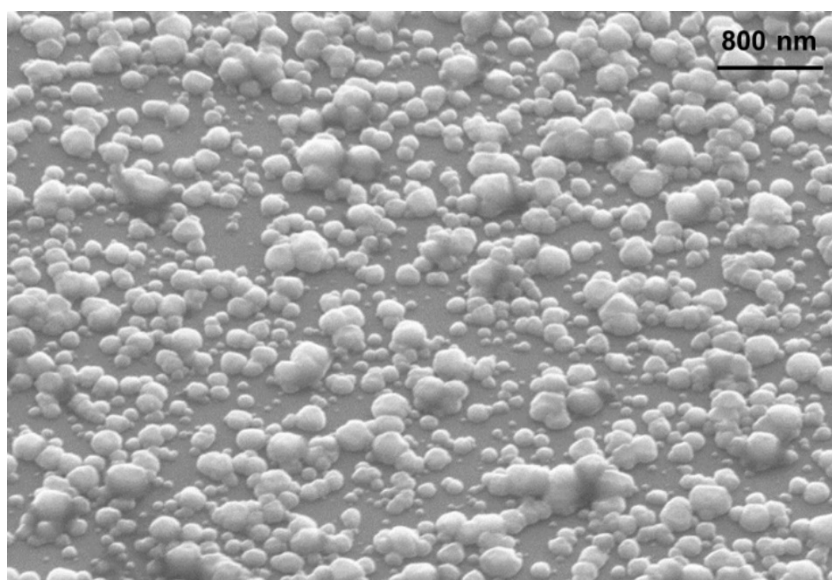

Figure 5.15: Tilted view (35° from normal) of the non-uniform growth on a-plane sapphire. No buffer layer was grown in this sample.

The features observed by SEM under these conditions resemble the Stranski-Krastanov growth model, in which interactions between adatoms are stronger than those between the adatoms and the substrate, leading to 3D island growth.[24,25] This kind of non-uniform island growth was observed in two cases in this study: (a) high nitrogen plasma power, and (b) high substrate temperatures. Increasing the substrate temperature further

resulted in no growth, which for the Zn flux investigated here was at observed temperatures between 200 and 250 °C. Increasing the nitrogen plasma power seems to have had a similar effect. This is possibly related to the excess energy which is introduced to the growth surface by the plasma, which has been reported to have detrimental effects to MBE growth.[5,26] As a result, it is concluded that both high nitrogen plasma power and high substrate temperatures can lead to a transition of the growth process to 3D island growth.

Although the range of experimental parameters examined in this study did not result in single-crystal growth, this initial investigation has identified issues with the desorption of Zn from the growth surface at high temperatures. To improve lattice matching between the grown films and the substrates in future experiments, fine tuning of the growth parameters will be required. It is concluded that a higher flux of Zn will be beneficial for the growth process of Zn_3N_2, to counterbalance the thermal desorption process at high temperatures. This will allow the substrate temperature to be optimised for lattice matched growth without introducing strain and defects due to deviations in stoichiometry. Furthermore, optimising the N_2 flow rate to maximise the active nitrogen species will likely be beneficial to the growth rate. Based on the trend observed in **Figure 5.2b** this will be achieved at lower nitrogen flow rates, which could not be investigated here.

5.5. Charge transport properties

To characterise the charge transport properties of the Zn_3N_2 samples grown by MBE, their electrical properties were investigated by room temperature Hall effect measurements. All examined samples were n-type and unintentionally doped. It is noted that the doping level was very high, reaching carrier densities in the order of 10^{19}-10^{20} cm^{-3}, and that the carrier mobility was in the range of 30-130 cm^2 V^{-1} s^{-1}. It should be mentioned that these values are comparable to other MBE studies of Zn_3N_2, even those which reported single crystal growth.[1-3]

The charge carrier density and mobility of films grown at different conditions are shown in **Figure 5.16**. The results from the Hall effect analysis are also listed in **Table 5.5** and **Table 5.6**. For samples grown at different Zn flux conditions, the carrier density and carrier mobility of the deposited samples increased as the Zn flux increased. This is shown in **Figure 5.16a, b**. It is difficult to attribute some of the trends observed for the carrier density directly to the process conditions. For instance, it is not immediately obvious why a higher Zn flux would lead to increased unintentional doping levels in the grown films.

Because the films grown at the higher Zn flux were thicker, the increased carrier density could be a result of defects introduced as the films crystallised at a greater distance from the substrate. However, if that were the case, i.e. if the carrier density was strongly dependent on film thickness, then it would correlate with the film thickness. The data listed in **Table 5.6** show that there is no such correlation. With that said, the observed increase in carrier density is more likely related to the conditions on the substrate surface during the nucleation process and the effect they have on defect propagation as the films crystallise. Although the carrier density increased at high Zn flux conditions, the highest Zn flux was selected for the investigations of the substrate temperature to maximise the growth rate.

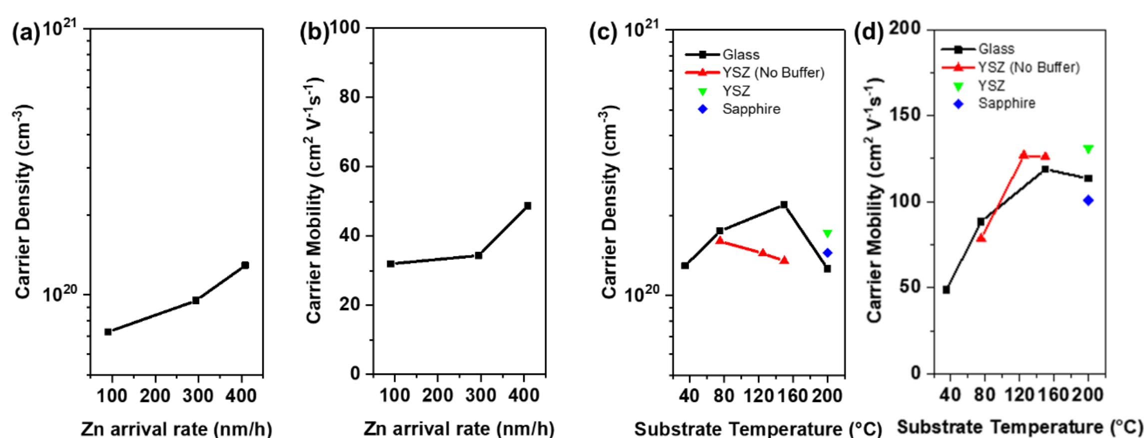

Figure 5.16: Charge carrier density and mobility for samples deposited at different (a, b) Zn arrival rates, and (c, d) substrate temperatures.

For samples grown at different substrate temperatures, the carrier density varied in the order of 10^{20} cm^{-3} but showed no clear correlation across all samples examined here, as shown in **Figure 5.16c**. The high carrier density observed for samples grown at high substrate temperatures correlates with the results obtained from XRD measurements, which showed that crystallinity was poorer at higher substrate temperatures. Because the samples studied here are unintentionally doped, the main suspects as the source of doping are structural defects (i.e. interstitials and vacancies in the crystal structure). Since the crystal structure was poorer in samples grown at higher substrate temperatures, it follows that the carrier density would not improve either. This conclusion is also valid for the samples deposited on different crystalline substrates which had similar levels of unintentional doping.

The carrier mobility, shown in **Figure 5.16d**, increased with substrate temperature up to 130 cm^2 V^{-1} s^{-1} for the samples grown at 150-200 °C. This improvement is attributed to an improvement in film uniformity, which is shown in the SEM images in **Figure 5.9**.

Grain boundary scattering is decreased in the smoother, more uniform films and results in an improved charge carrier mobility. The trend shown for the MBE samples in **Figure 5.16d** is comparable to that of the sputtered samples in **Figure 4.7d**.

Table 5.5: Charge transport properties for MBE samples grown at different Zn flux.

Substrate	Zn flux (nm/h)	Thickness (nm)	ρ (Ω cm)	n_e (cm^{-3})	μ_H ($cm^2 V^{-1} s^{-1}$)
glass	90	148	2.69×10^{-3}	7.27×10^{19}	32
glass	294	365	1.91×10^{-3}	9.52×10^{19}	34
glass	409	619	9.91×10^{-4}	1.29×10^{20}	49

Table 5.6: Charge transport properties for MBE samples grown at different substrate temperatures and on different substrates.

Substrate	Substrate Temperature (°C)	Thickness (nm)	ρ (Ω cm)	n_e (cm^{-3})	μ_H ($cm^2 V^{-1} s^{-1}$)
glass	75	651	4.04×10^{-4}	1.75×10^{20}	88
glass	150	346	2.39×10^{-4}	2.20×10^{20}	119
glass	200	458	4.37×10^{-4}	1.26×10^{20}	114
a-plane sapphire	200	454	4.28×10^{-4}	1.44×10^{20}	101
YSZ	200	326	2.76×10^{-4}	1.72×10^{20}	131
YSZ	75	606	4.97×10^{-4}	1.60×10^{20}	78
YSZ	125	283	3.42×10^{-4}	1.44×10^{20}	127
YSZ	150	230	3.68×10^{-4}	1.35×10^{20}	126

The resistivity ρ and carrier mobility μ_H of the MBE samples are plotted against the carrier density n_e in **Figure 5.17a, b** for different datasets. The graph includes the results obtained from sputtering. The MBE samples seem to follow a trend which was observed for the sputtered samples in both the resistivity and the carrier mobility. As the carrier mobility increases (and the resistivity decreases) in the more uniform films grown at high substrate temperatures, the carrier density also increases. As a result, the MBE samples have the highest mobility amongst the samples examined here, but also have the highest charge carrier density (apart from the metallic films deposited with sputtering). This trend is likely related to the crystal structure of the Zn_3N_2 samples examined here. For both the sputtered and MBE-grown samples, XRD measurements showed that the films had poorer

crystallinity when grown on a heated substrate, even though they were more (400) oriented in some cases. Structural defects which may be formed under these conditions, such as N vacancies, result in donor states being introduced to the density of states, which increases the carrier density. The data examined here suggests that such defects are very easily formed in the Zn_3N_2 crystal structure, resulting in degenerate levels of doping.

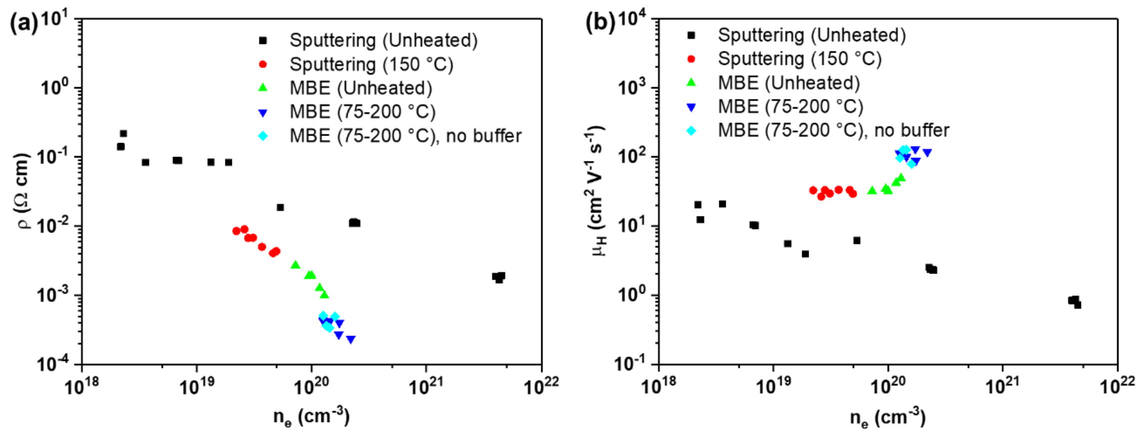

Figure 5.17: (a) Resistivity ρ and (b) charge carrier mobility μ_H as a function of carrier concentration for Zn_3N_2 samples grown at different conditions.

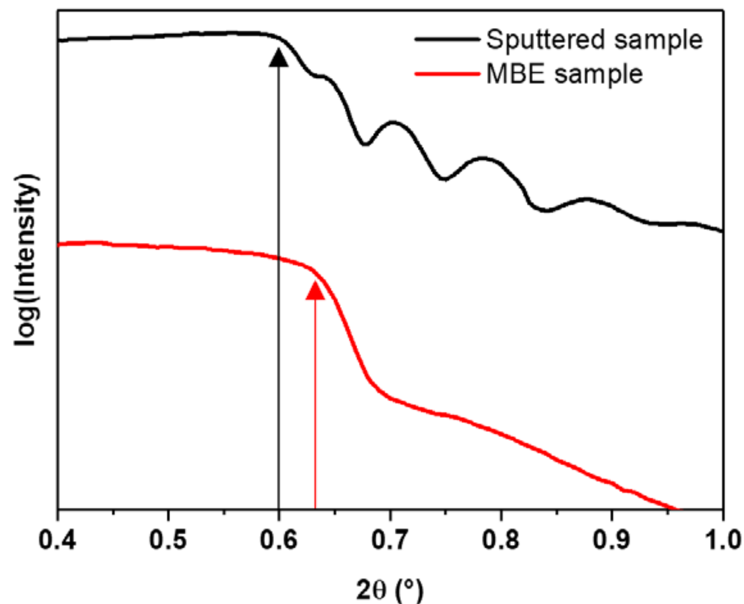

Figure 5.18: XRR scans of MBE-grown and sputtered Zn_3N_2 samples grown on glass substrates. The arrows show the critical angle in each sample, which is indicative of the density of the films.

Furthermore, there was a significant improvement in the carrier mobility between the sputtered and MBE-grown samples, which was accompanied by an increase in the carrier density by up to an order of magnitude. An important difference between the films obtained by the two techniques which has not been discussed until now is their density. X-ray Reflectivity (XRR) measurements suggest that the MBE samples had a higher density

than the sputtered samples. This is demonstrated by the difference in the critical angle of the XRR scans in **Figure 5.18**. From modelling of the XRR measurements it is concluded that the MBE samples had a density of ~6.0 g/cm^3, which is close to the theoretical density of Zn_3N_2. On the other hand, samples deposited by sputtering had a density of ~5.2 g/cm^3. These measurements show that the sputtered films were porous, which the surface morphology observed by SEM also suggests, whereas the MBE samples were more compact and dense films.[27] A side-effect of the higher density of the MBE samples is that they were more resistant to ambient oxidation. This was attributed to the MBE-grown films being less porous, which slows down the diffusion rate of oxygen and water vapour through the films. The oxidation process of Zn_3N_2 films is discussed in more detail in Chapter 7.

There have been theoretical and experimental studies on the effects of porosity on the effective properties measured in Hall effect measurements of conducting layers.[28,29] In these studies, it is discussed that both the carrier density and carrier mobility measurements are affected by geometrical factors in granular films. Hall mobility is expected to be lower in porous materials because of interparticle boundaries. Similarly, the carrier density within the porous material differs from the effective carrier density n^* by:

$$n_e = \frac{n^*}{A} \tag{5.3}$$

where A is a numerical factor determined by the shape of the particles ($A = \pi/4$ for close-packed spheres). As a result, it is concluded that the microstructure or porosity of the films is one of the contributing factors for the differences observed between the electrical properties of the sputtered and MBE-grown samples.

5.6. Optical bandgap and Burstein-Moss shift

The optical properties of the MBE-grown samples were evaluated with spectroscopic ellipsometry measurements. Where possible, transmittance and reflectance measurements were also performed, subject to the type of substrate used to grow each sample. The optical bandgap of those samples was determined using the Cody expression for the absorption coefficient, as described in Chapter 4. The experimental and modelled ellipsometric parameters of a Zn_3N_2 sample grown on glass are shown in **Figure 5.19a**. The optical properties obtained from the ellipsometry model are shown in **Figure 5.19b**. The grown films had an absorption onset at approximately 1.25 eV and a refractive index of 2.4-2.7.

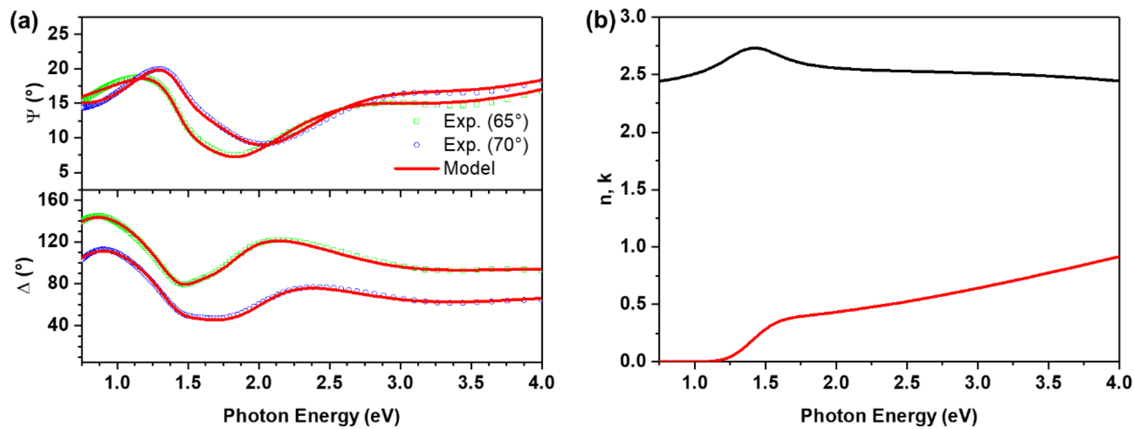

Figure 5.19: (a) Experimental and modelled ellipsometric parameters for a Zn_3N_2 sample grown on an unheated glass substrate. (b) Refractive index *n* (black) and extinction coefficient *k* (red) obtained for Zn_3N_2 from ellipsometry models.

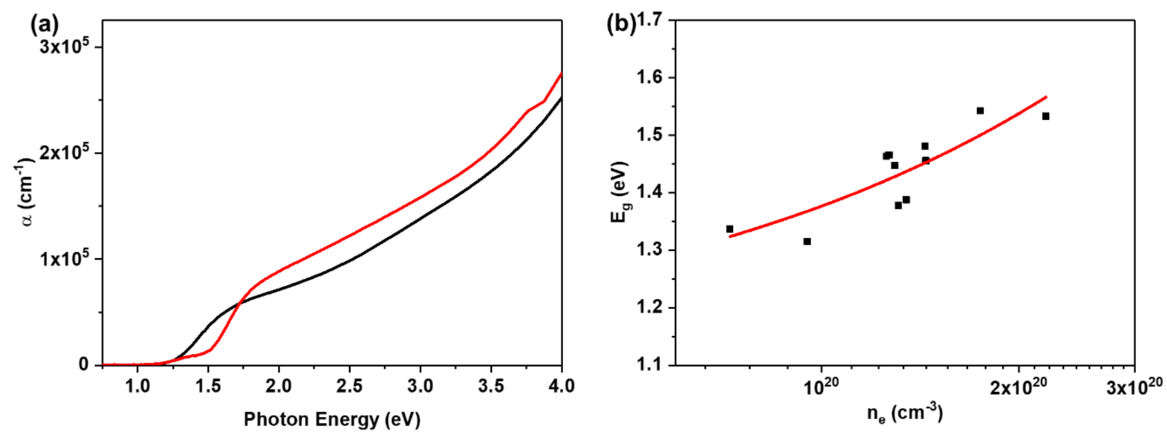

Figure 5.20: (a) Absorption coefficient α of MBE-grown samples in which the optical bandgap has shifted. These spectra were calculated from optical transmittance and reflectance measurements. (b) Optical bandgap of several MBE samples plotted against their carrier density measured from Hall effect measurements. The red curve shows a fit of the data to equation (5.6).

In very broad terms, the optical properties of the MBE-grown samples were comparable to the sputtered samples. However, the measured optical bandgap varied more significantly in the MBE samples than in the sputtered samples. The absorption coefficient spectra shown in **Figure 5.20a** demonstrate the range in which the optical bandgap varied in different MBE-grown Zn_3N_2 samples. The largest optical bandgap was observed in samples grown on a heated substrate. Because the wide bandgap sample shown in **Figure 5.20a** was grown using a two-step process (i.e. growth with a buffer layer), two onsets of absorption are observed: one at ~1.25 eV, and one at ~1.5 eV. The first absorption onset is at the same photon energy as the sample grown on an unheated substrate, indicating that it is caused by the buffer layer, whereas the second absorption onset is caused by the film grown on the buffer layer.

Photoluminescence was not observed in any of the MBE-grown samples. This is attributed to the high doping level in these samples, which was approximately one order of magnitude higher than in samples deposited by sputtering. The high defect density results in a high density of non-radiative recombination states, which prevent carrier recombination through radiative transitions observed in photoluminescence. As these Zn_3N_2 samples were heavily doped, the effect of the Burstein-Moss effect on the optical bandgap was investigated. In heavily doped n-type semiconductors, partial filling of the conduction band can result in a shift of the optical bandgap called the Burstein-Moss shift. The Burstein-Moss shift ΔE_g can be described in the following form, based on calculations of the Fermi level for parabolic bands in a semiconductor:

$$E_g = E_0 + \Delta E_g \tag{5.4}$$

$$\Delta E_g = \frac{h^2}{2}\left(\frac{1}{m_e} + \frac{1}{m_h}\right)\left(\frac{3n_e}{\pi}\right)^{\frac{2}{3}} \tag{5.5}$$

where E_g is the experimental optical bandgap of a semiconductor, E_0 is the intrinsic bandgap of the semiconductor, and m_e and m_h are the effective masses for electrons and holes respectively.[3,30,31] It is seen in equation (5.5) that the Burstein-Moss shift is characterised by a relationship of $\Delta E_g \sim n_e^{2/3}$.

The optical bandgaps of several MBE samples grown in this study are shown against their charge carrier densities in **Figure 5.20b**. The data were fitted to the following equation:

$$E_g = E_0 + A n_e^{\frac{2}{3}} \tag{5.6}$$

where A is a proportionality constant. The fit to equation (5.6) is shown by the solid line in in **Figure 5.20b**. Both E_0 and A were fitted with a least squares analysis, resulting in the following expression for the Burstein-Moss shift in Zn_3N_2:

$$E_g = 1.10 + 1.27 \times 10^{-14} n_e^{\frac{2}{3}} \tag{5.7}$$

As a result, the Burstein-Moss analysis suggests an intrinsic bandgap of 1.10 ± 0.07 eV for Zn_3N_2. This is demonstrated graphically in **Figure 5.21** which shows the optical bandgap of MBE samples plotted against $n_e^{2/3}$. In this graph, the fit to equation (5.6) is a straight

line with an intercept at 1.10 eV. It is noted that the values obtained here for E_0 and A are comparable these reported by Suda *et al.* for polycrystalline Zn_3N_2 grown by MBE.[3]

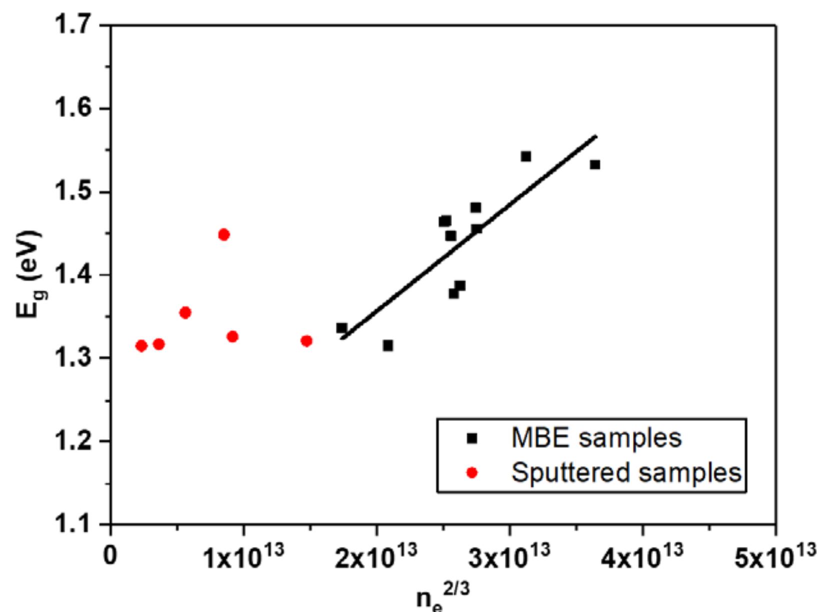

Figure 5.21: Bandgap E_g of MBE samples plotted against $n_e^{2/3}$. The straight-line fit demonstrates the effect of the Burstein-Moss shift.

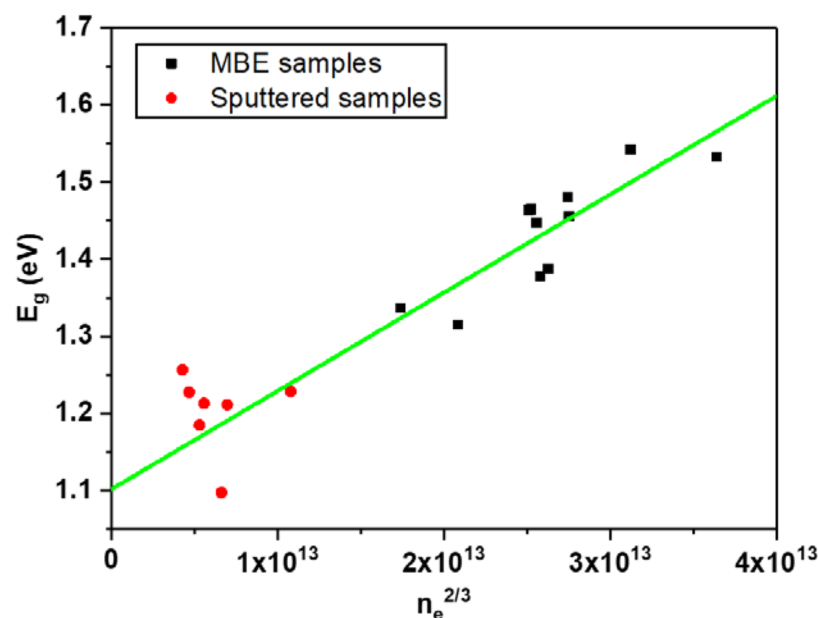

Figure 5.22: Burstein-Moss shift in sputtered and MBE-grown samples after correcting for the effect of thermal annealing on the optical bandgap.

It is worth noting that the trend of the Burstein-Moss shift was not maintained in the sputtered samples, as shown in **Figure 5.21**. Instead, the optical bandgap seems to settle at around 1.30 eV for the samples with lower carrier density. This is likely a result of other factors affecting the measurements of the optical and electrical properties of these

samples. One such parameter is the density of the sputtered films affecting the effective carrier density, as described by equation (5.3). The second parameter is an effect of thermal annealing on the optical bandgap. Wen *et al.* reported a red-shift of the optical bandgap as a result of ex-situ thermal annealing in O_2 and air.[32] The same effect was observed for the samples examined in this study. The Hall effect measurements for the sputtered samples included a thermal annealing step to anneal the In contacts into the films. However, the values for the optical bandgap shown in **Figure 5.21** are based on optical measurements performed before annealing. If the data are corrected for the redshift observed after annealing, the sputtered samples are closer to the trend of the BM shift observed in the MBE samples. This is shown in **Figure 5.22**. The values of the carrier density were also adjusted for the filling factor based on equation (5.3) using the value of $\pi/4$ as an approximation of close-packed spheres. The reasons behind the shift of the bandgap in the annealed samples are discussed further in Chapter 7 which examines the effect of ex-situ thermal annealing on several properties of the Zn_3N_2 films.

5.7. Summary

An MBE process to deposit Zn_3N_2 films, and the properties of the grown films were discussed in this chapter. Initial experiments with depositing metallic Zn on Si and glass indicated a poor sticking coefficient of Zn on these surfaces. By introducing active nitrogen species with a nitrogen plasma source, Zn_3N_2 films were easily obtained on unheated glass substrates. However, it was found that growth on heated substrates required some form of substrate preparation, otherwise the growth process was terminated at temperatures as low as 150 °C. This was attributed to the desorption of Zn from a hot surface. Two approaches were investigated to enable growth on heated substrates: a two-step growth and a thermal treatment of the substrates. Both methods enabled growth at high temperatures, indicating that surface preparation is crucial for the initiation of Zn_3N_2 growth due to a tendency of Zn to desorb at relatively low growth temperatures. Furthermore, a surplus of Zn is likely beneficial for the same reason.

The grown Zn_3N_2 films were polycrystalline in structure and became more (400) oriented when grown on crystalline substrates at high substrate temperatures. X-ray Reflectivity measurements showed that the MBE-grown films were more densely packed than the sputtered Zn_3N_2 samples. The MBE-grown samples were unintentionally doped in the order of 10^{20} cm^{-3} and had the highest mobility observed in this study, which was in the

order of 100 cm^2 V^{-1} s^{-1}. The doping levels and mobility values seen here are comparable to those reported in other studies of MBE-grown Zn_3N_2 samples. In terms of optical properties, the MBE-grown samples behaved similarly to the sputtered samples. However, because of the very high doping levels, a Burstein-Moss shift was observed which was consistent with samples grown by sputtering. The trend of the Burstein-Moss shift suggests an intrinsic bandgap of ~1.10 eV for Zn_3N_2, which is further evidence for the narrow bandgap of this material.

5.8. Bibliography

1 T. Oshima and S. Fujita, Japanese Journal of Applied Physics **45,** 8653 (2006).

2 W. Peng, T. Tiedje, H. Alimohammadi, V. Bahrami-Yekta, M. Masnadi-Shirazi, and W. Cong, Semiconductor Science and Technology **31,** 10LT01 (2016).

3 T. Suda and K. Kakishita, Journal of Applied Physics **99,** 076101 (2006).

4 A. Fotkatzikis, M. A. Pinault, and A. Freundlich, Applied Physics Letters **85,** 2478 (2004).

5 V. A. Grant, R. P. Campion, C. T. Foxon, W. Lu, S. Chao, and E. C. Larkins, Semiconductor Science and Technology **22,** 15 (2007).

6 R. P. Vaudo, Z. Yu, J. W. Cook, and J. F. Schetzina, Optics Letters **18,** 1843 (1993).

7 Y. Cordier, B. Damilano, P. Aing, C. Chaix, F. Linez, F. Tuomisto, P. Vennéguès, E. Frayssinet, D. Lefebvre, M. Portail, and M. Nemoz, Journal of Crystal Growth **433,** 165 (2016).

8 S. Gozu, T. Mozume, H. Kuwatsuka, and H. Ishikawa, Nanoscale Research Letters **7,** 620 (2012).

9 F. G. Celii, Y. C. Kao, E. A. B. III, W. M. Duncan, and T. S. Moise, Journal of Vacuum Science & Technology B: Microelectronics and Nanometer Structures Processing, Measurement, and Phenomena **11,** 1018 (1993).

10 N. Chand, T. D. Harris, S. N. G. Chu, E. A. Fitzgerald, J. Lopata, M. Schnoes, and N. K. Dutta, Journal of Crystal Growth **126,** 530 (1993).

11 J. Greenbank and B. Argent, Transactions of the Faraday Society **61,** 655 (1965).

12 J. D. McKinley and J. E. Vance, The Journal of Chemical Physics **22,** 1120 (1954).

13 S. R. Logan, Journal of Chemical Education **59,** 279 (1982).

14 M. Coke, Thesis, UCL (University College London), 2017.

15 N. Feldberg, J. D. Aldous, W. M. Linhart, L. J. Phillips, K. Durose, P. A. Stampe, R. J. Kennedy, D. O. Scanlon, G. Vardar, R. L. Field, T. Y. Jen, R. S. Goldman, T. D. Veal, and S. M. Durbin, Applied Physics Letters **103,** 042109 (2013).

16 N. Feldberg, J. D. Aldous, P. A. Stampe, R. J. Kennedy, T. D. Veal, and S. M. Durbin, Journal of Electronic Materials **43,** 884 (2014).

17 V. Umansky and M. Heiblum, in *Molecular Beam Epitaxy*, edited by M. Henini (Elsevier, Oxford, 2013), p. 121.

18 M. Bum Ki and I. Hiroshi, Japanese Journal of Applied Physics **33,** 1472 (1994).

19 H. Sitter, G. J. Glanner, and M. A. Herman, Vacuum **46,** 69 (1995).

20 B. Qi, B. Agnarsson, K. Jonsson, S. Olafsson, and H. P. Gislason, Journal of Physics: Conference Series **100,** 042020 (2008).

[21] K. Akihiko, H. Hiroyuki, and K. Katsumi, Japanese Journal of Applied Physics **33,** 688 (1994).

[22] Y. Yao, T. Sekiguchi, T. Ohgaki, Y. Adachi, and N. Ohashi, Journal of the Ceramic Society of Japan **120,** 513 (2012).

[23] J. R. Lang and J. S. Speck, Journal of Crystal Growth **346,** 50 (2012).

[24] L. Morresi, in *Silicon Based Thin Film Solar Cells*, edited by R. Murri (Bentham Science Publishers, 2013), p. 81.

[25] R. Garcia, A. C. Thomas, and F. A. Ponce, Journal of Crystal Growth **310,** 3131 (2008).

[26] P. N. Dever, M. H. Samir, T. Li-Wei, L. Yuan-Ting, L. Chen-Yu, and S. Hye-Won, Applied Physics Express **7,** 115502 (2014).

[27] M. Kwoka, B. Lyson-Sypien, A. Kulis, M. Maslyk, M. Borysiewicz, E. Kaminska, and J. Szuber, Materials **11,** 131 (2018).

[28] M. Y. Kharitonov and K. B. Efetov, Physical Review B **77,** 045116 (2008).

[29] A. Gondorf, M. Geller, J. Weißbon, A. Lorke, M. Inhester, A. Prodi-Schwab, and D. Adam, Physical Review B **83,** 212201 (2011).

[30] P. K. Chakraborty, G. C. Datta, and K. P. Ghatak, Physica B: Condensed Matter **339,** 198 (2003).

[31] Y. Kumagai, K. Harada, H. Akamatsu, K. Matsuzaki, and F. Oba, Physical Review Applied **8,** 014015 (2017).

[32] T. Wen, M. Gautam, A. M. Soleimanpour, and A. H. Jayatissa, Materials Science in Semiconductor Processing **16,** 318 (2013).

Chapter 6: Aluminium Zinc Nitride Grown by Sputtering

6.1. Bandgap tuning in Zinc Nitride materials

The structural, optical, and electrical properties of Zn_3N_2 thin films grown by sputtering and MBE were investigated in the two previous chapters, and the results between the two techniques have been consistent. In semiconductor electronics, the ability to tune the bandgap of the deposited layers is useful (e.g. for heterostructures used in lasers, LEDs, or heterojunction solar cells).

Bandgap engineering in semiconductors is typically achieved with two main approaches: the effects of quantum confinement (i.e. in quantum dots or quantum well structures), and semiconductor alloys. In semiconductor alloys the lattice size, bandgap, and refractive index of the material are all affected. Taylor *et al.* observed a shift in the photoluminescence of Zn_3N_2 nanoparticles of different sizes, which was attributed to the effects of quantum confinement.[1] In terms of semiconductor alloys, the related II-IV-V alloys Zn(Ge, Sn)N_2, have a bandgap tuneable in the range of 2.0-3.1 eV.[2-5] These materials have attracted interest for solar energy conversion applications as alternatives to III-V semiconductors. However, material systems related to Zn_3N_2 have not been investigated. For example, alloying Zn_3N_2 with a wide-bandgap III-V material, such as AlN, could allow tuning of the bandgap energy over a wide range at relatively low fractions of alloying. Another reason to investigate Zn_3N_2-based semiconductor alloys is that they may provide insight on the fundamental properties of Zn_3N_2 and assist in better understanding some of the persisting issues with Zn_3N_2, such as the high doping levels seen in samples grown without intentional doping.

In this study, we have investigated the formation of an AlZnN alloy and discuss the structural, optical, and electrical properties of such films. The approach used here to deposit an AlZnN alloy is to reactively sputter from an AlZn target. When sputtering from an alloy target, the two metallic species will have different sputtering yields, depending on the process conditions and the composition on the surface of the target. When nitrogen gas was used as the reactive gas, the sputter process resulted in the deposition of AlZnN films. The

process of sputtering from an alloy target and the specific conditions used in these experiments are discussed in more detail in **§3.1.1**.

Samples with varying Al content were deposited by altering the conditions on the surface of the target. The deposited films were characterised by spectroscopic ellipsometry, X-ray Diffraction and Hall Effect measurements. The crystal structure, and optical and electrical properties of the alloyed films were compared to Zn_3N_2 samples deposited under similar conditions. At the time of writing, there has been no experimental study of a II-III-V semiconductor alloy, therefore the details of determining the fraction of each component in the alloy films, and how the analysis differs from III-III'-V alloys are initially discussed.

6.2. Compositional analysis of a II-III-V alloy

Estimating the composition of Al in the deposited films was necessary for any of the measured properties to be related to Al content. This was approached with quantitative EDS analysis. It was found experimentally that the fraction of Al in the sputtered films could be altered in consecutive samples by sputtering at a nitrogen flow of 45 sccm (standard cubic centimetres per minute). This is shown in **Figure 6.1** for 4 consecutive samples. In further depositions, the process became unstable and resulted in arcing, likely due to excessive formation of AlZnN on the target. Conditioning the target by sputtering in argon plasma for 30 minutes was sufficient to recover the Al fraction in the deposited films to its initial value. This behaviour can be explained by the partial formation of compounds (AlN and ZnN) at the surface of the target. Whichever metal species or compound has a lower sputter yield (e.g. Al/AlN) will gradually increase in concentration at the surface of the target. The deposition rate of other species (e.g. Zn/ZnN) then becomes limited by the rate of exposure of new atoms to the plasma. Using this method, a range of AlZnN samples with different compositions were deposited and studied.

The spectra measured in four AlZnN samples (*AZN-#*) are shown in **Figure 6.2** and compared to that of a Zn_3N_2 sample (ZN) deposited under similar conditions. The results of the EDS analysis corresponding to these measurements are listed in **Table 6.1**. The elements detected in the films were C, N, O, Al, and Zn. Carbon is a known surface contaminant and will not be discussed further. It is noted that the intensity of the oxygen peak and as a result the calculated oxygen content varied in different samples. The oxygen observed in the measurements has several possible sources, such as:

a) surface oxidation,

b) the glass substrate, and
c) unintentional oxygen doping during deposition.

Unintentional oxygen doping should be relatively insignificant and at similar levels for all samples, as they were deposited in the same chamber and under similar conditions. Instead, the fluctuations in the measured oxygen signal are attributed to surface oxidation. Furthermore, because the samples were relatively thin, any contribution from the glass substrate and the surface oxide to the measured oxygen signal would be a considerable portion of the analysis volume. The Zn/Al ratio which is the primary result from the EDS measurements is unaffected by the oxidation process. This was investigated by EDS measurements on fully oxidised samples which showed the same results to those taken shortly after deposition.

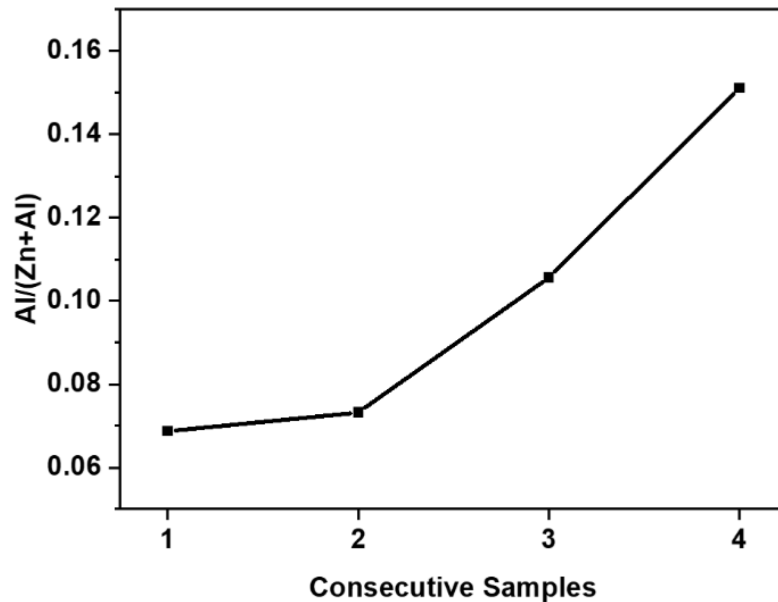

Figure 6.1: Measured Al fraction in consecutive AlZnN films deposited at a nitrogen flow rate of 45 sccm.

Using the data from the EDS analysis, the fraction of Al, x, in the film is readily calculated as:

$$x = \frac{Al\%}{Zn\% + Al\%} \tag{6.1}$$

where *Al%*, *Zn%* are atomic percentages measured by the compositional analysis. However, to correlate the measured properties in the AlZnN films to the Al content in the films, it would be more suitable to use the fraction of AlN instead. That is because any difference in the measured properties is the effect of alloying with AlN, not with Al. In III-III'-V ternary alloys, the fraction of each component in the alloy, e.g. AlN and GaN in AlGaN, is equivalent to the atomic fraction of the group III metal in the crystal structure.

For instance, x in $Al_xGa_{(1-x)}N$ would be defined using a relationship equivalent to equation (6.1). This equation can be obtained by starting out with the ratio of the two metals in the alloy and solving for x:

$$\frac{Ga\%}{Al\%} = \frac{(1-x)}{x} \tag{6.2}$$

However, a different nomenclature must be used in the case of a II-III-V alloy, to maintain the stoichiometry of both II-V and III-V compounds at opposite ends of the alloy. As a result, to express the fraction of AlN in the AlZnN films, a II-III-V alloy of the following form was devised: $Al_{2x}Zn_{3(1-x)}N_2$. From this expression for AlZnN alloys, the molar fraction of AlN, x, is calculated from experimentally determined Al and Zn atomic percentages as:

$$x = \frac{Al\%}{\frac{2}{3}Zn\% + Al\%} \tag{6.3}$$

starting, as for III-III'-V alloys, from the initial expression for the ratio of Zn to Al:

$$\frac{Zn\%}{Al\%} = \frac{3(1-x)}{2x} \tag{6.4}$$

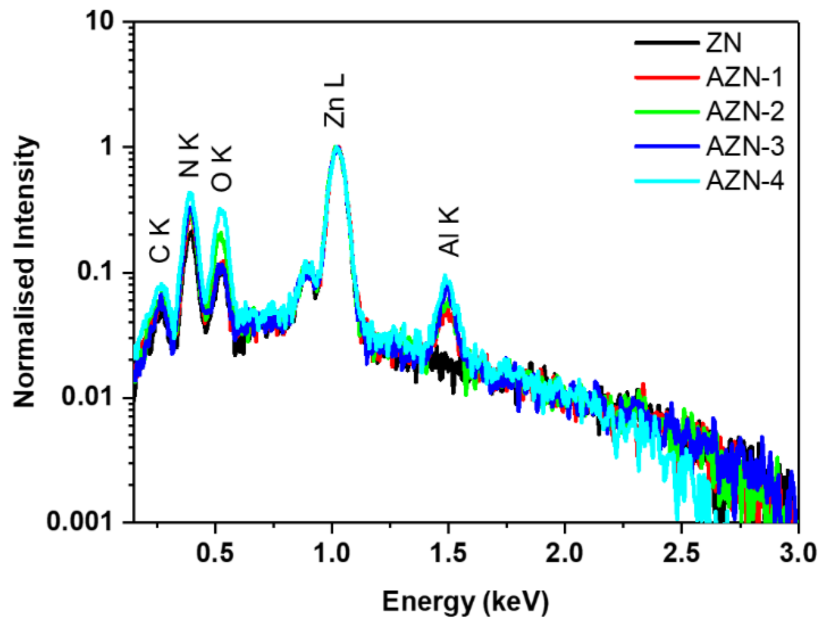

Figure 6.2: EDS measurements of a Zn_3N_2 sample and several AlZnN samples.

The AlN fraction was calculated from the EDS results using equation (6.4) and is listed in **Table 6.1**. From this analysis, we conclude that a maximum AlN fraction of x = 0.2107 was obtained in sample AZN-4. In contrast, using the atomic fraction of Al as in (6.1) yields a maximum fraction of x = 0.1511. As a result, using these different expressions in the analysis of, for instance, the dependence of the bandgap on the AlN fraction would result in different results for the slope of the curve. A comparison between equations (6.1)

and (6.4) regarding the dependence of the measured optical properties on *x* is discussed in **§6.4**.

Table 6.1: Compositional data for a Zn_3N_2 sample and different AlZnN samples as calculated by quantitative analysis of the EDS spectra.

Sample	N (at. %)	O (at. %)	Al (at. %)	Zn (at. %)	AlN fraction *x*
ZN	28	17	0	51	0.00
AZN-1	39	9	3	47	0.09
AZN-2	37	16	3	42	0.11
AZN-3	42	7	5	43	0.15
AZN-4	40	22	5	31	0.21

6.3. Crystal structure and morphology

The physical structure of the AlZnN films was investigated by GIXRD and SEM. The GIXRD scans and SEM images of the AlZnN samples are shown in **Figure 6.3**. Two diffraction peaks were observed in the diffraction pattern of the Zn_3N_2 sample, shown in **Figure 6.3a**. Similar diffraction peaks were also observed at relatively low AlN content for sample AZN-1. As the AlN fraction increased in samples AZN-3 and AZN-4, the films became amorphous. In terms of morphology, the surface of the samples became smoother in sample AZN-4, as shown in the SEM images in **Figure 6.3b-f**.

The two peaks observed in the diffraction pattern of the Zn_3N_2 sample correspond well with crystal planes (400) and (440) of the Zn_3N_2 structure, which are commonly observed in polycrystalline Zn_3N_2 and have also been discussed in previous chapters.[6-9] In AZN-1, the diffraction peaks were shifted to higher angles, which suggests that the crystal lattice has shrunk. For a cubic crystal structure, the lattice constant of AZN-1 is estimated as 9.59 A, compared to that of 9.76 A for Zn_3N_2. This observation suggests that Al was uniformly incorporated into the deposited films for low Al content. This calculation could not be performed for the rest of the samples as they became amorphous. The resulting amorphous structure at high levels of Al content may indicate an incompatibility between the crystal structure of Zn_3N_2 and that of AlN. Zn_3N_2 has an anti-bixbyite crystal structure (cubic) with a lattice constant of 9.76 Å. AlN can crystallise in both wurtzite (hexagonal, a = 3.11 Å, c = 4.98 Å) and zincblende (cubic, a = 4.38 Å) crystal structures.[10] As this study is based on samples that were deposited on unheated glass substrates, there is much room to improve the crystal structure by optimising the growth conditions and identifying a

suitable crystalline substrate for oriented deposition. However, due to time constraints these studies could not be performed for the present work.

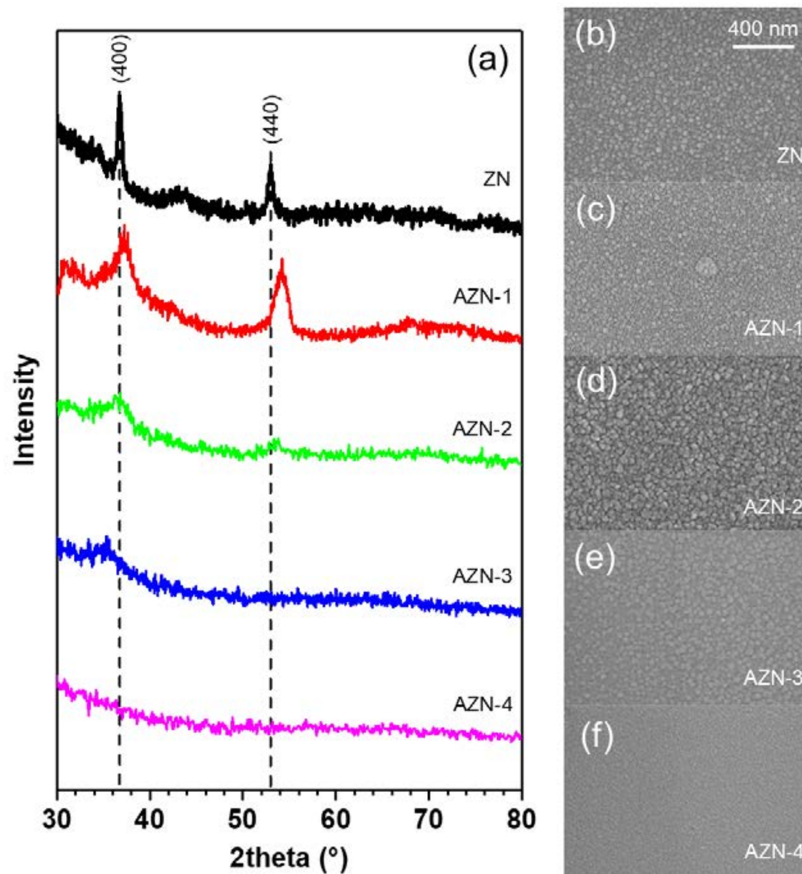

Figure 6.3: (a) XRD measurements of a Zn_3N_2 sample and different AlZnN samples. (b)-(f) SEM images of the same samples.

6.4. Absorption coefficient and refractive index

The effects of alloying were more clearly observed in the optical properties of the samples. Optical transmittance measurements initially indicated that the absorption onset of the AlZnN samples had shifted to higher energies, as shown in **Figure 6.4**. To quantify this shift more precisely, Ellipsometry measurements of the samples were modelled using a three-layer optical model which consisted of (a) a surface oxide layer, (b) the bulk of the AlZnN sample, and (c) the glass substrate. By modelling the surface oxide layer, any effect it would otherwise have on the calculated optical properties of the material is minimised. The properties of the semiconductor layers were modelled with the WVASE software using an oscillator based on a Herzinger-Johs parameterise function.[11] The experimental and modelled ellipsometric parameters for AZN-1 at two different angles of incidence are shown in **Figure 6.5**. The first few minima and maxima of optical interference were

observed in the ellipsometric parameters, which carry information about the optical properties and thickness of the films. The mean squared error (MSE) for the model shown in **Figure 6.5** is 17.25. Similar quality fits (MSE in the range of 8-20) were achieved for all samples by fitting the properties of the semiconductor layers.

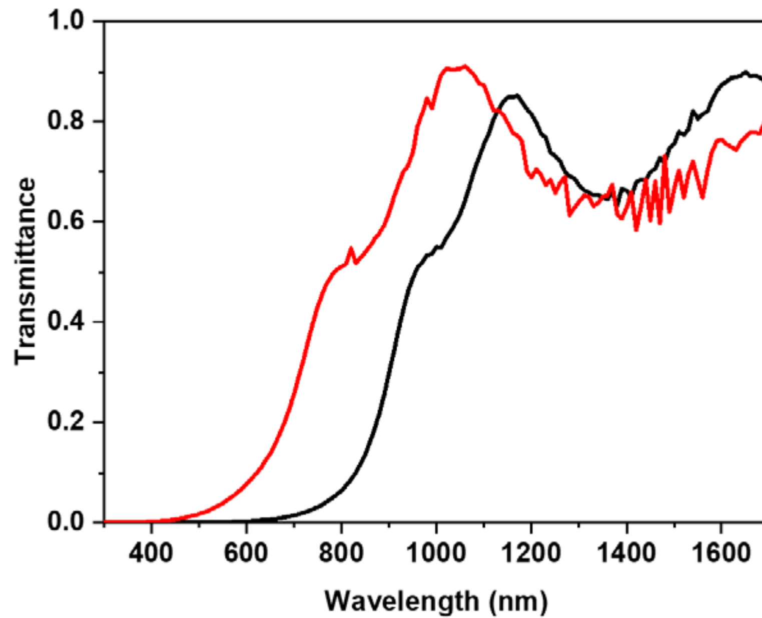

Figure 6.4: Transmittance measurements of a Zn_3N_2 (black) and an AlZnN (red) sample.

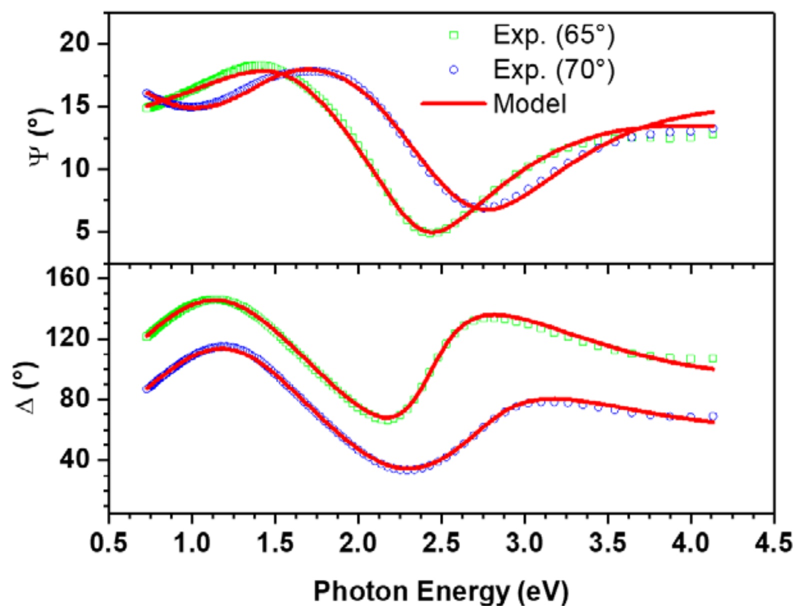

Figure 6.5: Experimental (points) and modelled (solid lines) ellipsometric parameters Ψ and Δ for AZN-1.

The refractive index, extinction coefficient and thickness of the AlZnN samples were determined from the ellipsometry models that were developed. The extracted refractive index and extinction coefficient for samples AZN-1 to AZN-4 are shown in **Figure 6.5b**.

The results of the ellipsometry models were consistent with the initial observations in optical measurements. For samples AZN-1 to AZN-4, the absorption onset shifted to increasingly higher energies. Similarly, the refractive index decreased, and the hump commonly observed in energies near the bandgap shifted to higher energies. Combined with the shift observed in the XRD pattern, these results further indicate that the incorporation of Al into the alloy films was uniform. To estimate the bandgap of the AlZnN samples, the absorption coefficient (α) of each sample was calculated from the extinction coefficient (k) as $a = 4\pi k/\lambda$, where λ is the wavelength of incident light. The bandgap was assigned at the wavelength at which the absorption coefficient reached 10^4 cm^{-1}, as is common practice in direct bandgap semiconductors.

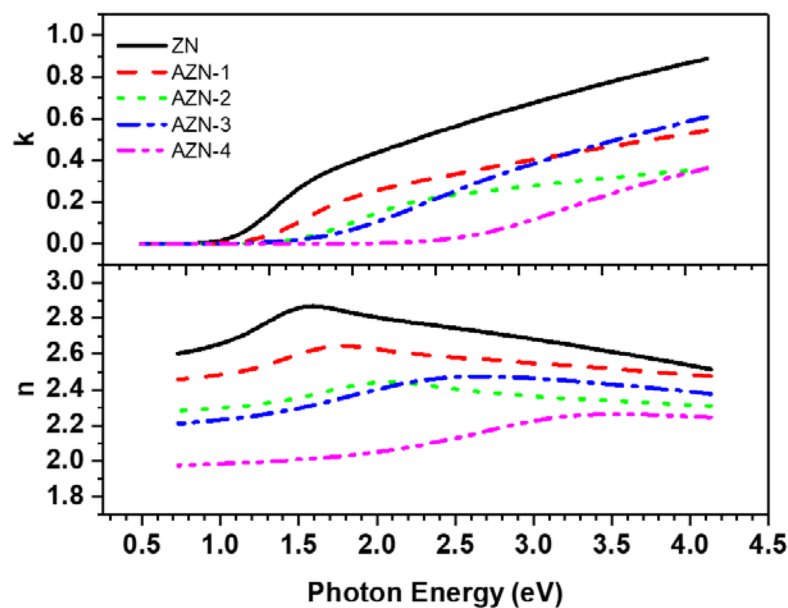

Figure 6.6: Extinction coefficient *k* and refractive index *n* of AlZnN films as modelled from ellipsometry measurements.

The bandgap and refractive index of several AlZnN samples calculated from analysis of the ellipsometry models were correlated with the AlN fraction in the films, as shown in **Figure 6.7**. A trend of the optical properties of the AlZnN samples in the direction of AlN was observed with increasing AlN fraction. Taking into consideration the optical properties of AlN (E_g = 6.05 eV and n = 1.7 for amorphous AlN[12,13]), the bandgap and refractive index were fitted to a Vegard's law type function.[5] For the bandgap of ternary semiconductor alloys, Vegard's law is commonly written in the following form:

$$E_g(x) = E_{g,ZnN}(1-x) + E_{g,AlN}x - bx(1-x) \tag{6.5}$$

where b is a material specific bowing parameter. The dashed lines in **Figure 6.7** show fits based on Vegard's law. The bowing parameter for the available data was fitted as b = -1.97

± 1.16 eV. The bandgap of Zn_3N_2 was also fitted, because of the uncertainty of its value in published literature. The fitted value for the bandgap of Zn_3N_2 was $E_{g,ZnN} = 1.13 \pm 0.16$ eV. This is a similar value to that obtained in Chapter 5 (E_g = 1.10 eV) by fitting the Burstein-Moss shift in MBE-grown samples for a parabolic band approximation. The proximity of these values for the bandgap is promising, because they were determined independently from each other, and hints at an intrinsic property of Zn_3N_2.

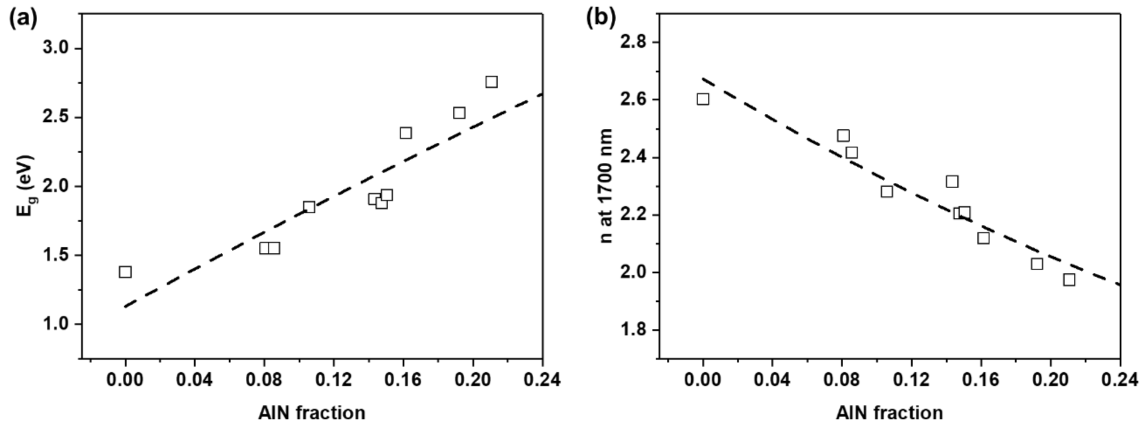

Figure 6.7: (a) Optical bandgap E_g and (b) refractive index n of different AlZnN films. The dashed lines show fits obtained using Vegard's law.

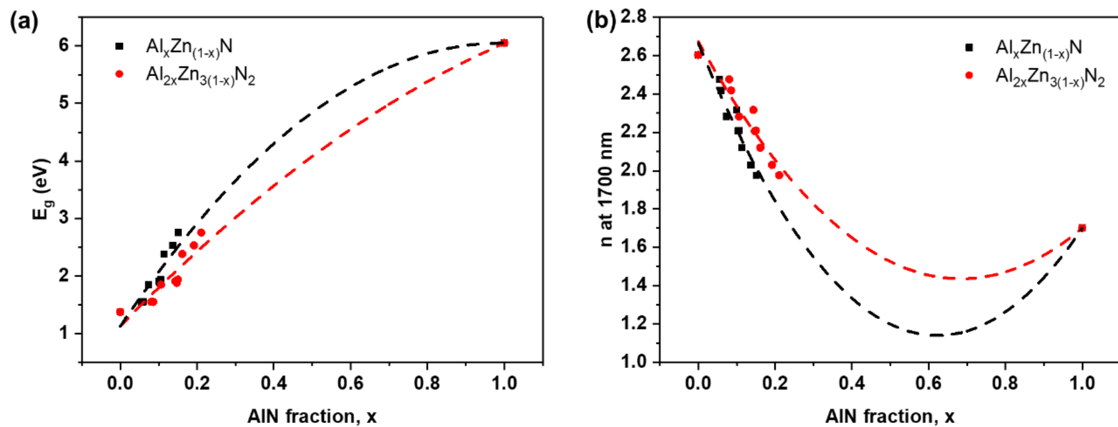

Figure 6.8: Comparison of different approaches to calculating the AlN fraction in the AlZnN films, and how it affects the apparent bowing of (a) the bandgap, and (b) the refractive index.

Based on the observed tuning of the optical properties of these alloys, AlZnN is suggested as a candidate materials system for use in Zn_3N_2-based heterostructures. The bandgap and refractive index extrapolated for higher AlN content alloys based on the fits obtained with Vegard's law are shown in **Figure 6.8**. However, because the Vegard's law analysis is based on fitting data for up to ~20% AlN, the calculated bowing parameters should be considered with caution. The same figure shows the difference in the apparent bowing of the optical properties of AlZnN when calculating the AlN fraction with equation

(6.1) used for conventional III-III'-V alloys and equation (6.4) suggested here for II-III-V semiconductor alloys. When equation (6.1) is used, the apparent bowing is greater, because the calculated values for x are overall lower. Higher AlN alloys should be investigated as there may be other effects affecting the properties of AlZnN alloys at higher Al content, such as transitions between direct/indirect bandgaps seen in other semiconductor alloys.

6.5. Charge transport properties

Since Zn_3N_2 is often a degenerately doped n-type semiconductor[7,14-18], the effects of the alloying on the electrical properties of the material were investigated by Hall Effect measurements. The resistivity and carrier density of several AlZnN samples are shown as function of AlN fraction in **Figure 6.9**. It is worth noting that all measured samples displayed n-type conductivity. The Zn_3N_2 sample had a resistivity in the order of 10^{-2} Ω cm, a carrier density in the order of 10^{19} cm^{-3}, and a mobility of 8.3 cm^2 V^{-1} s^{-1}. It was immediately observed that the AlZnN samples had significantly higher resistivity than the Zn_3N_2 samples. The resistivity measured in the AlZnN samples was in the order of 10-50 Ω cm and increased with increasing Al content. Similarly, the measured carrier density for the AlZnN samples was in the order of 10^{16}-10^{17} cm^{-3} and decreased with increasing Al content. These results further indicate that the addition of Al into this material had a major effect on its electronic structure. The carrier mobility in the AlZnN films, shown in **Figure 6.10**, did not show a clear dependence on the AlN fraction, but was on average lower than the Zn_3N_2 sample. The overall decrease in carrier mobility is likely a result of the amorphous structure obtained for films with a high Al content.

The observed increase in resistivity by 2-3 orders of magnitude corresponds well with the proportional decrease in the carrier density. A similar increase in resistivity is observed in Al-rich AlGaN alloys.[19] It should be noted that the origin of the high unintentional doping levels in Zn_3N_2 samples is not yet fully understood in the literature. However, both nitrogen vacancies and oxygen contamination are thought to be potential causes.[20,21] It is possible that the nitrogen vacancies responsible for the n-type doping in the structure of Zn_3N_2 are less likely to be formed when Al is present in the structure. Unfortunately, such changes in vacancy concentration could not be assessed for this work. Another possible explanation is that Al replaces O contaminants in the deposited films. If that were the case, the decrease in carrier density could be attributed to a decrease in the oxygen contamination. However, because there are multiple possible sources for the oxygen

observed in the EDS scans (surface oxidation and the glass substrate), the EDS analysis cannot be used to indicate the oxygen concentration in the bulk of the AlZnN films. Yet another likely mechanism is that of an increase in the donor binding energy in the AlZnN samples, which would result in fewer carriers excited to the conduction band at room temperature. A similar effect is known for oxygen-doped AlGaN alloys with increasing Al content.[22]

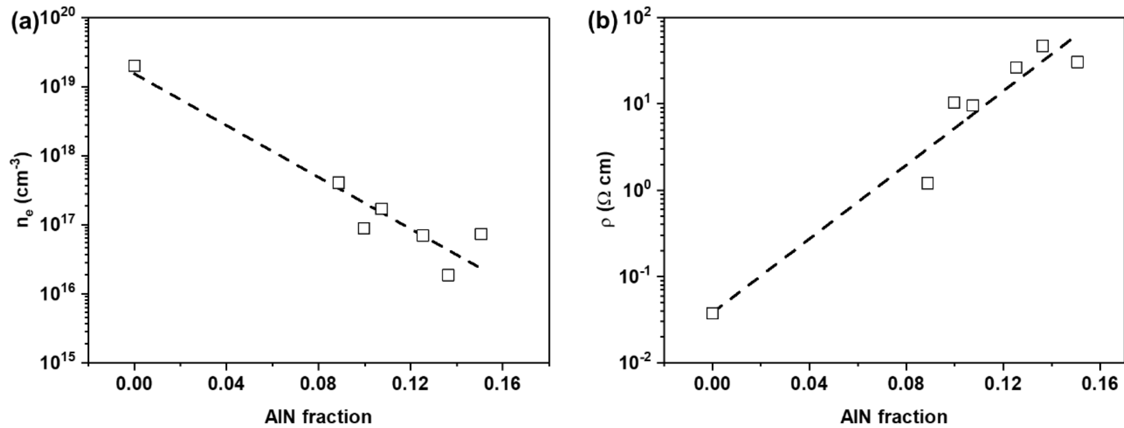

Figure 6.9: (a) Resistivity ρ and (b) carrier density n_e of different AlZnN films. The dashed lines are meant as a guide to the eye.

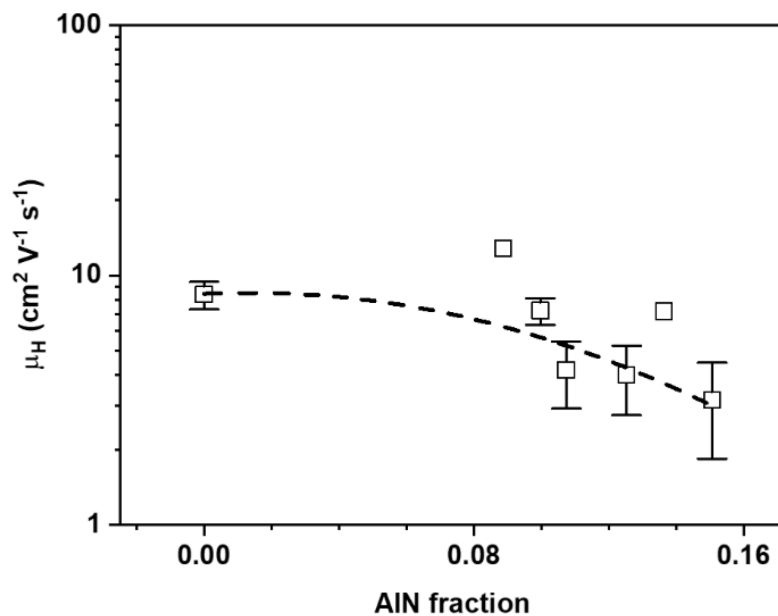

Figure 6.10: Carrier mobility μ_H of AlZnN samples plotted against the AlN fraction. The dashed line is meant as a guide to the eye. Where not shown, the error bars are smaller than the points on the graph.

Although the data presented here is insufficient to reach a definitive conclusion on the cause of the decreased carrier density, we suggest that studying AlZnN alloys further will provide insight on the origin of the donor defects in both Zn_3N_2 and AlZnN samples. For instance, the effect of oxygen contamination within the films could be investigated by

precisely determining the oxygen content in AlZnN samples, which would indicate whether Al replaces O in the structure. Furthermore, the crystal structure of the alloy could be further studied (in more crystalline samples) to determine what sites are occupied by Al. Computational studies could also provide insight on this topic. Furthermore, p-type dopants for Zn_3N_2 materials will be easier to investigate by performing doping studies in AlZnN samples than in degenerately doped Zn_3N_2, to enable p-n junctions based on Zn_3N_2 materials to be fabricated. Therefore, although a conclusion could not be reached here, the observed decrease in carrier concentration is an interesting effect that requires further investigation.

6.6. Summary

The formation of an AlZnN alloy by reactive sputtering was investigated in this chapter. The AlZnN films were described as $Al_{2x}Zn_{3(x-1)}N_2$ with a maximum AlN fraction of $x = 0.2107$ for the samples studied here. The alloy films adopted the crystal structure of Zn_3N_2 at low Al content but became amorphous at higher Al content. Analysis of optical measurements showed that the deposited films were semiconductor alloys with the intermediate properties of Zn_3N_2 and AlN. A maximum bandgap of 2.76 eV was measured for the sample with the highest Al content. The successful tuning of the optical properties in these alloys indicates that AlZnN is a promising candidate for use in heterostructures for semiconductor devices based on Zn_3N_2. Furthermore, based on the trend of the optical bandgap with AlN content, an intrinsic bandgap of 1.13 ± 0.16 eV was estimated for Zn_3N_2.

The electrical properties of the AlZnN films changed drastically, reaching carrier concentrations as low as 10^{16}-10^{17} cm^{-3}. Although a conclusion could not be reached for the reason behind this decrease, it is an interesting observation that warrants further investigation. Additionally, AlZnN samples are likely a good starting point to investigate p-type dopants in Zn_3N_2-related materials, because of their relatively low carrier concentration compared to degenerately doped Zn_3N_2.

6.7. Bibliography

1 P. N. Taylor, M. A. Schreuder, T. M. Smeeton, A. J. D. Grundy, J. A. R. Dimmock, S. E. Hooper, J. Heffernan, and M. Kauer, Journal of Materials Chemistry C **2,** 4379 (2014).

[2] N. Feldberg, J. D. Aldous, W. M. Linhart, L. J. Phillips, K. Durose, P. A. Stampe, R. J. Kennedy, D. O. Scanlon, G. Vardar, R. L. Field, T. Y. Jen, R. S. Goldman, T. D. Veal, and S. M. Durbin, Applied Physics Letters **103,** 042109 (2013).

[3] L. Lahourcade, N. C. Coronel, K. T. Delaney, S. K. Shukla, N. A. Spaldin, and H. A. Atwater, Advanced Materials **25,** 2562 (2013).

[4] S. Chen, P. Narang, H. A. Atwater, and L.-W. Wang, Advanced Materials **26,** 311 (2014).

[5] P. Narang, S. Chen, N. C. Coronel, S. Gul, J. Yano, L.-W. Wang, N. S. Lewis, and H. A. Atwater, Advanced Materials **26,** 1235 (2014).

[6] T. Suda and K. Kakishita, Journal of Applied Physics **99,** 076101 (2006).

[7] M. Futsuhara, K. Yoshioka, and O. Takai, Thin Solid Films **322,** 274 (1998).

[8] E. Maile and R. A. Fischer, Chemical Vapor Deposition **11,** 409 (2005).

[9] X. Cao, Y. Yamaguchi, Y. Ninomiya, and N. Yamada, Journal of Applied Physics **119,** 025104 (2016).

[10] F. Litimein, B. Bouhafs, Z. Dridi, and P. Ruterana, New Journal of Physics **4,** 64 (2002).

[11] B. Johs, C. M. Herzinger, J. H. Dinan, A. Cornfeld, and J. D. Benson, Thin Solid Films **313,** 137 (1998).

[12] H. Fatemeh, L. Majid Mojtahedzadeh, G. Mahmood, A. Morteza, and H. Alireza, Japanese Journal of Applied Physics **49,** 095802 (2010).

[13] A. E. Giba, P. Pigeat, S. Bruyère, T. Easwarakhanthan, F. Mücklich, and D. Horwat, Thin Solid Films **636,** 537 (2017).

[14] E. Aperathitis, V. Kambilafka, and M. Modreanu, Thin Solid Films **518,** 1036 (2009).

[15] G. Z. Xing, D. D. Wang, B. Yao, L. F. N. A. Qune, T. Yang, Q. He, J. H. Yang, and L. L. Yang, Journal of Applied Physics **108,** 083710 (2010).

[16] N. Jiang, D. G. Georgiev, T. Wen, and A. H. Jayatissa, Thin Solid Films **520,** 1698 (2012).

[17] C. G. Núñez, J. L. Pau, M. J. Hernández, M. Cervera, E. Ruiz, and J. Piqueras, Thin Solid Films **520,** 1924 (2012).

[18] T. Wen, M. Gautam, A. M. Soleimanpour, and A. H. Jayatissa, Materials Science in Semiconductor Processing **16,** 318 (2013).

[19] J. Li, K. B. Nam, J. Y. Lin, and H. X. Jiang, Applied Physics Letters **79,** 3245 (2001).

[20] Y. Kumagai, K. Harada, H. Akamatsu, K. Matsuzaki, and F. Oba, Physical Review Applied **8,** 014015 (2017).

[21] N. Jiang, J. L. Roehl, S. V. Khare, D. G. Georgiev, and A. H. Jayatissa, Thin Solid Films **564,** 331 (2014).

[22] M. D. McCluskey, N. M. Johnson, C. G. Van de Walle, D. P. Bour, M. Kneissl, and W. Walukiewicz, Physical Review Letters **80,** 4008 (1998).

Chapter 7: On thermal annealing and the stability of Zinc Nitride

7.1. Ex-situ thermal annealing of Zinc Nitride

It was shown in Chapter 4 that Zn_3N_2 films are prone to oxidation, resulting in the formation of a ZnO-based material when exposed to ambient conditions. The oxidation process results in the complete conversion of Zn_3N_2 films to an oxide material. This instability is problematic in research studies as it can cause confusion and complications when characterising these films, but more importantly provides an additional challenge for any potential applications of Zn_3N_2. For this reason, means of stabilising the deposited Zn_3N_2 films by ex-situ annealing were investigated. It was found that thermal annealing has a significant effect on the stability of Zn_3N_2 films, which prompted further investigation of the effects of thermal annealing on Zn_3N_2 films. Therefore, this chapter discusses the effects of ex-situ thermal annealing on the stability and other properties of Zn_3N_2 for both the sputtered and MBE-grown samples discussed throughout this work.

To investigate the effects of ex-situ annealing on Zn_3N_2 samples, the samples discussed here were annealed under nitrogen at temperatures of 200-400 °C. The samples were transferred to a rapid thermal annealing instrument within minutes of deposition and heated to the target temperature for 60 seconds. The stability, and the structural and optical properties of the films were then investigated as a function of the annealing temperature.

7.2. Ambient stability of annealed samples

The thermal annealing of the Zn_3N_2 samples affected their stability against oxidation, making the films less prone to oxidation. This observation is easily summed up in **Figure 7.1** which shows the optical transmittance and reflectance of as-deposited and annealed samples over a period of 12 weeks. When the Zn_3N_2 sample is fully oxidised, it becomes transparent in the visible spectrum, as shown in **Figure 7.1a**. The annealed samples display a redshift in the absorption onset which is discussed in **§7.4**. However, after annealing the films showed no signs of oxidation in a 12-week period, as shown in **Figure 7.1b**. This is an interesting effect, because the oxidation of Zn_3N_2 in ambient has been one of the difficulties in both applying and studying this material. The analysis of optical

measurements in Chapter 4 highlights the contrast between the as-deposited and oxidised layers in terms of their optical properties. However, the oxidation process itself has not been discussed. Understanding the physical process of oxidation will be useful in identifying the rate-limiting step that results in an improved stability after annealing. To investigate this mechanism, the process of oxidation is discussed next.

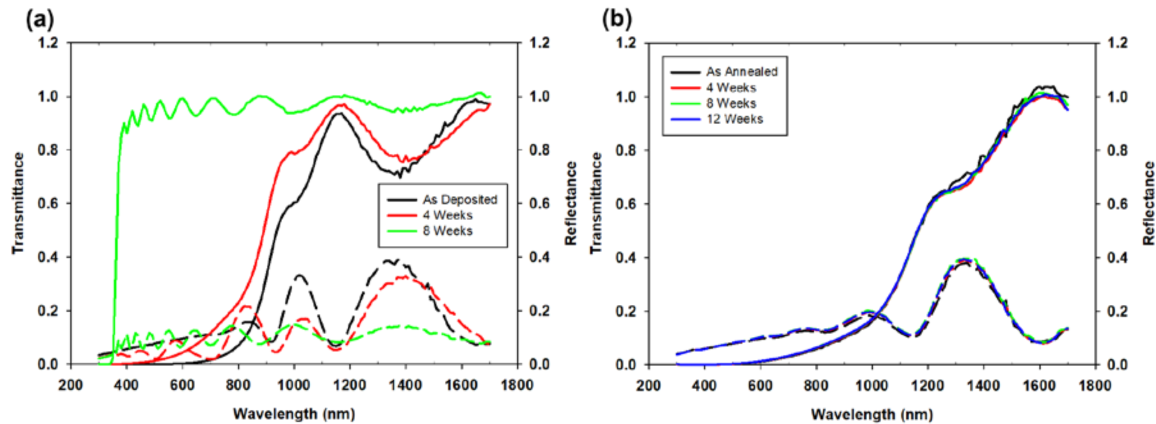

Figure 7.1: Transmittance and reflectance measurements of an (a) unannealed and (b) annealed Zn_3N_2 film over a 12-week period. The samples were stored in an ambient environment.

7.2.1. The process of oxidation

The process of oxidation likely begins with O_2 and H_2O species that are adsorbed onto the surface of Zn_3N_2. The following is a set of reactions between Zn_3N_2 and O_2 and H_2O species that describe the process of oxidation:

$$2\,Zn_3N_2 + 3\,O_2 \longrightarrow 6\,ZnO + 2\,N_2 \tag{7.1}$$

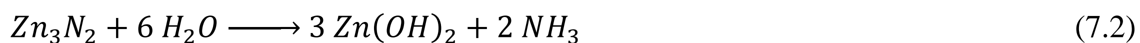

$$Zn_3N_2 + 6\,H_2O \longrightarrow 3\,Zn(OH)_2 + 2\,NH_3 \tag{7.2}$$

After a surface oxide layer has formed, further oxidation requires further exposure of the Zn_3N_2 surface to these species. As a result, the oxide layer must be permeable to O_2 and H_2O, through nanopores or a nanostructure in the oxide layer, otherwise the oxidation process would stop after the formation of a native surface oxide of a critical thickness.

The Zn_3N_2 film itself may be permeable to O_2 and H_2O, which could result in the oxide growing within the film microstructure as well as the surface of the films. Instead, if oxidation only occurred on the surface of the film, that would result in a distinct two-layer structure, in which the surface oxide layer is gradually growing in thickness, and the Zn_3N_2 layer is gradually being depleted. In the former case, the oxidation mechanism may be modelled by a single layer, the optical properties of which change over time as the average oxygen content within the crystal structure increases. In the latter case, two layers would

maintain distinct properties throughout the process of oxidation. It was determined experimentally that it is the latter oxidation process that is found in films studied here. This is demonstrated in **Figure 7.2a** which shows a cross-section Scanning Electron Microscopy (SEM) image of a sample exposed to ambient for a few days. The sample consists of two clearly distinct layers, which can be represented by the model shown in **Figure 7.2b**. For the sample shown in **Figure 7.2a**, the oxide layer is approximately 100 nm.

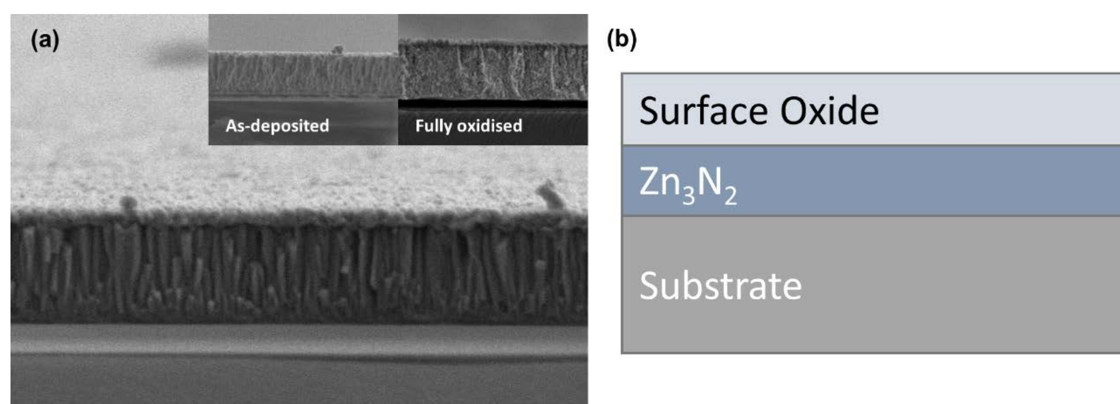

Figure 7.2: (a) Cross-section SEM image of a partially oxidised Zn_3N_2 film. Inset: Cross-section of an as-deposited and a fully oxidised sample. (b) Representation of the ellipsometry model used to describe the oxidation process.

7.2.2. Degradation study of annealed Zinc Nitride films

A degradation study was performed to investigate the effect of annealing temperature on the stability of the Zn_3N_2 films. Modelling and monitoring of the oxidation process were done by Spectroscopic Ellipsometry measurements. Experimental and modelled ellipsometric data for the as-deposited Zn_3N_2 sample are shown in **Figure 7.3**. The three-layer model shown in **Figure 7.2b** was used to model the data. This model consisted of: (a) the surface oxide layer, (b) the bulk Zn_3N_2 layer, and (c) the substrate. The rates of oxidation of as-deposited samples varied in different experiments but was in the order of 10-60 nm/day (measured as the rate of depletion of the Zn_3N_2 layer). In general, the MBE samples were more stable against oxidation compared to sputtered samples. This is likely related to the density difference between the sputtered and MBE-grown samples, which could affect how permeable the formed oxide layer is to O_2 and H_2O. For this reason, sputtered Zn_3N_2 films were used for this degradation study. The samples had a thickness of approximately 75 nm and were annealed at 200, 250, 300, 350, and 400 °C.

The thicknesses of the Zn_3N_2 and the oxide layers over time are shown in **Figure 7.4a** and **Figure 7.4b** respectively. The stability of the annealed samples improved

dramatically with annealing temperature, as indicated by the thickness of the Zn_3N_2 layer being maintained for longer periods in annealed samples. The ~75 nm film examined here was fully oxidised within 3 days of exposure to ambient. When annealed at 350-400 °C the films showed little to no signs of oxidation for up to 10 months after deposition. This is a drastic improvement in stability. It is noted that the final thickness of the fully oxidised samples was greater than the initial layer. This shows that the Zn_3N_2 films expand as a result of the oxidation process, something which had previously been observed in SEM of thicker samples, as shown in the inset of **Figure 7.2a**.

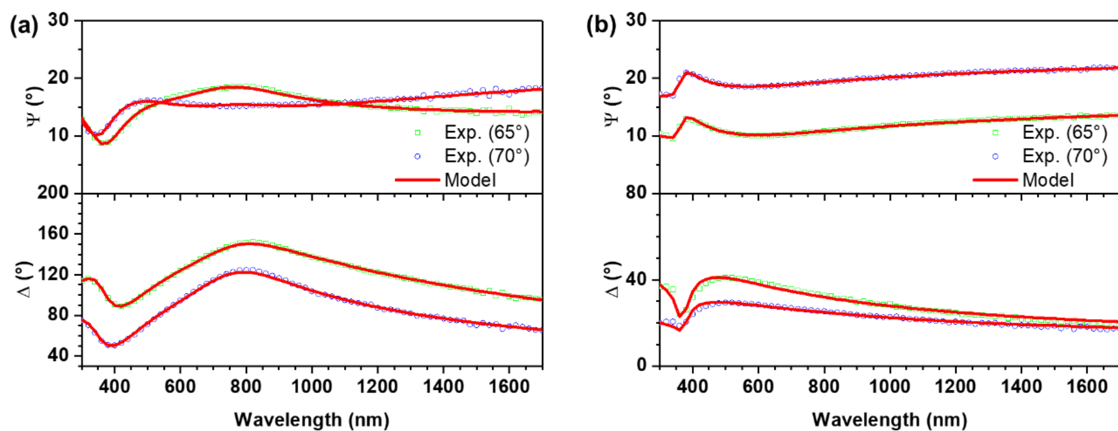

Figure 7.3: Experimental and modelled ellipsometric parameters of an as-deposited 75 nm Zn_3N_2 film (a) shortly after deposition, and (b) after full oxidation.

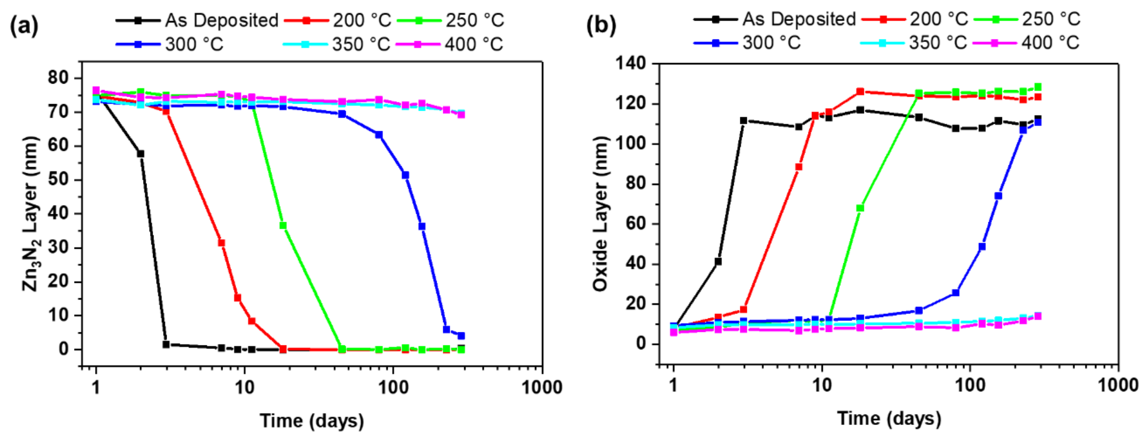

Figure 7.4: Thickness of (a) the Zn_3N_2 layer, and (b) the oxide layer over time for samples annealed under nitrogen atmosphere. The time axis is on a log-scale.

The oxidation rate of the annealed samples was not constant over time, suggesting that the oxidation of these films is a two-step process. This is shown in **Figure 7.5a** for the sample annealed at 300 °C. The oxidation process is described here using two different rates of oxidation: one which determines oxidation at the surface of the films (onset of oxidation) and one which determines the stability of the films after that (bulk oxidation).

The depletion rate of the Zn_3N_2 layer was calculated for the two steps as a function of annealing temperature and is shown in **Figure 7.5b**. As the annealing temperature increases, the reaction rate for both steps decreases exponentially.

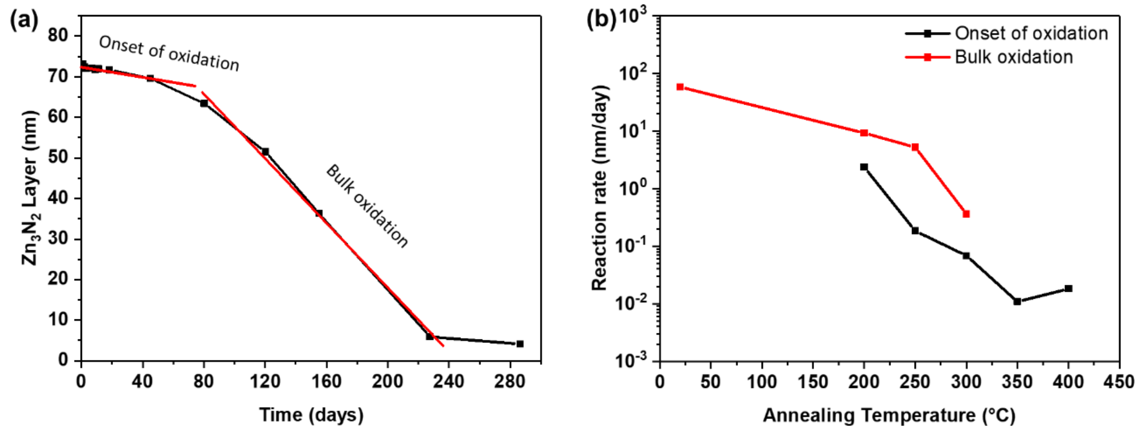

Figure 7.5: (a) Thickness of a Zn_3N_2 layer annealed at 300 °C over time. (b) Reaction rates (in terms of the rate of depletion of the Zn_3N_2 layer) for samples annealed at different temperatures.

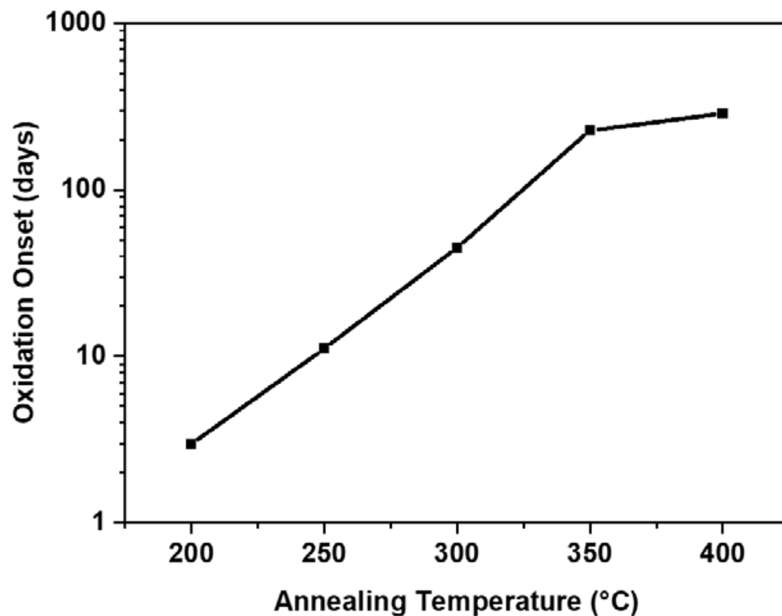

Figure 7.6: Duration of the first step of the oxidation process for different annealing temperatures.

The following mechanism is suggested to explain the results. The first step of the oxidation process must be limited by the rate of diffusion of O_2 and H_2O through the surface oxide layer. Therefore, the improved stability with annealing temperature is likely the result of a reconstruction of the surface oxide layer which makes it less permeable to O_2 and H_2O species. The improved stability of the films that have been annealed at higher temperatures suggests that the quality of the surface oxide increases with annealing temperature. In the second step of the oxidation process, the diffused O_2 and H_2O species react with the Zn_3N_2

surface, resulting in further growth of the oxide layer. The measured oxidation rate during the second step is still low because it is limited by diffusion of the O_2 and H_2O species in the first step. However, because the resulting oxide has a porous nanostructure and expands the thickness of the sample, as shown in the inset of **Figure 7.2a**, it deteriorates the quality of the surface oxide and increases the average reaction rate over time. With that said, the oxidation rates for the samples annealed 300-400 °C are still in the order of 10^{-2}-10^{-1} nm/day, which is a significant improvement compared to as-deposited samples.

The duration of the first step in this mechanism is plotted against the annealing temperature in **Figure 7.6**. This graph shows that for the samples annealed in the range of 350-400 °C, signs of significant oxidation were not observed until 100-200 days. This trend reached a maximum at around 400 °C. It is concluded from this discussion that the simple annealing step performed here improves the quality of the native oxide in Zn_3N_2, which significantly improves ambient stability without the need of further capping layers.

7.3. Crystal structure

Changes in the crystal structure of the annealed Zn_3N_2 films were investigated by X-ray Diffraction (XRD) measurements. The (400) diffraction peak of a set of samples annealed at 200, 300 and 400 °C is shown in **Figure 7.7a**. The graph shows that the (400) peak shifts to wider angles when annealed at high temperatures. The set of samples presented here is based on Zn_3N_2 films sputtered on glass, but the same trend was also observed in MBE-grown samples, regardless of the substrate. A similar effect was observed by Núñez *et al.* when varying the substrate temperature during growth.[1] The shift is more significant for peaks at wider angles which suggests it is related to changes in lattice size rather than experimental errors such as misalignment. This is demonstrated in **Figure 7.7b** which shows the relative shift of the (721) diffraction peak after offsetting the graphs to align the (400) peaks.

The observed shift of the diffraction peaks can be attributed to a change of the lattice parameter for different annealing temperatures. Using Bragg's law of diffraction, the lattice spacing d is calculated from the position of the (400) peak. For a cubic crystal structure, the lattice parameter a is then calculated using equation (3.3). This calculation shows that the lattice parameter decreases from 9.78 to 9.74 Å as the annealing temperature increases. In this case, the changes in the lattice parameter can be attributed to changes in residual stress within the polycrystalline films. Tensile or compressive stress may occur as a result

of the growth process in nanocrystalline thin films.[3] Thermal annealing can change the residual compressive or tensile stress because of a thermal expansion mismatch between the film and the substrate. This results in changes in the lattice parameter and by consequence the positions of peaks in the diffraction pattern.

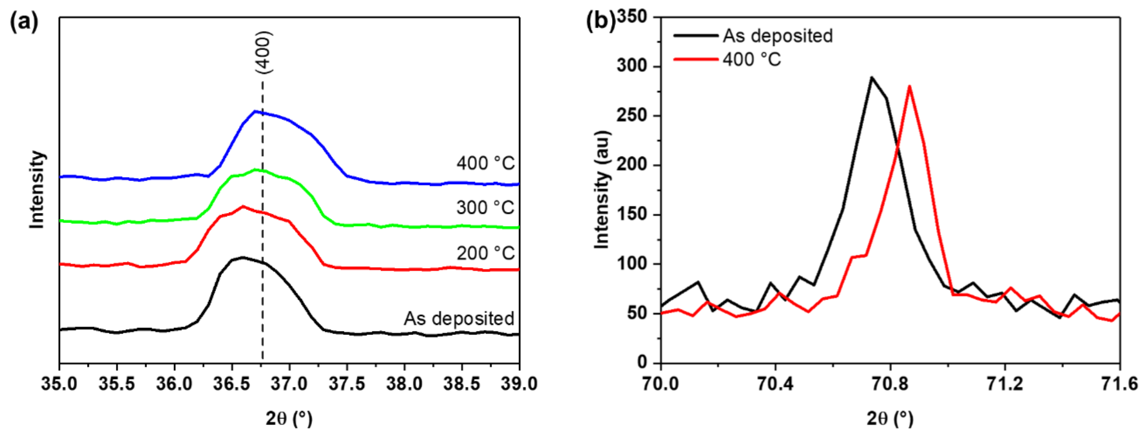

Figure 7.7: (a) Shift of the (400) diffraction peak in grazing incidence after annealing at different temperatures. The dashed line indicates the position of the (400) peak based on crystallographic data for Zn_3N_2.[2] (b) Shift of the (721) diffraction peak in out-of-plane diffraction after offsetting for the shift of the (400) peak.

7.4. Optical bandgap

When annealed at temperatures in the range of 500-800 °C, Zn_3N_2 is known to react with oxygen forming ZnO:N.[4-7] However, previous studies have reported that when annealed at moderate temperatures, e.g. 300 °C, Zn_3N_2 maintains its structure but its optical bandgap shifts to lower values.[8] In the study of Wen *et al.*, the bandgap of Zn_3N_2 shifted by as much as 190 meV (from 1.33 to 1.14 eV) when annealed in oxygen or air at 300 °C. The same effect was observed for the Zn_3N_2 samples studied here. At annealing temperatures of 200-400 °C, Zn_3N_2 samples exhibited a red-shift of the bandgap by up to ~200 meV. This is shown for different annealing temperatures in **Figure 7.8a**, which demonstrates that there is a gradual red-shift of the absorption onset at annealing temperatures of 300-400 °C. A red-shift of the bandgap was observed consistently in all annealed Zn_3N_2 samples examined in this study. The values of the optical bandgap before and after annealing varied in the range of 1.15-1.45 eV.

It is generally known that lattice compression or expansion can cause the bandgap of semiconductors to shift.[9-11] This can occur for both thermally induced strain (i.e. under low or high temperature conditions), and self-equilibrium strain. While it is likely that changes in strain observed in XRD measurements is a contributing factor to the observed shift of

the bandgap, the magnitude of the red-shift (~200 meV) suggests that there are other competing effects. One possible explanation is the Burstein-Moss (BM) shift which was discussed in Chapter 5 for MBE-grown samples. To investigate whether that is the case, the dataset for the BM shift was re-examined with the added data of the red-shift in annealed samples. To ensure that the carrier density measurements correspond to the bandgap measurements, Hall effect measurements of the annealed samples were performed for each annealing temperature. The data is shown in **Figure 7.8b**. This graph shows that thermal annealing significantly affected the measured carrier concentration in the sputtered Zn_3N_2 films. However, the carrier density increased, and the bandgap decreased with increasing annealing temperature. This trend is in the opposite direction of that predicted from the BM shift for a parabolic band approximation, which was observed in the MBE-grown samples. Therefore, the observed bandgap narrowing in annealed samples cannot be attributed to a reduction of the BM effect.

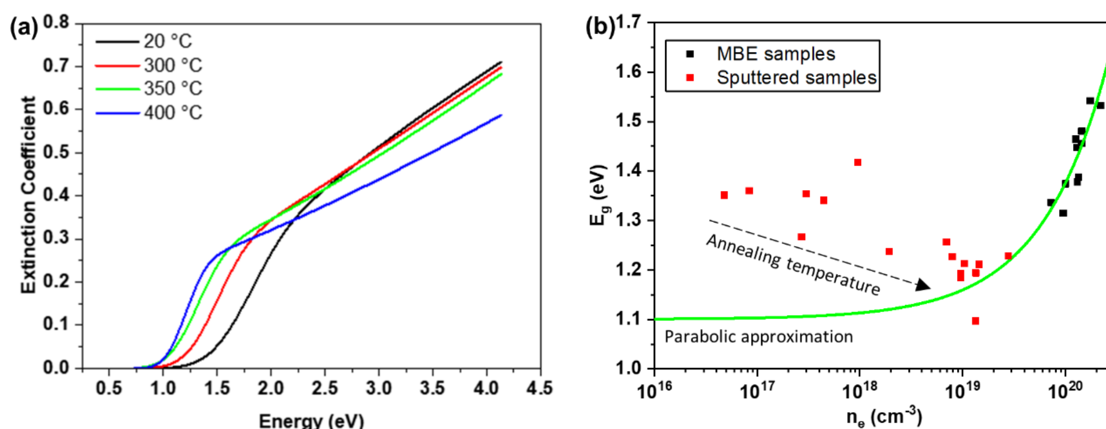

Figure 7.8: (a) Shift of the optical bandgap of polycrystalline Zn_3N_2 films after annealing in a nitrogen atmosphere. The extinction coefficient shown here was obtained from ellipsometric models. (b) Optical bandgap of sputtered and MBE samples against the measured charge carrier density. The arrow shows the direction of increasing annealing temperature from as-deposited samples to samples annealed at 400 °C.

Another possible explanation is that the red-shift in the bandgap is defect-induced, as it is accompanied by an increase in the carrier density. However, **Figure 7.8b** shows a uniform shift of the extinction coefficient to lower energies. In addition, the absorption curve is better defined (steeper) in the annealed samples than in the as-deposited samples. This does not indicate that there is absorption from defect states, which usually takes the shape of absorption tails in the conduction band.[12] Furthermore, at higher carrier concentrations, measured here for the MBE-grown samples, a BM shift is still observed, which shows that the added dopants fill the conduction band. Therefore, it is unlikely that the red-shift of the bandgap is defect-induced. Instead, it is suggested that the wider

bandgaps observed in as-deposited samples are related to deviations from the Zn_3N_2 structure which are at present not fully understood. It could be that the changes in lattice size observed in XRD measurements have a significant effect in the band structure of Zn_3N_2, producing this considerable shift in the bandgap. The range of optical bandgaps shown in **Figure 7.8b** covers a significant portion of the range of narrow bandgaps often reported in literature (see **§2.3**). Therefore, it is argued that the variations observed in literature within this range are caused by similar effects to those discussed here and are related to processing or growth conditions.

7.5. Summary

This chapter discusses the effects of ex-situ thermal annealing on the properties of the Zn_3N_2 films. It was found that the ambient stability of annealed Zn_3N_2 films increased significantly. The stability of the annealed samples improved with annealing temperature up to 400 °C. This was attributed to a reconstruction of the native surface oxide of Zn_3N_2, which decreases its permeability to the oxidising species. The oxidation mechanism is explained here as a two-step process which results in a non-constant rate of oxidation over time. Thermal annealing reduces the average reaction rate of both steps significantly, resulting in an improved stability. The dramatic improvement in film stability illustrated in **Figure 7.4a** demonstrates a significant technological method to utilise the native oxide of Zn_3N_2 to improve stability of the films without growing further capping layers. This solves a major practical challenge in the research and development of this material, and technologies related to it.

Furthermore, it was found that annealing Zn_3N_2 films in nitrogen in temperatures of 200-400 °C affected strain in the crystal structure, resulting in a contraction of the crystal lattice which was evident in the diffraction patterns of the films. This suggests that the growth mechanism in the polycrystalline films studied here generated strain, which was altered by the annealing process. Furthermore, a red-shift of the optical bandgap up to ~200 meV was observed after annealing, which was attributed to an improvement of material quality. The range of bandgaps which was obtained here (1.15-1.45 eV) covers a significant portion of the experimental narrow bandgap reports in literature, suggesting similar effects are responsible for variations of the bandgap of polycrystalline Zn_3N_2 samples in literature.

7.6. Bibliography

[1] C. G. Núñez, J. L. Pau, M. J. Hernández, M. Cervera, E. Ruiz, and J. Piqueras, Thin Solid Films **520,** 1924 (2012).
[2] D. E. Partin, D. J. Williams, and M. O'Keeffe, Journal of Solid State Chemistry **132,** 56 (1997).
[3] E. Chason and P. R. Guduru, Journal of Applied Physics **119,** 191101 (2016).
[4] C. Wang, Z. Ji, K. Liu, Y. Xiang, and Z. Ye, Journal of Crystal Growth **259,** 279 (2003).
[5] D. Wang, Y. C. Liu, R. Mu, J. Y. Zhang, Y. M. Lu, D. Z. Shen, and X. W. Fan, Journal of Physics: Condensed Matter **16,** 4635 (2004).
[6] E. Kaminska, A. Piotrowska, J. Kossut, A. Barcz, R. Butkute, W. Dobrowolski, E. Dynowska, R. Jakiela, E. Przezdziecka, R. Lukasiewicz, M. Aleszkiewicz, P. Wojnar, and E. Kowalczyk, Solid State Communications **135,** 11 (2005).
[7] B. S. Li, Y. C. Liu, Z. Z. Zhi, D. Z. Shen, Y. M. Lu, J. Y. Zhang, X. W. Fan, R. X. Mu, and D. O. Henderson, Journal of Materials Research **18,** 8 (2003).
[8] T. Wen, M. Gautam, A. M. Soleimanpour, and A. H. Jayatissa, Materials Science in Semiconductor Processing **16,** 318 (2013).
[9] Z. Zhu, A. Zhang, G. Ouyang, and G. Yang, The Journal of Physical Chemistry C **115,** 6462 (2011).
[10] F. Caili, D. Junhong, and L. Gang, Materials Research Express **2,** 045008 (2015).
[11] M. Devika, N. K. Reddy, F. Patolsky, K. Ramesh, and K. R. Gunasekhar, Applied Physics Letters **95,** 261907 (2009).
[12] J. J. Thevaril and S. K. O'Leary, Solid State Communications **150,** 1851 (2010).

Chapter 8: Zinc Nitride Nanoparticles by Gas Phase Aggregation

8.1. Zinc Nitride nanoparticles

Part of the motivation to study Zn_3N_2 in the form of nanoparticles stems from the motivation to demonstrate bandgap tunability, which is useful for photonics applications. Previous studies which have demonstrated Zn_3N_2 nanoparticles with a tuneable photoluminescence emission at different nanoparticle sizes.[1] In this case, the effects of quantum confinement can be utilised to tune the bandgap. When deposited in an MBE vacuum chamber, the Zn_3N_2 nanoparticles can potentially be encapsulated in heterostructures to further investigate their properties and develop possible applications. Furthermore, Zn_3N_2 nanoparticles have been reported to enhance electrocatalytic processes in dye-sensitised solar cells, as discussed in §2.6.[2]

The formation and deposition of Zn_3N_2 nanoparticles using the gas-phase aggregation process described in Chapter 3 is discussed here. Initially, the formation and deposition of Zn nanoparticles with a NanoGen50 nanoparticle source was investigated. Once that was established, an RF nitrogen plasma source was used as the source for active nitrogen species to form Zn_3N_2 nanoparticles.

8.2. In-situ process monitoring

The nanoparticle aggregation process was monitored in-situ with a quadrupole mass spectrometer (QMS). By changing the frequency of the alternating electric field applied to the quadrupole, a range of nanoparticles could be filtered based on their mass-to-charge ratio. To measure the size distribution of the nanoparticle beam, a range of frequencies was scanned and the current generated by the nanoparticle beam was measured at each frequency. A typical size distribution of the generated nanoparticle beam is shown in **Figure 8.1**. The optimum operating conditions were identified by varying the following experimental parameters:

- the insertion length of the magnetron gun into the aggregation zone,
- the argon flow rate, and
- the sputter current applied to the Zn target,

and measuring the mean nanoparticle size and the flux of the nanoparticle beam.

Initially, the insertion length was varied at a fixed argon flow rate of 90 sccm (standard cubic centimetres per minute) and a sputter current of 150 mA. Increasing the insertion length of the magnetron into the aggregation zone reduces the length of the aggregation zone and therefore the residence time of the nanoparticles in the aggregation zone. Thus, both the size of the nanoparticles and the flux of the nanoparticle beam decreased as the insertion length increased, as shown in **Figure 8.2a**. To maximise the flux of the nanoparticle beam, the insertion length was set to the minimum, maximising the length of the aggregation zone.

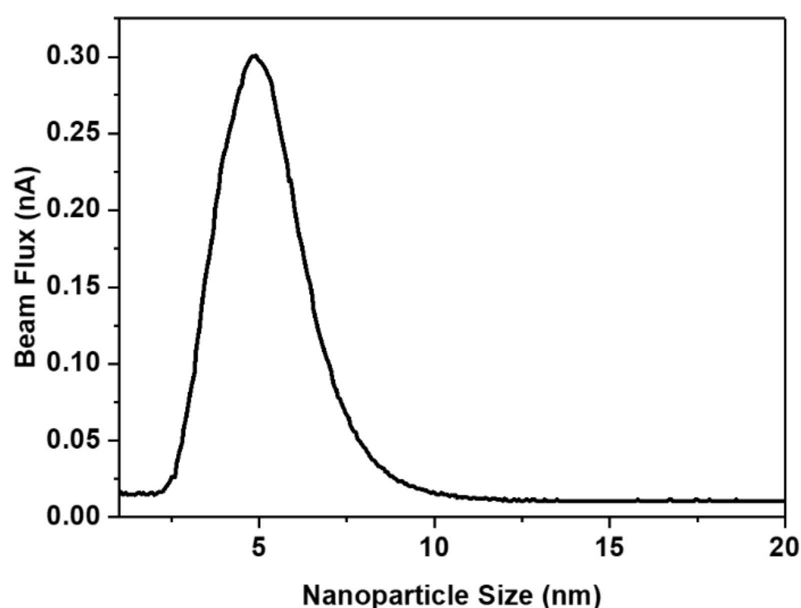

Figure 8.1: Typical distribution of the generated nanoparticle beam, measured with a quadrupole mass spectrometer.

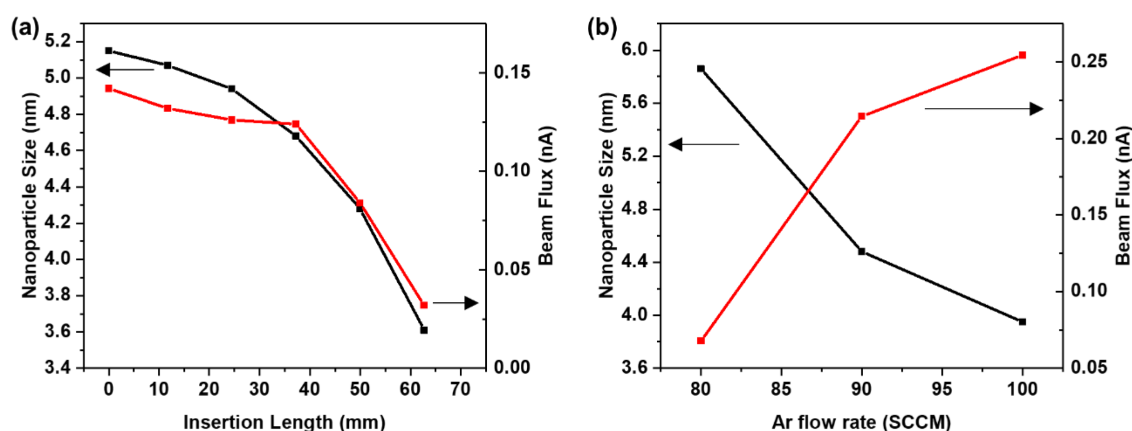

Figure 8.2: Mean nanoparticle size (black) and flux of the nanoparticle beam (red) as a function of (a) the insertion length of the magnetron gun, and (b) the argon flow rate.

Next, the argon flow rate was varied from 80 to 100 sccm. As shown in **Figure 8.2b**, lower gas flow rates resulted in larger nanoparticle sizes, because of the increased residence time of the nanoparticles. However, the flux of the nanoparticle beam decreased dramatically at low Ar flow rates, to the point that no nanoparticle distribution was measured at flow rates below 80 sccm. This is likely related to the role of argon molecules in the thermalisation of the sputtered Zn vapour. Reducing the gas flow rate also reduced the flux of the nanoparticle beam, because the sputtered atoms remain at a high temperature which is detrimental for the cluster nucleation process.[3] Finally, the sputter current was increased up to 225 mA. Both the nanoparticle size and the beam flux increased with increasing current, as shown in **Figure 8.3**. This is attributed to an increase in the density of the sputtered vapour leading to the formation of a greater number of cluster seeds, which in turn lead to the formation of bigger nanoclusters.

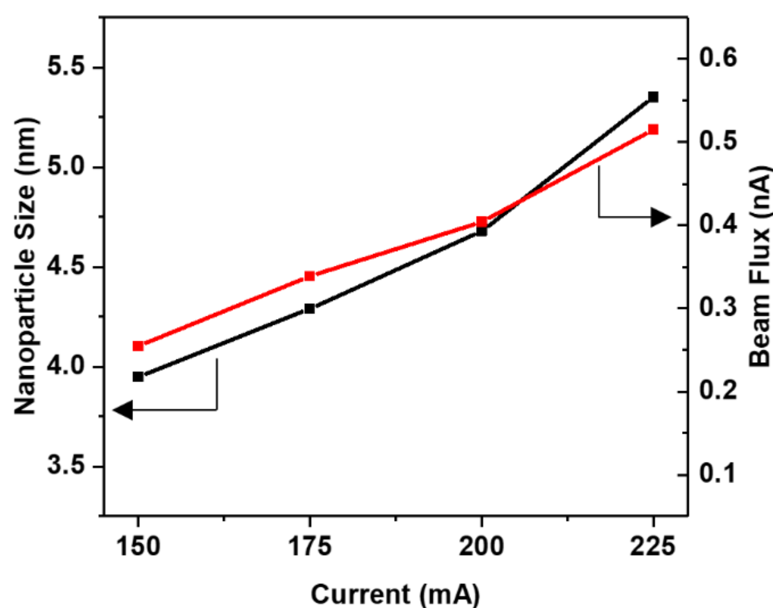

Figure 8.3: Mean nanoparticle size (black) and flux of the nanoparticle beam (red) as a function of sputter current.

8.3. Deposition rate and process stability

Operating the magnetron gun at high currents for extended periods resulted in a rapid decrease of the beam flux, an increase in the mean nanoparticle size and sputter voltage, and eventually arcing. The deposition rate measured by a Quartz Crystal Monitor (QCM) also decreased with time, suggesting it is not an artefact related to the QMS. The sputter process recovered if given enough time to cooldown. The measured beam flux of

the nanoparticle source over a 1-hour experiment at a fixed current is shown in **Figure 8.4**. It is speculated that this behaviour was caused by overheating of the target or charge build-up.

Under the conditions examined here, the QCM indicated that the deposition rate of the Zn nanoparticles was in the order of 6 nm/h, 5 μg·cm^{-2}·h^{-1} or 4×10^{16} atoms·cm^{-2}·h^{-1}. Because of the low measured deposition rates, maintaining the beam flux for extended periods was crucial. Therefore, to enable longer experiments without the flux of the nanoparticle beam deteriorating significantly, a current of 175 mA was used.

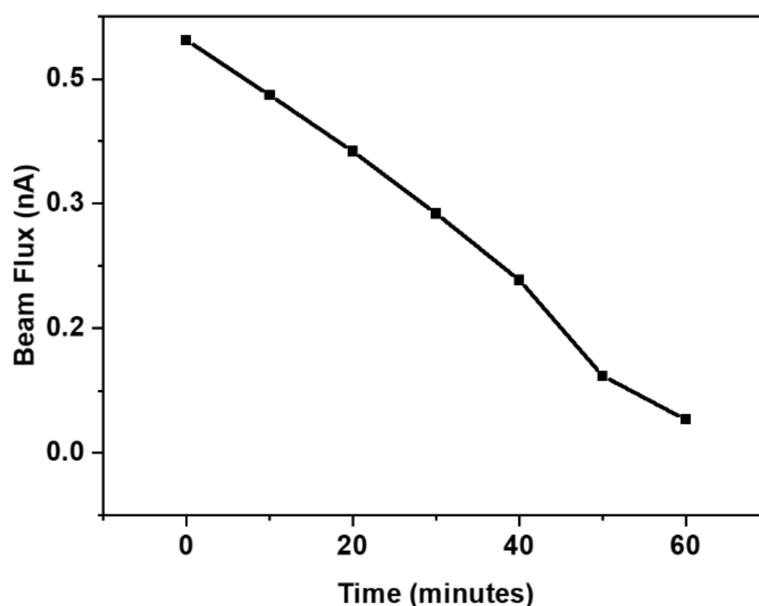

Figure 8.4: Measured nanoparticle beam flux over a 1 h experiment at 225 mA.

8.4. Nanoparticle deposition with and without nitrogen plasma

Zn nanoparticles were deposited on Si (100) and glass substrates. Scanning Electron Microscopy (SEM) images showed that the deposition rate for the Zn nanoparticles was very low, as indicated by the QCM estimate of 6 nm/h. The surface of one of these samples is shown in **Figure 8.5a**. The SEM images featured particles in the range of 10-20 nm and revealed that the substrate was only partially covered by the nanoparticles in a 3 hour experiment. This experiment was repeated with the nitrogen plasma source operated at a power of 450 W to form Zn_3N_2. It was found that a significantly greater number of nanoparticles was deposited on the substrate with the nitrogen plasma running. This resulted in the formation of a nanoporous film, the morphology of which is shown in **Figure 8.5b**. The mean nanoparticle size measured in-situ by the QMS was 4-6 nm for these

experiments. The larger nanoparticle sizes observed in the SEM images are likely the result of nanoparticle aggregation, and oxidation. As nanoparticles arrive on the surface of the substrate, they interact with other nanoparticles and aggregate into larger clusters. Furthermore, it is expected that the nanoparticles may form a core-shell structure with ZnO, or even be fully oxidised in contact with air.[4] The formation of a ZnO shell increases the size of the nanoparticles, resulting in the larger features observed in the SEM images.

With enough nanoparticles, a film with the nanostructure shown in **Figure 8.5b** is formed. The significant increase in the amount of material deposited in the presence of nitrogen plasma indicates that the sticking coefficient of the Zn nanoparticles on Si is low, and that it was enabled by the introduction of active nitrogen on the deposition surface. This is analogous to what was observed for evaporated Zn in Chapter 5, in which the deposition of Zn on glass was only observed under nitrogen plasma and resulted in the formation of a Zn_3N_2 film. As a result, it is concluded that a significant amount of the Zn nanoparticle flux did not stick on the substrate for the samples deposited without nitrogen plasma. It is highly likely that Zn_3N_2 nanoparticles were formed when nanoparticles were deposited under nitrogen plasma. This was investigated with Energy Dispersive X-ray Spectroscopy (EDS) and ellipsometry measurements.

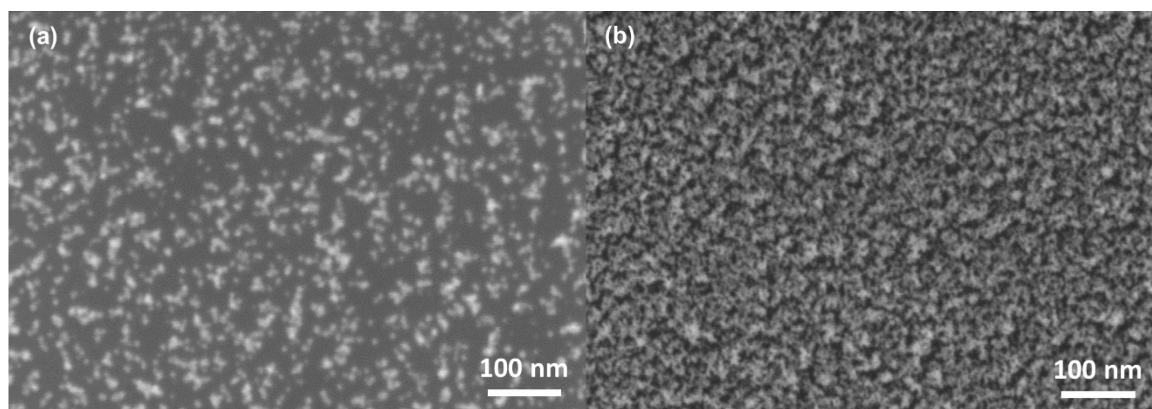

Figure 8.5: SEM images of Zn nanoparticles and deposited on Si in 3 h experiments (a) without and (b) with nitrogen plasma running during deposition.

EDS measurements of two samples deposited with and without nitrogen plasma during deposition are shown **Figure 8.6a**. Characteristic X-rays originating from C, O, Zn and Si were observed for both samples. A direct comparison of the EDS spectra for the two samples shows that the Zn and O peaks were significantly stronger in the sample deposited under nitrogen plasma. In contrast, the peak originating from the Si substrate is significantly reduced, indicating that the substrate accounts for a lower fraction of the analysis volume under the same excitation conditions. Therefore, it is concluded that the nanostructures

observed in **Figure 8.5** consist of Zn and O in great quantities. As a result, the EDS measurements indicate that the nanoparticles are well oxidised, because both Zn and O were observed in significant amounts in both samples.

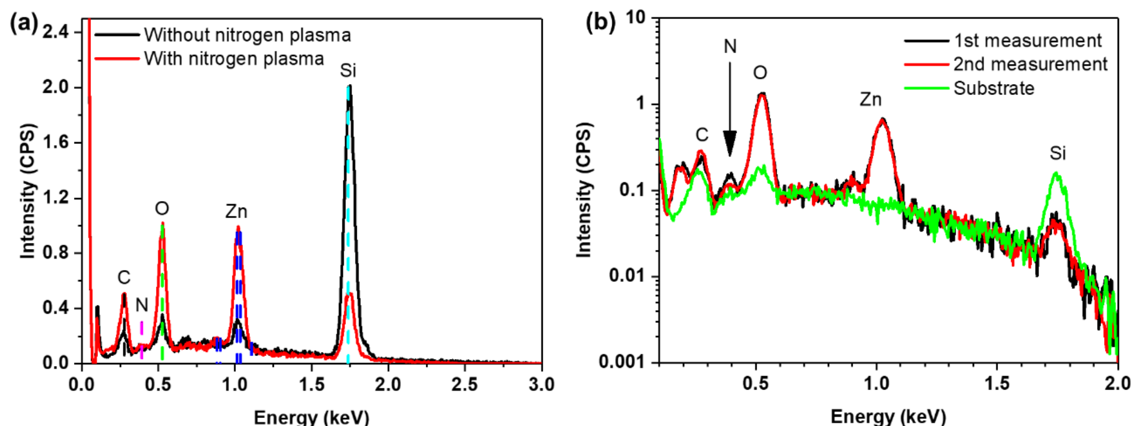

Figure 8.6: EDS measurements of (a) two samples deposited with and without nitrogen plasma during deposition, and (b) a nanoparticle sample measured shortly after exposure to air and 24 h later. A scan of the Si substrate under the same conditions is shown for reference.

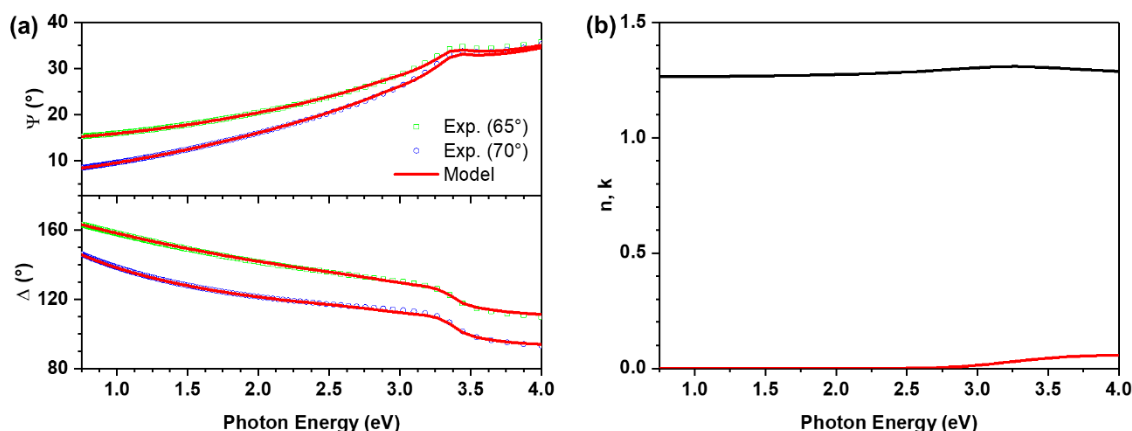

Figure 8.7: (a) Experimental and modelled ellipsometric parameters for a nanoparticle film deposited under nitrogen plasma. (b) Refractive index *n* (black) and extinction coefficient *k* (red) obtained for the nanoparticle film from the ellipsometric model.

No evidence of the incorporation of nitrogen into the nanoparticle film was observed initially. However, because Zn_3N_2 films tend to oxidise the nanoparticle film may have oxidised rapidly in contact with air.[5,6] To find evidence for the formation of Zn_3N_2 in the nanoparticle film, the sample grown under nitrogen plasma was repeated and was immediately (within minutes of exposure to air) transferred to the SEM instrument. The EDS spectrum of this sample is shown in **Figure 8.6b**. A similar EDS spectrum was observed, showing that the film included a large amount of oxygen. However, traces of nitrogen were also observed, indicated by the arrow in **Figure 8.6b**. The EDS measurement was repeated after 24 hours, which showed that the intensity of the nitrogen feature had

decreased further. These results suggest that nitrogen was initially incorporated into the deposited films, but the Zn_3N_2 nanoparticles oxidised rapidly when exposed to air. It is concluded that Zn_3N_2 nanoparticles can be generated with this process, however, they must be encapsulated to be studied further. To allow Zn_3N_2 nanoparticles to be studied optically, the encapsulation material must have a much wider bandgap than Zn_3N_2 so that it does not interact with photons at the energy region of interest. Potential candidates that would achieve this include GaN, AlN, Si_3N_4, or SiO_2. However, growing these materials in the same MBE system required modifications that were currently not available.

Finally, the thickness and optical properties of the nanoparticle film were investigated by ellipsometry. The experimental and modelled ellipsometric parameters are shown in **Figure 8.7a**. The optical properties obtained for the nanoparticle film are shown in **Figure 8.7b**. A two-layer model consisting of a semiconductor layer and the Si substrate was used. The ellipsometric model suggests that the thickness of the nanoparticle film was approximately 55 nm and had a roughness in the order of 20 nm.

The modelled nanoparticle film had a refractive index of 1.3, and an absorption onset of approximately 3.0 eV. The transparency in the visible region further suggests that the deposited film consisted of a ZnO structure. The refractive index is low compared to that of ZnO which is 1.9 in the near infrared. However, this is likely a result of porosity which was not factored in the model. The thickness of this nanoparticle film (55 nm) is relatively close to the nanoparticle flux measured with the QCM which was ~6 nm/h. In a 3 h experiment and assuming a dense Zn film, this flux should result in a film of ~18 nm. Because the nanoparticle film is not densely packed and is significantly oxidised, its thickness should be greater than 18 nm. Comparing these numbers makes it clear that the partial coverage obtained for the samples deposited without nitrogen plasma corresponds to a small fraction of the full flux of the Zn nanoparticle beam and highlights the low sticking coefficient of Zn nanoparticles on these substrates.

8.5. Summary

This chapter investigated a process to deposit Zn_3N_2 nanoparticles by gas phase aggregation. Initially, in-situ monitoring techniques were used to optimise the Zn nanoparticle beam. It was found that the Zn nanoparticle flux was relatively low with the available experimental setup. Furthermore, only a small portion of the produced Zn nanoparticles was deposited on unprocessed Si and glass substrates, indicating a low

sticking coefficient of Zn. The yield of the deposition process increased under nitrogen plasma, which provided active species for Zn to react with. This resulted in the formation of a nanoparticle film with a fine nanostructure. Deposition under nitrogen plasma likely resulted in the formation of Zn_3N_2, as seen for evaporated Zn in Chapter 5. However, only traces of nitrogen were observed in EDS measurements, indicating that the Zn_3N_2 nanoparticles were rapidly oxidised because of their large surface area. Therefore, it is suggested that Zn_3N_2 nanoparticles, or similar nanostructures of Zn_3N_2 must be encapsulated to be studied further. The encapsulation material must be selected so that it has a wider bandgap than the energy region of interest for Zn_3N_2 nanoparticles (e.g. GaN, AlN, Si_3N_4, SiO_2).

8.6. Bibliography

1 P. N. Taylor, M. A. Schreuder, T. M. Smeeton, A. J. D. Grundy, J. A. R. Dimmock, S. E. Hooper, J. Heffernan, and M. Kauer, Journal of Materials Chemistry C **2,** 4379 (2014).

2 L. Chun-Ting, C. Hung-Yu, L. Yu-Yan, H. Yi-June, T. Yu-Lin, R. Vittal, S. Yu-Jane, and H. Kuo-Chuan, ACS Applied Materials & Interfaces **7,** 28254 (2015).

3 P. Grammatikopoulos, S. Steinhauer, J. Vernieres, V. Singh, and M. Sowwan, Advances in Physics: X **1,** 81 (2016).

4 P. Camarda, F. Messina, L. Vaccaro, G. Buscarino, S. Agnello, F. M. Gelardi, and M. Cannas, Journal of Applied Physics **120,** 124312 (2016).

5 C. G. Núñez, J. L. Pau, M. J. Hernández, M. Cervera, E. Ruíz, and J. Piqueras, Thin Solid Films **522,** 208 (2012).

6 M. Gómez-Castaño, A. Redondo-Cubero, L. Vázquez, and J. L. Pau, ACS Applied Materials & Interfaces **8,** 29163 (2016).

Chapter 9: Conclusions and Further Work

9.1. Conclusions

This work has investigated the properties of Zn_3N_2, a relatively little-studied semiconductor material, and discussed its potential for semiconductor applications. Previous studies have indicated that Zn_3N_2 is a candidate for use as a low-cost solar absorber.[1] However, some aspects of Zn_3N_2, e.g. its band structure, remain controversial to date.[2,3]

In this work, Zn_3N_2 samples were deposited by Reactive Sputtering and Molecular Beam Epitaxy (MBE). The deposition of Zn_3N_2 nanoparticles by a gas-phase aggregation process was also examined. Investigation of the growth processes for both MBE and sputtering showed that the growth rate of Zn_3N_2 decreases rapidly with increasing temperature. Higher growth rates were more easily achieved by sputtering, although the same trend was observed. This was attributed to a tendency of Zn to desorb at relatively low growth temperatures. As a result, a surplus of Zn is necessary to maintain high growth rates at high substrate temperatures. Furthermore, attempts to deposit evaporated Zn, or Zn in the form of nanoparticles highlighted that Zn has a low sticking coefficient on the substrates investigated here (Si, glass), even for unheated deposition. The effect of the growth surface on the high temperature growth rate was investigated by (a) the growth of a buffer layer at a low temperature, and (b) a thermal treatment of the substrates to high temperatures prior to growth. Both approaches had a positive effect on the growth rate by providing a more favourable surface with which Zn could react.

The deposited Zn_3N_2 films were polycrystalline in structure. The strongest diffraction peak was predominantly the (400) peak, indicating that (100) is a favoured crystal orientation for Zn_3N_2. Depositing Zn_3N_2 at high substrate temperatures improved the crystal orientation, but in some cases decreased the crystal quality because of poor lattice matching with the substrate. When grown on approximately lattice matched substrates, both crystallinity and the degree of orientation of the films improved. Single crystal samples were not obtained in this study, which highlights the need for further optimisation of the growth conditions such as the Zn:N ratio during growth.

In terms of electrical properties, all Zn_3N_2 samples studied here were highly doped n-type semiconductors. The carrier concentration varied from 10^{18} to 10^{21} cm^{-3} in different samples. Degenerate-level unintentional doping is a common occurrence in Zn_3N_2 samples. Under such high doping, carrier mobilities in the range of 30-130 cm^2 V^{-1} s^{-1}were obtained at high substrate temperatures. The high doping levels in Zn_3N_2 are attributed to intrinsic defects and unintentional oxygen doping. The most thermodynamically favoured n-type defects are thought to be nitrogen vacancies. In this study, the doping level could not be significantly reduced despite attempts to improve the purity of the growth environment and crystal structure. As a result, the growth parameters and conditions require further development and may involve narrow optimum conditions. Furthermore, the development of novel techniques, such as optimisation of buffer layers or surface preparation, may be necessary.

The measured optical bandgap of Zn_3N_2 samples varied in the range of 1.15-1.60 eV. Furthermore, the refractive index of Zn_3N_2 was calculated at 2.4-2.7 from optical measurements. Analysis of the absorption coefficient indicates that the bandgap of Zn_3N_2 is direct, based on the strong absorption observed in Zn_3N_2 films. An argument is developed that the Tauc plot which is commonly used to interpret absorption spectra can easily lead to an overestimation of the bandgap if the parameters for the analysis are not carefully selected. This has likely contributed to the discrepancies in previous experimental reports, which have reported values in the range of 1.0 eV to 3.4 eV. The Zn_3N_2 samples examined in this study have consistently displayed a narrow bandgap. Variations in the measured optical bandgap were attributed to the Burstein-Moss (BM) effect for samples doped in the order of 10^{20} cm^{-3}. From the analysis in this work, it is proposed that the intrinsic bandgap of Zn_3N_2 is in the energy region of 1.10-1.40 eV. Evidence for a narrow bandgap in Zn_3N_2 was further observed in photoluminescence measurements of certain samples which exhibited bright photoluminescence features in the region of 1.40 eV.

The tunability of the optical properties of Zn_3N_2 was demonstrated in a ternary AlZnN alloy. By increasing the Al content in the alloy films, the bandgap increased up to 2.76 eV. These results are the first attempts to develop a compatible materials system for use in Zn_3N_2-based heterostructures. The observed tuning of the optical properties is a promising first step for the AlZnN system, although the crystal structure of the alloy films requires optimisation. Furthermore, the electrical properties in the AlZnN alloys changed significantly, reaching carrier concentrations as low as 10^{16} cm^{-3}. These changes were

attributed to an increased donor binding energy at high Al content, which resulted to fewer carriers excited to the conduction band. It is suggested that further investigation of these alloys could provide insight on the high doping levels observed experimentally in Zn_3N_2 samples. In addition, although the AlZnN films remained n-type, they may be a more suitable starting point for future doping studies than degenerately doped Zn_3N_2.

Finally, a method to improve the ambient stability of as-deposited Zn_3N_2 films was demonstrated by means of an ex-situ thermal annealing process. Zn_3N_2 thin films annealed at temperatures of 200-400 °C demonstrated increasingly improved stability against oxidation under ambient conditions. The improved stability is believed to be caused by an improvement in the quality of the surface oxide layer, which prevents further exposure of the Zn_3N_2 surface to O_2 and H_2O species. The method discussed here displayed a significant improvement in the stability of the Zn_3N_2 films (from 3 days to more than 200 days to full oxidation), which is crucial for further use of these layers, e.g. for processing or use in devices. It is interesting that this method utilises the native oxide which grows on the Zn_3N_2 surface and does not require growth of an additional capping layer. Other effects of thermal annealing on these layers must be taken in consideration, such as those reported here (strain, bandgap narrowing, changes in the carrier concentration). However, these effects will likely be less significant as this material is better understood and grown in better quality.

9.2. Further work

The experiments discussed in this work have opened several paths for further research. More specifically:

1. Optimisation of MBE and sputtering processes to improve crystal quality.
2. Further investigation of the potential of new ternary alloys, e.g. AlZnN or GaZnN.
3. Identification of p-type dopants through doping studies.
4. Design and fabrication of prototype devices such as solar cells, detectors, LEDs or thin film transistors.

The scope and requirements for each topic are discussed in the following paragraphs.

9.2.1. Optimisation of the crystal structure

Improving the crystal quality of Zn_3N_2 samples is an important aspect of the pursuit to improve material quality, material purity, and to further the understanding of the

fundamental properties of Zn_3N_2. This is because of the degenerate-level unintentional doping observed in polycrystalline Zn_3N_2 samples, which is thought to be caused by structural defects and impurities. Minimising the defect density is also crucial for charge transport properties and device performance. This can be a continuation of the MBE experiments discussed in this work. Further optimisation of the MBE growth process (e.g. II-V ratio, substrate temperature, substrate preparation) is required to achieve single-crystal growth and minimise structural defects. Out of these parameters, it is likely that preparation of the growth surface (either in the form of substrate type and treatment, or in the form of buffer layer growth and optimisation) will play a crucial role in obtaining single-crystal growth. The experiments in this study suggest a higher Zn flux is required to account for the desorption of Zn at high substrate temperatures. Some modifications to the MBE system may also be necessary to allow for better control of some of these parameters (e.g. mass flow controller for low flow rates). Further characterisation of highly crystalline samples (e.g. XPS or SIMS, RBS, and DLTS) will be beneficial towards investigating impurity and defect levels in the grown samples.

Developing a reactive sputtering process for the growth of single-crystal Zn_3N_2 may be interesting for the purposes of comparison in further experiments. In addition, achieving good material quality in samples grown by sputtering will also further demonstrate the commercialisation potential of this material. The single-crystal growth of Zn_3N_2 by reactive sputtering has already been demonstrated by Cao *et al.* on YSZ substrates, so the substrates investigated here (YSZ and Al_2O_3) will likely suffice.[4] To achieve a single-crystal sputtering process based on the experiments discussed here, the use of a mixture of Argon and N_2 as a sputter gas will be necessary. Furthermore, using an RF power supply may also be beneficial as it will minimise charge build-up on the sputter target.

9.2.2. Investigation of ternary alloys and their structure

The possibility of II-III-V semiconductor alloys was demonstrated in this study by the deposition of AlZnN samples. The AlZnN samples exhibited tuneable optical properties and significantly lower charge carrier density levels. However, the crystal structure of these alloys requires further investigation, as the AlZnN samples examined here became amorphous at high Al content. It may be possible to obtain crystalline AlZnN samples through optimisation of growth conditions and the growth surface (substrate type and preparation). The investigation of other ternary alloys, such as GaZnN, is also interesting

for bandgap tuning. The possibility of a MgZnN alloy may also be worth investigating, as Mg_3N_2 and Zn_3N_2 share the same crystal structure and could be more compatible than II-III-V alloys.

9.2.3. Identifying p-type dopants

Achieving p-type doping in Zn_3N_2-based materials is crucial as it will enable the fabrication of semiconductor devices which require a p-n junction. Typically, p-type conductivity type may be achieved by intrinsic dopants or impurities incorporated during growth. However, the overwhelming number of reports of n-type samples in literature suggests that variations in the stoichiometry of Zn_3N_2 are unlikely to result in p-type doping. Furthermore, there is little guidance from computational studies as to which elements may be p-type dopants to the crystal structure of Zn_3N_2. One study which investigated Cu-Group elements suggested that out of Cu, Ag, and Au, only Cu is a p-type dopant for Zn_3N_2.[5] Dopants used in other semiconductors, such as Mg, Be, B, may also be a good start for the investigation. However, performing a doping study on degenerately doped samples is a significant challenge. As a result, the objective of minimising defects and unintentional doping is related to identifying p-type dopants. The AlZnN materials discussed in this study may be a good starting point for such an investigation, as they exhibited relatively low charge carrier concentrations.

9.2.4. Prototype device fabrication

A final and significant point for further research is to demonstrate the applicability of Zn_3N_2 in semiconductor devices by designing and fabricating prototype devices. The use of Zn_3N_2 in thin film solar cells seems like a reasonable starting point, based on the narrow bandgap and strong absorption coefficient of Zn_3N_2 films. Ideally, this would be done with high-quality material and with a materials system native to Zn_3N_2 (i.e. p-type and n-type Zn_3N_2). Furthermore, Zn_3N_2-based alloys can be employed in multijunction solar cell structures, to optimise absorption of the solar spectrum. Obtaining initial results from this materials system can help guide development and further research. Therefore, initial attempts may have to make use of other materials, such as a p-type GaAs substrate, if p-type conductivity cannot be obtained otherwise. Once such novel technologies are developed and demonstrated to have promising device performance, the use of Zn_3N_2 in low-cost semiconductor devices may become commercially viable.

9.3. Bibliography

[1] M. Ullah, G. Murtaza, M. Yaseen, and S. A. Khan, Journal of Alloys and Compounds (2017).
[2] X. Cao, Y. Ninomiya, and N. Yamada, physica status solidi (a) **214,** 1600472 (2017).
[3] J. Jia, H. Kamijo, S. Nakamura, and Y. Shigesato, MRS Communications**,** 1 (2018).
[4] X. Cao, Y. Yamaguchi, Y. Ninomiya, and N. Yamada, Journal of Applied Physics **119,** 025104 (2016).
[5] N. Jiang, J. L. Roehl, S. V. Khare, D. G. Georgiev, and A. H. Jayatissa, Thin Solid Films **564,** 331 (2014).